Low Temperature Plasma Enhanced Atomic Layer Deposition of Conducting Zirconium Nitride: In-situ growth characterization, recipe development, and the sources of oxygen contamination in films

by

Triratna Parmeshwar Muneshwar

A thesis submitted in partial fulfillment of the requirements for the degree of

Doctor of Philosophy

in
Materials Engineering

Department of Chemical and Materials Engineering
University of Alberta

© Triratna Parmeshwar Muneshwar, 2014

Abstract

Atomic layer deposition (ALD) enables uniform and conformal deposition of sub-nanometer thick films over large substrate area, hence is the most suitable technique for deposition of critical features in modern semiconductor fabrication. Compared to other transition metal nitrides, reported studies on zirconium nitride (ZrN) ALD are scarce. Moreover ALD of conducting ZrN is relevant for numerous applications in advanced semiconductor devices. Plasma enhanced ALD (PEALD) ZrN thin films using tetrakis-dimethylamido zirconium (TDMAZr) and forming gas (5% H_2, 95% N_2) reactant plasma were grown on p-type Si (111) and thermal SiO_2 substrates at temperatures in the range of 100 °C - 350 °C. The ZrN PEALD growth was characterized from dynamic in-situ spectroscopic ellipsometry (*d-iSE*) measurements performed in real-time during film growth. A procedure was developed to interpret and analyze *d-iSE* data accounting for partial surface monolayer growth per ALD cycle. The optimum process parameters for self-limiting ZrN PEALD growth were determined from experiments designed on the basis of self-limiting ALD surface reactions. The ZrN film thickness determined from *iSE* data was found to be in agreement with the ex-situ XRR measurement. The metallic nature of ZrN films deposited with 0.10s TDMAZr – 12s purge – 9s plasma – 9s purge at 150 °C and 600 Watts plasma was concluded from the free electron dispersion component of the dielectric function and photoemission features at the Fermi level in the valence band XPS spectra. The glancing incidence x-ray diffraction (GIXRD) pattern was consistent with ZrN and Zr_3N_4 phases along with ZrO_2 feature arising from the post-deposition surface oxidation. The

electrical resistivity for 35.5 nm ZrN film was found to be 559.5 μΩ-cm. The XPS survey spectra showed presence of O and C within the grown ZrN film. The relatively high concentrations of O was explained on the basis of high energy Ar^+ sputtering induced diffusion of oxygen atoms from the surface oxide layer into the underlying film. To address poor ALD precursor consumption, a first-principle numerical model for ALD growth was developed to compare novel ALD recipes with the conventional ABAB… type deposition. ZrN PEALD with AABAAB... cycle showed ~20% increase in the GPC along with 50% reduction in the TDMAZr dose for saturation as compared to ABAB… cycle under similar process conditions.

DEDICATION

This thesis is dedicated to my parents, teachers and friends for their patience, support and encouragement that has been my strength throughout…

Acknowledgements

First and foremost I would like to thank my supervisor, Dr. Ken Cadien, for his time, guidance and support during the course of my Ph.D. Working under his supervision has been a wonderful experience and an excellent opportunity to learn from his experience, technical insight and attitude towards research.

I thank Dr. Douglas Barlage from the Department of Electrical and Computer Engineering, for his suggestions and guidance on the integration of ZrN PEALD films with the III-V semiconductor devices.

I thank Shiraz Merali from the Department of Chemical and Materials Engineering and Dimitre Karpuzov from Alberta Center for Surface Engineering and Science (ACSES) for their assistance with material characterization.

I would like to acknowledge Bruce Rayner from Kurt. J. Lesker, Greg Pribil from J. A. Woollam and Keith Franklin from Nanofab at University of Alberta for their technical support with troubleshooting instrument issues.

I would like to extend my gratitude to my colleagues, especially Amir Afshar, Mengmeng Miao, Brent Rudyk and Pouyan Motamedi, with whom I have had the pleasure to work along.

Thank you all.

Triratna P. Muneshwar
September 2014

Table of Contents

1. **Introduction** 1
1.1. Problem Statement 1
1.2. Research Goals 2
1.3. Thesis Outline 2
1.4. References 4
2. **Literature Review** 6
2.1. ALD Background 6
2.2. Atomic Layer Deposition (ALD) 7
2.2.1. An Introduction 7
2.2.2. Operating principle of ALD 9
2.2.3. ALD process design 11
2.2.3.1. ALD reactor design 11
2.2.3.2. ALD reactants 12
2.2.3.3. ALD cycle 13
2.3. *In-situ* characterization in ALD 18
2.4. ALD of zirconium nitride (ZrN) 18
2.4.1. Zirconium nitride: Properties and applications 18
2.4.2. ZrN film by ALD 19
2.5. References 20
3. **Experimental Procedure and Characterization Techniques** 30
3.1. Introduction 30
3.2. ALD 150-LX reactor 30
3.3. Experimental Procedures 32
3.3.1. Substrate Preparation 33
3.3.2. Substrate transfer IN/OUT of reactor 33
3.3.3. PEALD of ZrN 34
3.4. Characterization Techniques 34
3.4.1. *In-situ* spectroscopic ellipsometry (*iSE*) 35

3.4.2. X-ray reflectivity (XRR) ... 39
3.4.3. X-ray photoelectron spectroscopy (XPS) ... 40
3.4.4. Van der Pauw sheet resistance ... 41
3.4.5. Optical emission spectroscopy (OES) ... 42
3.5. References ... 43
4. Dynamic *in-situ* SE study of ALD growth initiation ... 46
4.1. Introduction ... 46
4.2. ZrN growth and *d-iSE* acquisition ... 47
4.3. ALD growth modes ... 48
4.4. Bruggeman's EMA to model sub monolayer ALD growth ... 49
4.5. Results and discussion ... 50
4.5.1. Interpretation of measured *d-iSE* data ... 50
4.5.2. ZrN PEALD film properties ... 52
4.5.3. Initial stages of ZrN PEALD growth ... 53
4.6. Summary ... 56
4.7. References ... 56
5. Plasma ALD of conducting ZrN thin films ... 60
5.1. Introduction ... 60
5.2. Experimental Procedure ... 60
5.3. Dynamic *iSE* on ZrN plasma ALD films ... 63
5.3.1. Acquisition and interpretation of *d-iSE* data ... 63
5.3.2. Analysis of *d-iSE* data ... 64
5.4. Results and discussion: ... 65
5.4.1. Growth-per-cycle (GPC) from *iSE* data ... 65
5.4.2. ZrN plasma ALD process optimization ... 67
5.4.2.1. ALD temperature window ... 68
5.4.2.2. ALD cycle optimization ... 70
5.4.3. ZrN PEALD thin film properties ... 72
5.5. Conclusions ... 76
5.6. References ... 77
6. Oxygen contamination in ALD nitride films ... 82
6.1. Introduction ... 82

6.2. Experimental Procedure 83
6.3. Results and discussion 83
6.3.1. Residual H_2O/O_2 in process gases 83
6.3.2. Plasma source related O-contamination 84
6.3.3. Surface Oxidation 87
6.3.4. Oxygen depth-profile 88
6.4. Conclusions 89
6.5. References 89
7. Unconventional ALD: AABAAB… type 93
7.1. Introduction 93
7.2. Growth model for ABAB… type ALD 94
7.2.1. ALD surface reactions 95
7.2.2. ALD film growth 97
7.3. Growth model for AABAAB… type ALD 100
7.4. Results and discussion 105
7.5. Conclusions 106
7.6. References 107
8. Conclusions and Contributions to Knowledge 109
8.1. Conclusions 109
8.2. Contributions to knowledge 111
8.3. References 111
9. Future Directions 113
Bibliography 114

List of Tables

Table 2-1: ALD applications in semiconductor fabrication process................. 8

Table 3-1: Characterization techniques used to evaluate ALD films 35

Table 5-1: Design of experiments to determine optimized process parameters for ZrN PEALD growth. ALD cycle is represented as TDMAZr pulse (t_1) – post-precursor purge (t_2) – plasma pulse (t_3) – post plasma purge (t_4); Substrate temperature (T_{sub}). The optimum range of target parameter obtained in each set was used in the following set. ZrN films were deposited with 600 Watts plasma power and reactant gas composition of (60 sccm forming gas and 100 sccm argon). 67

Table 7-1: Theoretical GPC for AABAAB… growth and ABAB… growth for total precursor dose of 1s and reactant pulse of 9s, with precursor steric factor m_{A-L} = 1.0, 1.5, 2.0 and 4.0... 103

Table 8-1: Electrical resistivity (ρ) of PEALD grown transition metal nitrides on SiO_2. 110

List of Figures

Figure 2-1: ALD of *AB* (reactants $A\text{-}L_n$ and $B\text{-}X_n$) in a continuous flow reactor. Block diagram of a continuous flow reactor, reactant pulsing sequence during a deposition cycle are shown in (a) and (b). Schematic of surface reactions for an "ideal-ALD" are shown in (c) emphasizing upon the consumption and regeneration of surface species ($S{:}B\text{-}X_m$) for a complete deposition cycle with a monolayer growth (thickness d_{mono}).....9

Figure 2-2: (a) Non-linear growth initiation regime for substrate-enhanced and substrate-inhibited growth. (b) Temperature dependent film growth characteristics with temperature window for ALD and PEALD. (c), (d) shows the effect of precursor/reactant dose and inert gas purge on GPC. To compensate for possible disturbances during deposition the excess precursor/reactant dose and longer purge are used than minimum required for self-limiting ALD growth...14

Figure 3-1: Schematic of ALD-150 LX reactor (Kurt J. Lesker Inc.) design showing precursor delivery lines, ICP plasma source, substrate holder and optical ports for in-situ characterization 31

Figure 3-2: In-situ SE for real-time ALD growth studies: (a) Schematics of SE configuration on ALD 150LX reactor (adapted from operation manual, K. J. Lesker); (b) Principle of SE measurement (c) example of SE parameters (Ψ, Δ) measured on native-SiO_2/Si surface. 39

Figure 3-3: Sheet resistance (R_s) from Van der Pauw configuration. 41

Figure 3-4: (a) Optical emission from 600 Watt (60 sccm forming gas + 100 sccm Argon) reactant plasma before and after TDMAZr pulse. Ar plasma is also shown for reference. (b) Additional features in 384.23-389.33 nm range corresponding to CN emissions were observed in the post-

TDMAZr plasma pulse. (c) H-α emission at 656.5 nm shows the presence of atomic H in reactant plasma. For clarity the emission features are shifted along intensity axis..42

Figure 4-1: Partial ALD surface layer with coverage θ and thickness $d_{surface}$ in (a) is represented with B-EMA layer of effective dielectric function ε_{EMA} and thickness $d_{surface}$ in (b). 49

Figure 4-2: The d-iSE parameters (Δ, Ψ) at 4.0 eV measured in the early stages of ZrN PEALD growth. ALD pulse A dna B denotes the TDMAZr pulse and forming gas plasma exposure respectively. 51

Figure 4-3: Imaginary part (ε_2) of the dielectric function for 5.71±0.01 nm thick ZrN PEALD film as determined from iSE data. The Drude (D) and Lorentz (L1 and L2) components are also shown...................................53

Figure 4-4: (a) *d-iSE* parameter Δ measured at 4.0 eV in the early stages of ZrN PEALD on Si(111) substrate; (b) determined ZrN surface monolayer coverage against deposition cycle for first 6 monolayer growth. This ALD film coverage is determined from the analysis of *d-iSE* data using B-EMA approximation in diffusive growth regime. Solid lines are guide to the eye. 55

Figure 5-1: (a) Schematics of spectroscopic ellipsometer M2000DI on ALD150LX reactor chamber along with TDMAZr and forming gas inlets. (b) Deposition cycle for ZrN PEALD. 61

Figure 5-2: The d-iSE parameter Δ measured at 4.0 eV during first 10 cycles of ZrN PEALD. The duration of precursor pulse (t_1), plasma exposure (t_3) and inert gas purges (t_2 and t_4) are shown in upper inset. Lower inset shows iSE parameters (Ψ, Δ) measured on blank substrate (solid line) and after 10 deposition cycles (dotted lines) ever entire range of M2000DI. 64

Figure 5-3: ZrN PEALD film thickness against number of deposition cycles as determined from analysis of *iSE* measurements. An average GPC of 0.103 nm per cycle was obtained in the linear growth regime (dotted line) for 0.12s TDMAZr/15s Ar purge/15s plasma/15s Ar purge, for 600 Watts plasma at 150 °C substrate temperature. (Inset) shows a comparison between the film thickness as derived from *iSE* measurements at 150 °C (solid lines) and ex-situ XRR measurements at RT (dotted lines). 66

Figure 5-4: Average GPC for ZrN deposition as a function of substrate temperature with 0.20s TDMAZr pulse/15s Ar purge/ 15s plasma/ 15s Ar purge. Surface controlled ALD growth was observed in the temperature range of 100-200 °C with an average GPC 0.109 ± 0.005 nm per cycle. 69

Figure 5-5: GPC for ZrN deposition at 150 °C substrate temperature as a function of targeted ALD cycle parameters (a) TDMAZr pulse, (b) plasma exposure length, (c) post-precursor purge, and (d) post-plasma purge. The ALD cycle parameters other than the target parameter are listed in Table 5-1. 71

Figure 5-6: Imaginary part of dielectric function (ε_2) for 35.3 nm thick ZrN PEALD film deposited at 150 °C on Si substrate, as determined from iSE data measured at end of deposition without substrate cooling. Free electron dispersion is represented by Drude term (D) while the Lorentz oscillators (L1 and L2) centered at 4.45 eV and 6.89 eV represents the interband optical transitions. 73

Figure 5-7: XPS survey spectra from 35.5 nm ZrN PEALD film after 3 minutes etching with 4.0 keV Ar^+...74

Figure 5-8: Valance-band XPS spectra of 35.5 nm thick ZrN PEALD film deposited at 150 °C. 75

Figure 5-9: GIXRD patterns at 1° incidence from ZrN PEALD films deposited with (a) 300 cycles at 150 °C and (b) 1200 cycle at 225 °C on Si (111) substrates. 75

Figure 6-1: RGA spectra of process gas (a) Argon, (b) Forming gas (FG), and (c) Nitrogen. An offset has been added to the ordinate axis representing normalized partial pressure of the gas components for clarity. Absolute pressure corresponding to H_2O was found to be within background 1.6 x 10^{-7} Torr in (a)-(c). 84

Figure 6-2: OES spectra in 200-280 nm range, measured at the substrate during (a) Argon, (b) Nitrogen, and (c) reactant gas (forming gas + Argon) plasma. None of the characteristics SiO emission peaks at 229.9 nm, 234.4 nm, 266.9 nm and 269.4 nm could be distinguished from background noise in spectra (a)-(c). 85

Figure 6-3: High resolution XPS core-level O1s and Si2p emission from ZrN PEALD film at 0s, 30s, 150s, and 750s of 4.0 keV Ar ion sputtering. 86

Figure 7-1: Schematic of ALD surface reaction with precursor pulse ($A-L_n$) and the reactant ($B-X_n$) pulse. Dashed lines represent the thickness of ALD grown monolayers (indexed as n=1, 2…). The substrate surface has been indexed as n=0. Surface species are shown with rectangles with superscript denoting the monolayer index. (A, B, L and X are denoted by blue, green, yellow and red spheres respectively) 94

Figure 7-2: Modeled ALD film thickness as a function of deposition cycles obtained from **Eq. (7.6)** and **Eq. (7.7)** for the precursor steric factor (m_{A-L}) varied as 1.0, 1.5, 2.0 and 4.0 assuming no steric hindrance from reactant molecules (m_{B-X} =1). From the linear fit between thickness and number of deposition cycles the determined GPC (units: ML/cycle) is shown as a function of m_{A-L} (Inset). Precursor and reactant pulses along with other surface reaction kinetic parameters were kept the same in these calculations (see text for details). GPC of less than 1 ML/cycle at m_{A-L} =1

suggests that the precursor pulse used in this calculation was shorter than that required for surface saturation 99

Figure 7-3: (a) Precursor ($A\text{-}L_x$) adsorption at surface sites (B-X) with effective shadowed region (S1); (b) decrease in the volume of adsorbed molecules from removal of ligands (L-X); and (c) the reduced steric hindrance (S2) is utilized for step A2 of AABAAB… type deposition. 100

Figure 7-4: Modeled ALD film thickness for AABAAB… (A_1 = 0.5s, A_2 = 0.5s, B = 9s) and ABAB… (A = 1s and B = 9s) type deposition with precursor steric factor $m_{A\text{-}L}$= 4.0. For equivalent precursor dose the calculated GPC of 0.059 ML/cycle with AABAAB… ALD as compared to GPC of 0.048 ML/cycle with ABAB… ALD shows better precursor utilization for proposed AABAAB… cycle...103

Figure 7-5: Simulated ALD saturation curves with respect to precursor dose for AABAAB and ABAB type deposition at (a) $m_{A\text{-}L}$=4.0; (b) $m_{A\text{-}L}$=2.0; (c) $m_{A\text{-}L}$=1.5; and (d) $m_{A\text{-}L}$=1.0. The modeled GPC is obtained at equivalent precursor dose for AABAAB type deposition ($dose_{A1}$ = $dose_{A2}$ = 0.5*$dose_{total}$) and ABAB type deposition ($dose_A$ = $dose_{total}$). 104

Figure 7-6: ALD saturations curves obtained for ZrN deposition using ABAB and AABAAB type deposition. 105

List of Symbols and Abbreviations

ALD : Atomic Layer Deposition

PEALD : Plasma Enhanced Atomic Layer Deposition

ICP : Inductively Coupled Plasma

d-iSE : Dynamic in-situ Spectroscopic Ellipsometry

TDMAZr : Tetrakis dimethylamido Zirconium

FG : Forming gas (5% H_2, 95 % N_2)

Ψ, Δ : Ellipsometry Amplitude ratio and Phase difference

XPS : X-ray Photoelectron Spectroscopy

VB XPS : Valence Band X-ray Photoelectron Spectroscopy

XRR : X-ray Reflectivity

R_S : Sheet Resistance

OES : Optical Emission Spectroscopy

ε : Complex Dielectric Function

θ : Fractional Surface Coverage

GPC : Average Growth per ALD cycle

GIXRD : Glancing Incidence X-ray Diffraction

m : Numerical factor for Sterically Hindered Reaction Sites

1. Introduction

Atomic layer deposition (ALD) of conducting zirconium nitride (ZrN[a]) is essential for applications such as diffusion barrier layer for Cu-interconnects, contact metal in high density memories etc., where uniform deposition of ultrathin ZrN films is required within high-aspect ratio features. Good lattice matching between ZrN (111) and GaN (0001) (lattice constant = 0.316 nm) and small differences between their work function (ϕ^{ZrN} = 4.6 eV [1]; $\phi^{n\text{-}GaN}$ = 4.1 eV [2]) also makes it a potential material for integration with GaN based semiconductor devices.

1.1. Problem Statement

ALD of insulating [3] and conducting [4] ZrN films has been reported in the literature, however the data on conducting ZrN is confounded by the fact that these films were grown directly on silicon substrates without an intervening insulating layer. The ALD growth of ZrN needs further study in order to develop a viable solution for device fabrication. In this research the growth of ZrN via plasma enhanced atomic layer deposition (PEALD) is studied using *in-situ* ellipsometry (*iSE*), and model is developed to understand the growth of these films. In addition, one of the important issues in ALD, namely precursor

---

[a] A variable stoichiometry with respect to N content is exhibited by zirconium nitride films rightly represented as ZrN_x with $1 \leq x \leq 1.33$. In the text the PEALD film is referred as ZrN (neglecting the subscript *x*).

consumption [5], is addressed through novel recipe development. Finally, improved PEALD ZrN will be applied to device fabrication.

1.2. Research Goals

- Interpret and analyze the *d-iSE* data considering partial surface monolayer growth per ALD cycle.
- Study and develop low-temperature PEALD process for the deposition of conducting ZrN films using tetrakis-dimethylamido-zirconium (IV) (TDMAZr) precursor and forming gas (5% H_2 - 95% N_2) reactant plasma.
- Identify the source of O-contamination within PEALD grown ZrN films.
- Develop novel recipes for improved ALD precursor utilization.

1.3. Thesis Outline

The primary objective of this thesis was to develop and study a low-temperature PEALD process for depositing conducting ZrN films. A stable metal-organic Zr precursor (TDMAZr) was selected for its high reactivity and non-corrosive reaction by-products against halogen based precursors. Application of H_2 containing reactant gas plasma was expected to be beneficial in the reduction of zirconium from Zr^{+4} in TDMAZr to Zr^{+3} in the deposited ZrN films as compared to nitrogen or ammonia (NH_3) plasma. The H_2 content (5% H_2) in the reactant gas was determined from the molecular bond dissociation energy (H-H and N-N bond strengths) dependent ionization probabilities.

The literature review on ALD growth is presented in **Chapter 2** emphasizing on the fundamental ALD surface reaction steps and the key elements of ALD process design and in-situ growth characterization. Material properties, deposition techniques and applications of ZrN thin films are briefly discussed in this chapter.

The experimental procedure followed for the growth of ZrN PEALD films are described in **Chapter 3** along with the analytical techniques applied for process optimization and material characterization. Salient features of the ALD reactor (ALD-150 LX, Kurt J. Lesker) and *in-situ* spectroscopic ellipsometer (M2000DI, J. A. Woollam) are discussed here.

The analysis of the dynamic *iSE* (*d-iSE*) data essentially depends upon the physical interpretation of raw data along with the application of appropriate film growth model. In **Chapter 4**, considering a surface diffusion enhanced mode for ZrN PEALD film growth, the surface coverage of ALD film after every deposition cycle is determined from the analysis of *d-iSE* parameters.

Chapter 5 describes the optimization of ZrN film deposition process to attain characteristic self-limiting PEALD growth. An experimental scheme is proposed for ALD process optimization from reduced number of depositions. The material properties of the ZrN films grown with optimized ALD cycle are evaluated and compared with the literature data.

In literature, high concentrations of O have often been reported in nitride ALD films. Although different mechanisms have been discussed for incorporation of O within nitride films, very limited number of studies has been focused on the identification of this contamination source. A study is presented in **Chapter 6** to investigate O contamination source within ZrN PEALD grown films.

One of the most critical issues with ALD in high-volume fabrication is the poor utilization of ALD precursors. In conventional ALD (ABAB… cycle) this precursor utilization and growth-per-cycle (GPC) at saturation is limited by the surface reaction kinetics and the steric factors. A first-principle numerical model for ALD growth is developed in **Chapter 7**, to investigate alternate ALD cycle recipes for efficient precursor consumption.

The key results from the presented work are summarized in **Chapter 8** and the future research directions are described in **Chapter 9**.

1.4. References

[1] Y. Gotoh, H. Tsuji, J. Ishikawa, J. Vac. Sci. Technol. B Microelectron. Nanometer Struct. 21 (2003) 1607.

[2] C. Bae, C. Krug, G. Lucovsky, A. Chakraborty, U. Mishra, Appl. Phys. Lett. 84 (2004) 5413.

[3] J.S. Becker, E. Kim, R.G. Gordon, Chem. Mater. 16 (2004) 3497.

[4] S. Cho, K. Lee, P. Song, H. Jeon, Y. Kim, Jpn. J. Appl. Phys. 46 (2007) 4085.

[5] R.G. Gordon, D. Hausmann, E. Kim, J. Shepard, Chem. Vap. Depos. 9 (2003) 73.

2. Literature Review

2.1. ALD Background

Thin film deposition is an essential process step in the fabrication of modern electronic device components such as semiconductor integrated circuits, solid state memory, LED's, compact batteries, solar cells, micro electro-mechanical systems (MEMS), etc. These deposition techniques are broadly classified as: (a) physical vapor deposition (PVD) and (b) chemical vapor deposition (CVD). In PVD (evaporation, laser ablation, sputtering, etc.), the film growth results from the physical transport of vapour from the source (solid target material or molten pool) to the deposition surface, henceforth referred to as substrate. The directional transport of vapour under high vacuum leads to poor step coverage within non-planar substrate features and $\cos^n\theta$ thickness dependence [1], with θ being the angle between source and substrate normal. In CVD, the chemical reactants are simultaneously introduced into the reactor under a continuous flow of carrier gas and the film growth results from their reaction at the substrate, usually maintained at high temperatures. Although uniform deposition over large planar surface could be attained in CVD [2], inclusion of reaction by-products within growing material and gas-phase reactions pose a serious concern. In addition, the constricted transport of CVD reactants within a non-planar high-aspect ratio features, results in non-conformal deposition.

In modern semiconductor fabrication, deposition of high-k dielectric gates in field-effect transistors [3–5], diffusion barrier/seed layers for Cu interconnects [6], etc., requires the uniform deposition of sub-10 nm thick films. Moreover these films are also required to be free of defects (pinholes, particulate inclusions, etc.) and uniformly cover non-planar high-aspect ratio features, such as through-silicon vias (TSV), deep trenches, etc., spread over large substrate area (> 700 cm^2). With the advent of 450 mm diameter Si wafers in high-volume fabrication the substrate area is expected to increase to ~ 1500 cm^2 [7]. The fundamental limitation with PVD and conventional CVD processes makes them unsuitable for fabrication of these critical features over large deposition area.

2.2. Atomic Layer Deposition (ALD)

2.2.1. An Introduction

Atomic layer deposition (ALD) emerged in the 1960's and 1970's [8,9] as a variation of conventional CVD technique, where the chemical reactants are individually introduced into the reactor in a cyclic sequence [10–14] (i.e. for binary reaction $A+B \rightarrow AB$, the reactant pulsing sequence is ABABAB…with an inert gas purge between every reactant pulse). Although ALD also results from the surface reactions like in CVD, in ALD surface reaction ($A+surface$ or $B+surface$) the active surface reactions sites are consumed on reaction, terminating the reaction on saturation regardless of any excess reactants. This self-limiting ALD surface reaction results in uniform deposition over planar as well as non-planar substrate features. Furthermore, as the ALD surface reactions are self-terminating on saturation, uniform

deposition could be achieved on extremely large substrate areas using sufficient reactant flux to meet surface saturation conditions.

To facilitate removal of excess reactant molecules and by-products of the surface reaction, the ALD reactor is purged with inert gas between successive reactant pulses. This inert gas purging ensures that the ALD grown films are free of particulate inclusion from gas phase reaction and contamination from the incorporation of reaction by-products. This complete reactant pulsing sequence during ALD, i.e. reactant A – inert gas purge – reactant B – inert gas purge, is termed an individual deposition cycle. Since an integral number of deposition cycles are used, ALD offers a sub-nanometer control over deposition thickness in addition to excellent uniformity over entire substrate area.

The earliest efforts in ALD were directed towards deposition of compound thin films for electroluminescent displays [15], interest in ALD was revived by the continuous scaling in semiconductor devices [16] (see **Table 2-1**).

Table 2-1: ALD applications in semiconductor fabrication process

Application	ALD Material	References
High-k dielectric in MOSFET	Al_2O_3, ZrO_2, HfO_2	[3–5]
Metal gate for high-k oxides	HfN, TaN, TiN, TaC	[19–22]
Cu diffusion barrier in interconnects	ZrN, HfN, TiN, TaN	[23–26]
Adhesion layer for metal interconnects	Ru	[27]
Oxides in DRAM trench capacitors	TiO_2, $Al_xTi_{1-x}O_y$, $BaTiO_3$, $SrTiO_3$	[28–31]
Contacts in DRAM trench capacitors	TiN, Ir, W	[19,32,33]

Recently ALD has also been applied in much wider research areas such as nanoparticle coatings, nano-laminates, etc., and advanced devices based on carbon nanotubes, semiconducting nanowires, etc., [17,18].

2.2.2. Operating principle of ALD

ALD of binary compound films (*AB* using $A\text{-}L_n$ and $B\text{-}X_n$) in a continuous flow reactor is schematically represented in **Figure 2-1**. A continuous flow of

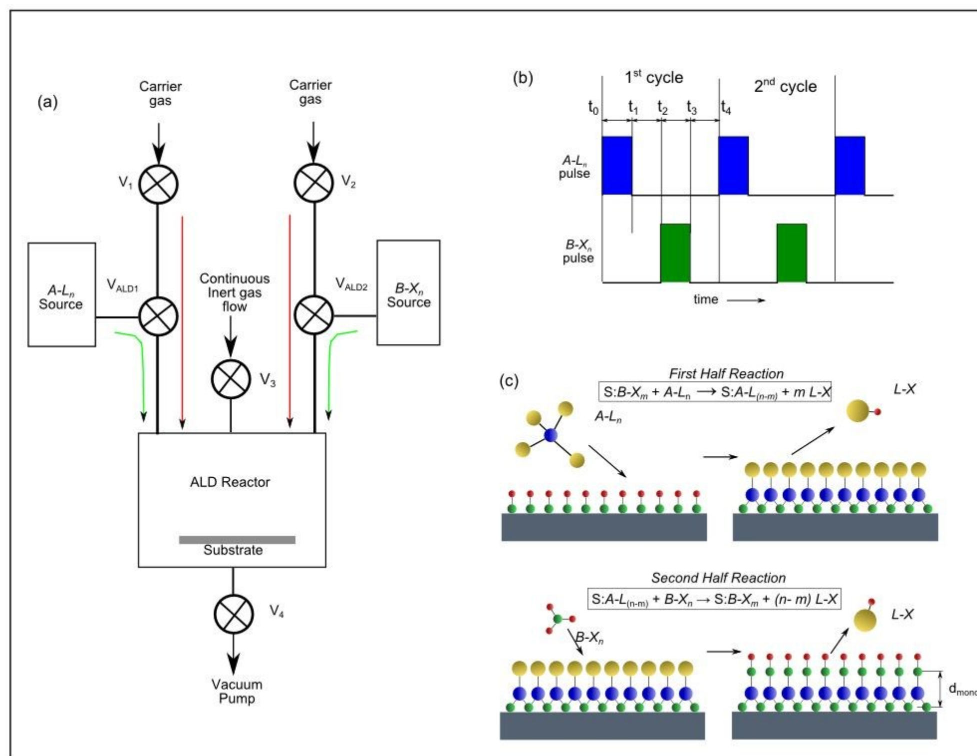

Figure 2-1: ALD of *AB* (reactants $A\text{-}L_n$ and $B\text{-}X_n$) in a continuous flow reactor. Block diagram of a continuous flow reactor, reactant pulsing sequence during a deposition cycle are shown in (a) and (b). Schematic of surface reactions for an "ideal-ALD" are shown in (c) emphasizing upon the consumption and regeneration of surface species ($S{:}B\text{-}X_m$) for a complete deposition cycle with a monolayer growth (thickness d_{mono}).

inert gas is maintained through the deposition chamber and the reactant delivery lines during deposition by keeping valves V_1 - V_4 open as shown in

Figure 2-1(a). This is done primarily to prevent any material build-up from condensation within ALD reactor or delivery lines which would act as a virtual/secondary reactant source. The inert gas flowing through reactant delivery lines also acts as a carrier gas for the transport of ALD reactant molecules to the substrate. Using an electronically controlled 3-port ALD valve (V_{ALD1} and V_{ALD2} normally **OFF**) a precise dose of reactant molecules is released into this carrier gas in form of short pulses, generally for few milliseconds duration.

The typical ALD surface reactions for deposition of *AB* are schematically represented in **Figure 2-1(b)**. In the *first-partial* ALD reaction during $A\text{-}L_n$ pulse ($t_0 \leq t \leq t_1$; V_{ALD1} switched **ON**), the introduced reactant molecules react with the $B\text{-}X_m$ surface reaction sites. At saturation these $B\text{-}X_m$ sites are completely consumed with the generation of $A\text{-}L_{n-m}$ surface species that acts as reaction sites for the following $B\text{-}X_n$ reactant pulse ($t_2 \leq t \leq t_3$; V_{ALD2} switched **ON**). This *second-partial* ALD reaction on saturation entirely consumes the newly formed $A\text{-}L_{n-m}$ surface species and regenerates $B\text{-}X_m$ species at the surface for the following $A\text{-}L_n$ pulse. In between $A\text{-}L_n$ and $B\text{-}X_n$ reactant pulses ($t_1 \leq t \leq t_2$ and $t_3 \leq t \leq t_4$; both V_{ALD1} and V_{ALD2} are **OFF**) the ALD reactor is purged with the continuously flowing inert gas for removal of reaction by-products and excess reactant molecules.

For an "*ideal ALD*" under saturation conditions, a deposition cycle would result in the growth of a complete surface monolayer at the surface with thickness d_{mono} as shown in **Figure 2-1(c)**. However the repulsive interaction

between reactant molecules from steric factors restricts the surface reactions at the adjacent surface active sites. Hence only a partial monolayer growth per deposition cycle is obtained, even in the case of "near-ideal" $AlMe_3/H_2O$ ALD of Al_2O_3 [12].

2.2.3. ALD process design

ALD has a fundamental upper-limit of a monolayer deposition per cycle; however in practice the observed film growth is typically ~0.05-0.10 nm per cycle because of the partial monolayer growth. Moreover the utilization of chemical reactants in ALD surface reaction is rather poor, since only a fraction of the introduced reactant molecules reach the substrate and only fraction of these undergoes surface reaction depending upon their respective reactivity. Furthermore, at saturation the respective surface reaction terminates and any excess reactant species is pumped out of the reactor during inert gas purging. Hence an overall efficiency of ALD process depends upon (1) ALD reactor design; (2) selection of ALD reactants; and (3) ALD cycle optimization.

2.2.3.1. ALD reactor design

Reactor design is a crucial component of ALD process since it essentially governs the transport of reactant species from source to the substrate. Also only a part of the total reactant molecules introduced in the reactor arrive at the substrate, while the rest remains unutilized and are pumped out of the reactor along with reaction by-products during the following inert gas purge. This unutilized fraction of reactant molecules depends upon the reactor geometry and its volume. An ALD reactor with optimum volume not only

maximizes reactant utilization but also requires shorter inert gas purge to pump out surface reaction by-products. Additional features such as maintaining a plug-flow throughout the reactor and application of strategies for confining reactant flux close to the substrate region significantly improves the efficiency of reactant transport at the substrate and also prevents parasitic ALD reactions away from substrate.

2.2.3.2. ALD reactants

The chemical reactants for ALD could be broadly divided into metallic and non-metallic reactants, henceforth referred to as metal-precursors and reactants respectively [14]. The metal precursors are further classified as *inorganic* (non-carbon), *organometallics* (metal-carbon bond) and *metal-organics* (no metal-carbon bonds). The non-metallic ALD reactants mainly consist of hydrides (NH_3, H_2O, etc.) or molecular species (N_2, O_2, O_3, etc.). Selection of precursor-reactant combination for an ALD process is based upon their vapour pressure, relative reactivity and thermal stability.

The halogen based ALD precursors are avoided due to corrosive/reactive nature of their reaction by-products. Also the contamination from halide inclusion adversely affects the film properties. The stable molecular reactants (O_2, N_2, NH_3, H_2, etc.) require high substrate temperature for acceptable ALD growth rates, thus preventing their application for deposition on temperature sensitive substrates. Use of molecular reactants with higher chemical reactivity (O_3 [34–36]; N_2H_4 [37]) has been reported, however their application introduces additional constraints on ALD process design.

Plasma enhanced ALD (PEALD) involves application of plasma discharge to decompose molecular reactants into highly reactive components, such as electrons, ions, radicals, molecular fragments, etc., [38, 39]. PEALD thus enables the use of stable reactants for deposition at lower substrate temperatures compared to conventional ALD, henceforth referred to as thermal ALD [25, 40]. The reduction in the required substrate temperature permits ALD on thermally sensitive substrates and also application of precursors with low temperature for self-decomposition. Additional plasma parameters [41–43] provide further flexibility in PEALD process design and control over material properties of deposited films [22–24, 44–47]. Effect of pre- and post- deposition plasma treatment on the interface and the quality of ALD films has also been studied [48–50].

2.2.3.3. ALD cycle

For a selected precursor/reactant combination, deposition cycle parameters such as the substrate temperature, dose of precursor/reactant molecules, inert gas purge durations are required to be optimized to attain self-limiting ALD growth. Plasma power and plasma gas composition are additional parameters to be optimized for PEALD. Dependence of ALD growth on these parameters is schematically presented in **Figure 2-2**.

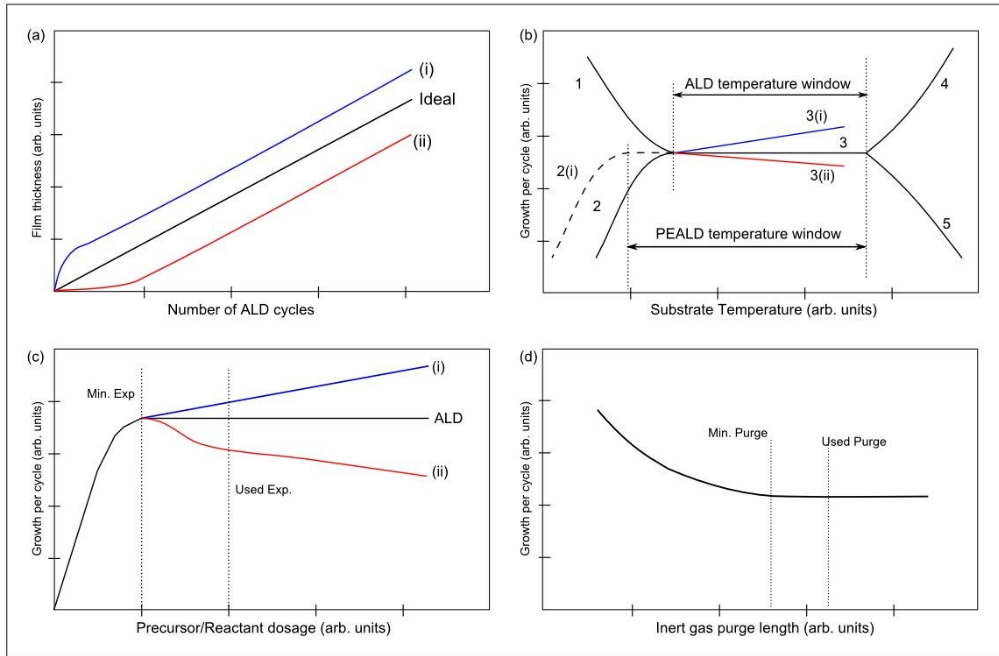

Figure 2-2: (a) Non-linear growth initiation regime for substrate-enhanced and substrate-inhibited growth. (b) Temperature dependent film growth characteristics with temperature window for ALD and PEALD. (c), (d) shows the effect of precursor/reactant dose and inert gas purge on GPC. To compensate for possible disturbances during deposition the excess precursor/reactant dose and longer purge are used than minimum required for self-limiting ALD growth.

A linear increase in film thickness with the number of deposition cycles is a characteristic of recurring surface reactions over each ALD cycle. In the growth initiation/nucleation stage, i.e. over first few deposition cycles, ALD reaction occurs on the bare substrate surface, while in the later-stages or steady-state these surface reactions takes place over the underlying ALD grown film. A change in the surface reaction kinetics from the initiation-stages to steady-stages of ALD is often observed as a transition from non-linear to linear growth regime [51]. The two extremes of the non-linear growth trends resulting from (i) substrate-enhanced growth and (ii) substrate-inhibited growth are shown in **Figure 2-2(a)** along with an ideal substrate- independent growth. For the steady-state linear-growth regime, the slope of film thickness

versus the number of ALD cycle is related to the amount of material deposited per cycle. This slope, termed as growth-per-cycle (GPC), is a useful parameter to evaluate ALD process.

Substrate temperature (T_{sub}) is a critical ALD parameter that governs residence time for precursor/reactant molecules on the surface and reaction kinetics. It also provides a control over undesired/secondary reactions resulting from either condensation or decomposition of precursor/reactant species at the surface. In experimental determination of these film growth characteristics, an arbitrarily high dose of both precursor and reactant species is used to ensure that the surface reactions are not limited by the supply of precursor/reactant molecules. Furthermore, arbitrarily long inert gas purges are utilized to ensure that the reaction by-products and any excess unreacted molecules are completely pumped out of the reactor without affecting the film growth. The temperature dependent film growth features are represented as type 1 – 5 in **Figure 2-2(b)** and discussed below:

Low temperature range: Type-1 growth arises from the condensation of precursor/reactant at the substrate surface and is observed as a decrease in GPC with increasing T_{sub}. Type-2 is the characteristic of film growth limited by the activation energy for surface reaction, where higher T_{sub} favours the surface reaction resulting in higher GPC.

High temperature range: Type-4 growth primarily results from the decomposition of precursor molecules at the substrate such that the deposition

is no longer controlled by the availability of surface reaction sites. An increase in GPC with T_{sub} for type-4 growth is because of the increased precursor decomposition at higher temperature, similar to a CVD. However the type-5 growth results from the decrease in the residence time of precursor/reactant species at the substrate with T_{sub}. The limited surface reactions because of the shorter residence time at higher T_{sub} results in lower GPC.

Intermediate temperature range: Type-3 growth represents surface reaction controlled self-limiting ALD film growth and this temperature range is termed the "ALD temperature-window". Most often the upper-limit of this temperature window is determined by the decomposition temperature for metal precursor, while the lower-limit is governed by the slowest of the ALD partial reactions (often involving stable molecular reactants). Plasma activation of reactants in PEALD extends the ALD temperature window by decreasing this lower-limit, as shown by type-2(i).

Although within the permissible temperature range the GPC for ALD is often considered to be independent of T_{sub}, weak temperature dependence leading to type-3(i) or type-3(ii) growth has also been reported [12]. For deposition of multi-component structures such as ternary or quaternary compounds, multilayered film structures, etc., it is essential that there exists a significant overlap of the ALD temperature windows of each component.

In order to attain self-limiting growth conditions in the ALD temperature window, a minimum dose of precursor/reactant molecules is necessary such

that all of the available surface reaction sites are consumed during the respective partial reactions. Any excess dose beyond the minimum for surface saturation does not affect GPC as shown in **Figure 2-2(c)**. In order to compensate for any disturbance in the delivery of precursor/reactant pulses or any other conditions during deposition process, higher doses than the minimum are generally used. A non-steady value of GPC with increasing dosage suggests that either the self-limiting condition has not been met or possibility of a non-ALD type growth and calls for adjustments in other process parameters. For example as shown in **Figure 2-2(c)**, the type-(i) growth indicates either condensation or decomposition of precursor/reactant species while the type-(ii) growth is typical etching related phenomenon. An initial decrease in GPC followed by a steady value with respect to reactant exposures indicates either incomplete removal of ligands on precursor at low reactant dose [52] or the amorphous-to-polycrystalline phase transformation with increased reactant dose [22].

A minimum inert gas purge is essential to ensure complete removal of the surface reaction by-products along with excess of precursor/reactant molecules from the reactor between consecutive ALD partial reactions as shown in **Figure 2-2(d)**. This minimum purge depends upon the volatility of reaction by-products and the reactor volume. Higher GPC for purge lengths shorter than this minimum is due to inclusion of the ALD reaction by-products and/or gas-phase reaction products into the growing film. For ALD precursor/reactants with short residence time within reactor and highly volatile reaction by-products, the following purge step could be completely eliminated

[42]. To compensate for any disturbance during deposition process inert gas purges are maintained at longer than the minimum duration.

2.3. *In-situ* characterization in ALD

ALD growth has been extensively studied using thin film characterization techniques such as electron microscopy, x-ray techniques, optical spectroscopy, IR spectrometry, Rutherford backscattering (RBS), electrical measurements, etc., [53–58]. A great amount of effort has been spent towards the development of fundamental understanding of ALD growth mechanisms. As the overall deposition proceeds in discrete steps of self-terminating saturated partial reactions, ALD provides an excellent opportunity for detailed study of surface reaction and growth mechanisms with *in-situ* characterization techniques such as quartz-crystal microbalance (QCM), quadruple mass spectrometry (QMS), spectroscopic ellipsometry (SE), etc. [59–63]. These *in-situ* studies would have a major role in the development and validation of theoretical ALD growth models [51,64–69]. Moreover, real-time control and optimization of ALD process using *in-situ* diagnostics have also been reported [70–74].

2.4. ALD of zirconium nitride (ZrN)

2.4.1. Zirconium nitride: Properties and applications

Zirconium nitride (ZrN), a Group IV transition metal nitride, is a refractory material with a golden yellow color appearance, a melting point of 2980 ^{0}C and Vickers hardness of 15.0 GPa [75]. It has a f.c.c. B1 structure (NaCl - type) with a lattice constant of 0.4567 nm where Zr forms the f.c.c. lattice and

N occupies the octahedral sites. Although near-stoichiometric nitride, ZrN (*N:Zr* ≈ 1) is the most stable phase under ambient conditions, N-rich metastable phases with 1.06 ≤ *N:Zr* ≤ 1.33 resulting from Zr-vacancies have also been reported [76]. The stoichiometry dependent transition from metallic (ZrN, electrical resistivity ~13.6 μΩ-cm) to transparent insulating (Zr_3N_4, band gap of ~ 2.2 eV) phase has been subject of several theoretical [77–82] and experimental [83–87] studies.

The low electrical resistivity and high melting temperature of ZrN makes it a promising material for applications in semiconductor device fabrication such as a diffusion barrier for Cu interconnects [88–91], advanced 3D-ICs [92], as a gate and source-drain contact for III-V semiconductor MOSFET's [93,94] and as a metal contact in trench capacitors for high density memory [95]. Other applications of ZrN films includes wear resistant coatings [96–98]; optical coatings [99,100], functional multilayer structures [101], high temperature superconductors [102], thermoelectrics [103,104], etc.

2.4.2. ZrN film by ALD

Modulation of ZrN stoichiometry between the metallic (ZrN) and insulating (Zr_3N_4) phase has been demonstrated using PVD techniques such as reactive sputtering, ion beam assisted deposition, etc., by controlling deposition parameters [105–113]. ZrN CVD films at low temperatures predominantly consisted of the Zr_3N_4 phase [114–118]. The lowest electrical resistivity of 1100 μΩ-cm was reported for plasma CVD of ZrN at 400 °C with an electrical bias [117]. Thermal ALD of ZrN films with NH_3 as the N-source primarily

resulted in deposition of the insulating phase [119]. PEALD of low resistivity ZrN films using N_2 plasma at 300 °C have been presented in [88], however the reported resistivity was measured for ZrN films deposited on Si without an insulating layer. ALD studies of ZrN films are limited [88,119,120] and the factors affecting the growth of the metallic or insulating phase are not well understood. Semiconductor device applications such as Cu-diffusion barrier and metal contacts for high density memories would require controlled deposition of conducting ZrN films within high aspect-ratio features. This is the primary motivation, which justifies study of ZrN PEALD process.

2.5. References

[1] M. Ohring, Materials Science of Thin Films: Deposition and Structure, 2nd ed, Academic Press, San Diego, CA, 2002.

[2] H. Komiyama, Y. Shimogaki, Y. Egashira, Chem. Eng. Sci. 54 (1999) 1941.

[3] J.W. Lim, S.J. Yun, Electrochem. Solid-State Lett. 7 (2004) F45.

[4] Y. Kim, J. Koo, J. Han, S. Choi, H. Jeon, C.-G. Park, J. Appl. Phys. 92 (2002) 5443.

[5] J. Kim, S. Kim, H. Jeon, M.-H. Cho, K.-B. Chung, C. Bae, Appl. Phys. Lett. 87 (2005) 053108.

[6] A.E. Kaloyeros, E. Eisenbraun, Annu. Rev. Mater. Sci. 30 (2000) 363.

[7] International Technology Roadmap for Semiconductors, 2012.

[8] A.M. Shevjakov, G.N. Kuznetsova, V.B. Aleskovskii, in:, High Temp. Chem. Oxides, Lenin- grad, USSR (Nauka, Leningrad, USSR, 1967), 1965, pp. 149–155.

[9] J. Antson, T. Suntola, Method for Producing Compound Thin Films, 4,058,430, 1977.

[10] M. Ritala, J. Niinistö, in:, A.C. Jones, M.L. Hitchman (Eds.), Chem. Vap. Depos., Royal Society of Chemistry, Cambridge, 2009, pp. 158–206.

[11] S.M. George, A.W. Ott, J.W. Klaus, J. Phys. Chem. 100 (1996) 13121.

[12] R.L. Puurunen, J. Appl. Phys. 97 (2005) 121301.

[13] S.M. George, Chem. Rev. 110 (2010) 111.

[14] V. Miikkulainen, M. Leskelä, M. Ritala, R.L. Puurunen, J. Appl. Phys. 113 (2013) 021301.

[15] T. Suntola, Mater. Sci. Rep. 4 (1989) 261.

[16] O. Sneh, R.B. Clark-Phelps, A.R. Londergan, J. Winkler, T.E. Seidel, Thin Solid Films 402 (2002) 248.

[17] H. Kim, H.-B.-R. Lee, W.-J. Maeng, Thin Solid Films 517 (2009) 2563.

[18] M. Leskelä, M. Kemell, K. Kukli, V. Pore, E. Santala, M. Ritala, J. Lu, Mater. Sci. Eng. C 27 (2007) 1504.

[19] P. Caubet, T. Blomberg, R. Benaboud, C. Wyon, E. Blanquet, J.-P. Gonchond, M. Juhel, P. Bouvet, M. Gros-Jean, J. Michailos, C. Richard, B. Iteprat, J. Electrochem. Soc. 155 (2008) H625.

[20] S. Consiglio, W. Zeng, N. Berliner, E.T. Eisenbraun, J. Electrochem. Soc. 155 (2008) H196.

[21] T.-H. Kim, T.-K. Eom, S.-H. Kim, D.-H. Kang, H. Kim, S. Yu, J.M. Lim, Electrochem. Solid-State Lett. 14 (2011) D89.

[22] J.-S. Park, H.-S. Park, S.-W. Kang, J. Electrochem. Soc. 149 (2002) C28.

[23] S. Cho, K. Lee, P. Song, H. Jeon, Y. Kim, Jpn. J. Appl. Phys. 46 (2007) 4085.

[24] J. Wooho, J. Korean Phys. Soc. 56 (2010) 905.

[25] J. Musschoot, Q. Xie, D. Deduytsche, S. Van den Berghe, R.L. Van Meirhaeghe, C. Detavernier, Microelectron. Eng. 86 (2009) 72.

[26] H.C.M. Knoops, L. Baggetto, E. Langereis, M.C.M. van de Sanden, J.H. Klootwijk, F. Roozeboom, R.A.H. Niessen, P.H.L. Notten, W.M.M. Kessels, J. Electrochem. Soc. 155 (2008) G287.

[27] O.-K. Kwon, S.-H. Kwon, H.-S. Park, S.-W. Kang, J. Electrochem. Soc. 151 (2004) C753.

[28] Q. Xie, J. Musschoot, D. Deduytsche, R.L. Van Meirhaeghe, C. Detavernier, S. Van den Berghe, Y.-L. Jiang, G.-P. Ru, B.-Z. Li, X.-P. Qu, J. Electrochem. Soc. 155 (2008) H688.

[29] J.W. Lim, S.J. Yun, H.-T. Kim, J. Electrochem. Soc. 154 (2007) G239.

[30] M. Vehkamäki, Electrochem. Solid-State Lett. 2 (1999) 504.

[31] N. Menou, X.P. Wang, B. Kaczer, W. Polspoel, M. Popovici, K. Opsomer, M.A. Pawlak, W. Knaepen, C. Detavernier, T. Blomberg, D. Pierreux, J. Swerts, J.W. Maes, P. Favia, H. Bender, B. Brijs, W. Vandervorst, S. Van Elshocht, D.J. Wouters, S. Biesemans, J.A. Kittl, in:, IEEE, 2008, pp. 1–4.

[32] S.-W. Kim, S.-H. Kwon, S.-J. Jeong, J.-S. Park, S.-W. Kang, Electrochem. Solid-State Lett. 11 (2008) H303.

[33] J.. Elam, C.. Nelson, R.. Grubbs, S.. George, Surf. Sci. 479 (2001) 121.

[34] J.B. Kim, D.R. Kwon, K. Chakrabarti, C. Lee, K.Y. Oh, J.H. Lee, J. Appl. Phys. 92 (2002) 6739.

[35] Y. Senzaki, S. Park, H. Chatham, L. Bartholomew, W. Nieveen, J. Vac. Sci. Technol. Vac. Surf. Films 22 (2004) 1175.

[36] X. Liu, S. Ramanathan, A. Longdergan, A. Srivastava, E. Lee, T.E. Seidel, J.T. Barton, D. Pang, R.G. Gordon, J. Electrochem. Soc. 152 (2005) G213.

[37] B.B. Burton, A.R. Lavoie, S.M. George, J. Electrochem. Soc. 155 (2008) D508.

[38] H. Kim, Thin Solid Films 519 (2011) 6639.

[39] H.B. Profijt, S.E. Potts, M.C.M. van de Sanden, W.M.M. Kessels, J. Vac. Sci. Technol. Vac. Surf. Films 29 (2011) 050801.

[40] K.-H. Kim, N.-W. Kwak, S.H. Lee, Electron. Mater. Lett. 5 (2009) 83.

[41] J. Kim, S. Kim, H. Kang, J. Choi, H. Jeon, M. Cho, K. Chung, S. Back, K. Yoo, C. Bae, J. Appl. Phys. 98 (2005) 094504.

[42] J. Swerts, A. Delabie, M.M. Salimullah, M. Popovici, M.-S. Kim, M. Schaekers, S. Van Elshocht, ECS Solid State Lett. 1 (2012) P19.

[43] H.B. Profijt, P. Kudlacek, M.C.M. van de Sanden, W.M.M. Kessels, J. Electrochem. Soc. 158 (2011) G88.

[44] E.-J. Kim, D.-H. Kim, Electrochem. Solid-State Lett. 9 (2006) C123.

[45] S.-J. Park, W.-H. Kim, H.-B.-R. Lee, W.J. Maeng, H. Kim, Microelectron. Eng. 85 (2008) 39.

[46] W.J. Maeng, H. Kim, Electrochem. Solid-State Lett. 9 (2006) G191.

[47] J.W. Lim, S.J. Yun, J.H. Lee, Electrochem. Solid-State Lett. 7 (2004) F73.

[48] D.H. Triyoso, R.I. Hegde, J. Grant, P. Fejes, R. Liu, D. Roan, M. Ramon, D. Werho, R. Rai, L.B. La, J. Baker, C. Garza, T. Guenther, B.E.

White, P.J. Tobin, J. Vac. Sci. Technol. B Microelectron. Nanometer Struct. 22 (2004) 2121.

[49] H.-L. Lu, L. Sun, S.-J. Ding, M. Xu, D.W. Zhang, L.-K. Wang, Appl. Phys. Lett. 89 (2006) 152910.

[50] J.-H. Yun, E.-S. Choi, C.-M. Jang, C.-S. Lee, Jpn. J. Appl. Phys. 41 (2002) L418.

[51] M.A. Alam, M.L. Green, J. Appl. Phys. 94 (2003) 3403.

[52] Z. Fang, P.A. Williams, R. Odedra, H. Jeon, R.J. Potter, J. Cryst. Growth 338 (2012) 111.

[53] M.L. Huang, Y.C. Chang, C.H. Chang, Y.J. Lee, P. Chang, J. Kwo, T.B. Wu, M. Hong, Appl. Phys. Lett. 87 (2005) 252104.

[54] T. Aaltonen, M. Ritala, M. Leskelä, Electrochem. Solid-State Lett. 8 (2005) C99.

[55] E. Eisenbraun, O. van der Straten, Yu Zhu, K. Dovidenko, A. Kaloyeros, in:, IEEE, 2001, pp. 207–209.

[56] J. Aarik, H. Mändar, M. Kirm, L. Pung, Thin Solid Films 466 (2004) 41.

[57] D.M. Hausmann, E. Kim, J. Becker, R.G. Gordon, Chem. Mater. 14 (2002) 4350.

[58] M.D. Groner, J.W. Elam, F.H. Fabreguette, S.M. George, Thin Solid Films 413 (2002) 186.

[59] K. Knapas, M. Ritala, Crit. Rev. Solid State Mater. Sci. 38 (2013) 167.

[60] H. Tiznado, M. Bouman, B.-C. Kang, I. Lee, F. Zaera, J. Mol. Catal. Chem. 281 (2008) 35.

[61] C.L. Platt, N. Li, K. Li, T.M. Klein, Thin Solid Films 518 (2010) 4081.

[62] R. Methaapanon, S.M. Geyer, S. Brennan, S.F. Bent, Chem. Mater. 25 (2013) 3458.

[63] A. Yanguas-Gil, J.A. Libera, J.W. Elam, ECS Trans. 50 (2013) 43.

[64] S.D. Elliott, in:, M. Fanciulli, G. Scarel (Eds.), Rare Earth Oxide Thin Films, Springer Berlin Heidelberg, 2007, pp. 73–86.

[65] H.-S. Park, J.-S. Min, J.-W. Lim, S.-W. Kang, Appl. Surf. Sci. 158 (2000) 81.

[66] R.L. Puurunen, Chem. Vap. Depos. 9 (2003) 249.

[67] R.L. Puurunen, Chem. Vap. Depos. 10 (2004) 159.

[68] R.L. Puurunen, W. Vandervorst, W.F.A. Besling, O. Richard, H. Bender, T. Conard, C. Zhao, A. Delabie, M. Caymax, S. De Gendt, M. Heyns, M.M. Viitanen, M. de Ridder, H.H. Brongersma, Y. Tamminga, T. Dao, T. de Win, M. Verheijen, M. Kaiser, M. Tuominen, J. Appl. Phys. 96 (2004) 4878.

[69] R.L. Puurunen, W. Vandervorst, J. Appl. Phys. 96 (2004) 7686.

[70] E. Langereis, S.B.S. Heil, H.C.M. Knoops, W. Keuning, M.C.M. van de Sanden, W.M.M. Kessels, J. Phys. Appl. Phys. 42 (2009) 073001.

[71] W. Lei, L. Henn-Lecordier, M. Anderle, G.W. Rubloff, M. Barozzi, M. Bersani, J. Vac. Sci. Technol. B Microelectron. Nanometer Struct. 24 (2006) 780.

[72] L. Henn-Lecordier, W. Lei, M. Anderle, G.W. Rubloff, J. Vac. Sci. Technol. B Microelectron. Nanometer Struct. 25 (2007) 130.

[73] J. Niinistö, A. Rahtu, M. Putkonen, M. Ritala, M. Leskelä, L. Niinistö, Langmuir 21 (2005) 7321.

[74] R. Matero, A. Rahtu, M. Ritala, Chem. Mater. 13 (2001) 4506.

[75] H.O. Pierson, in:, Handb. Refract. Carbides Nitrides Prop. Charact. Process. Appl., Noyes Publications, Park Ridge, N.J, 1996.

[76] L. Gribaudo, D. Arias, J. Abriata, J. Phase Equilibria 15 (1994) 441.

[77] A.L. Ivanovskii, N.I. Medvedeva, S.V. Okatov, Inorg. Mater. 37 (2001) 459.

[78] W. Ching, Y.-N. Xu, L. Ouyang, Phys. Rev. B 66 (2002).

[79] Q.-X. Guo, W.-K. Kwan, X.-L. Cheng, H. Zhang, Phys. Status Solidi B 247 (2010) 67.

[80] J. Adachi, K. Kurosaki, M. Uno, S. Yamanaka, J. Alloys Compd. 396 (2005) 260.

[81] T. Chihi, M. Fatmi, B. Ghebouli, M. Guemmaz, Solid State Sci. 13 (2011) 1414.

[82] D.I. Bazhanov, A.A. Knizhnik, A.A. Safonov, A.A. Bagatur'yants, M.W. Stoker, A.A. Korkin, J. Appl. Phys. 97 (2005) 044108.

[83] L. Porte, Solid State Commun. 50 (1984) 303.

[84] P. Prieto, J. Vac. Sci. Technol. Vac. Surf. Films 14 (1996) 3181.

[85] P. Prieto, A. Fernández, L. Soriano, F. Yubero, E. Elizalde, A. González-Elipe, J. Sanz, Phys. Rev. B 51 (1995) 17984.

[86] J.. Sanz, L. Soriano, P. Prieto, G. Tyuliev, C. Morant, E. Elizalde, Thin Solid Films 332 (1998) 209.

[87] P. Carvalho, J.M. Chappé, L. Cunha, S. Lanceros-Méndez, P. Alpuim, F. Vaz, E. Alves, C. Rousselot, J.P. Espinós, A.R. González-Elipe, J. Appl. Phys. 103 (2008) 104907.

[88] S. Cho, K. Lee, P. Song, H. Jeon, Y. Kim, Jpn. J. Appl. Phys. 46 (2007) 4085.

[89] M.B. Takeyama, A. Noya, K. Sakanishi, J. Vac. Sci. Technol. B Microelectron. Nanometer Struct. 18 (2000) 1333.

[90] C.-S. Chen, C.-P. Liu, H.-G. Yang, C.Y.A. Tsao, J. Vac. Sci. Technol. B Microelectron. Nanometer Struct. 22 (2004) 1075.

[91] L.C. Leu, P. Sadik, D.P. Norton, L. McElwee-White, T.J. Anderson, J. Vac. Sci. Technol. B Microelectron. Nanometer Struct. 26 (2008) 1723.

[92] W.R. Davis, J. Wilson, S. Mick, Jian Xu, Hao Hua, C. Mineo, A.M. Sule, M. Steer, P.D. Franzon, IEEE Des. Test Comput. 22 (2005) 498.

[93] J. Westlinder, J. Malmström, G. Sjöblom, J. Olsson, Solid-State Electron. 49 (2005) 1410.

[94] S.E. Mohney, B.P. Luther, S.D. Wolter, T.N. Jackson, R.F. Karlicek, R.S. Kern, in High Temp. Electron. Conf. 1998 HITEC 1998 Fourth Int., IEEE, 1998, pp. 134–137.

[95] S. Horita, T. Toda, H. Kasagawa, J. Korean Phys. Soc. 42 (2003) 1142.

[96] K.. Gruss, R.. Davis, Surf. Coat. Technol. 114 (1999) 156.

[97] G.W. Egeland, K. Wheeler, P. Peralta, K.J. McClellan, S.A. Maloy, G.M. Bond, J. Nucl. Mater. 416 (2011) 253.

[98] A. Fragiel, M.H. Staia, J. Muñoz-Saldaña, E.S. Puchi-Cabrera, C. Cortes-Escobedo, L. Cota, Surf. Coat. Technol. 202 (2008) 3653.

[99] K. Andersson, M. Veszelei, A. Roos, Sol. Energy Mater. Sol. Cells 32 (1994) 199.

[100] V. Braic, M. Balaceanu, M. Braic, in:, IEEE, 2008, pp. 267–270.

[101] W.J. Meng, J. Vac. Sci. Technol. Vac. Surf. Films 10 (1992) 1610.

[102] I. Hase, Y. Nishihara, Phys. Rev. B 60 (1999) 1573.

[103] J. Adachi, K. Kurosaki, M. Uno, S. Yamanaka, J. Alloys Compd. 399 (2005) 242.

[104] B. Saha, J. Acharya, T.D. Sands, U.V. Waghmare, J. Appl. Phys. 107 (2010) 033715.

[105] N. Farkas, G. Zhang, R.D. Ramsier, E.A. Evans, J.A. Dagata, J. Vac. Sci. Technol. Vac. Surf. Films 26 (2008) 297.

[106] S.A. Barnett, L. Hultman, J.-E. Sundgren, F. Ronin, S. Rohde, Appl. Phys. Lett. 53 (1988) 400.

[107] K. DongHo, K. ChulMin, K. EunHong, S. YoungChul, K. TaeGeun, R. CheongHyun, H. Cheol-Koo, J. Korean Phys. Soc. 55 (2009) 1149.

[108] B.O. Johansson, H.T.G. Hentzell, J.M.E. Harper, J.J. Cuomo, J. Mater. Res. 1 (2011) 442.

[109] H.. Benia, M. Guemmaz, G. Schmerber, A. Mosser, J.-C. Parlebas, Appl. Surf. Sci. 200 (2002) 231.

[110] R.P. Netterfield, P.J. Martin, D.R. McKenzie, J. Mater. Sci. Lett. 9 (1990) 972.

[111] A. Straboni, L. Pichon, T. Girardeau, Surf. Coat. Technol. 125 (2000) 100.

[112] L. Pichon, T. Girardeau, A. Straboni, F. Lignou, P. Guérin, J. Perrière, Appl. Surf. Sci. 150 (1999) 115.

[113] S. Horita, J. Vac. Sci. Technol. Vac. Surf. Films 11 (1993) 2452.

[114] K. Sugiyama, J. Electrochem. Soc. 122 (1975) 1545.

[115] D.M. Hoffman, Polyhedron 13 (1994) 1169.

[116] R. Fix, R.G. Gordon, D.M. Hoffman, Chem. Mater. 3 (1991) 1138.

[117] H. Wendel, H. Suhr, Appl. Phys. Solids Surf. 54 (1992) 389.

[118] P. Hasan, S.E. Potts, C.J. Carmalt, R.G. Palgrave, H.O. Davies, Polyhedron 27 (2008) 1041.

[119] J.S. Becker, E. Kim, R.G. Gordon, Chem. Mater. 16 (2004) 3497.

[120] H. Tiznado, M. Bouman, B.-C. Kang, I. Lee, F. Zaera, J. Mol. Catal. Chem. 281 (2008) 35.

3. Experimental Procedure and Characterization Techniques

3.1. Introduction

This chapter describes the experimental procedure followed for the deposition of ZrN PEALD films. The salient features of the ALD 150-LX deposition system are discussed followed by the substrate preparation, pre-deposition treatment and film deposition steps. The analytical techniques used to characterize growth and material properties of the ZrN PEALD films are discussed in the later part of this chapter.

3.2. ALD 150-LX reactor

Film depositions were performed in a fully automated, lab-scale continuous flow cylindrical reactor ALD-150 LX (Kurt J. Lesker Inc.) as schematically shown in **Figure 3-1**, with capability to simultaneously accommodate up to 4 different metal precursors along with a H_2O source and a reactant gas. A continuous plugged-flow of inert gas is maintained in the reactor during deposition to facilitate transport of introduced precursor/reactant species towards the substrate. An additional inert gas flow is used to create a curtain/barrier layer to confine precursor/reactant flux close to substrate and prevent parasitic depositions on reactor side-walls. The delivery lines are provided with a steady flow of inert gas that acts as a carrier for precursor/reactant molecules and also prevents any material build up within

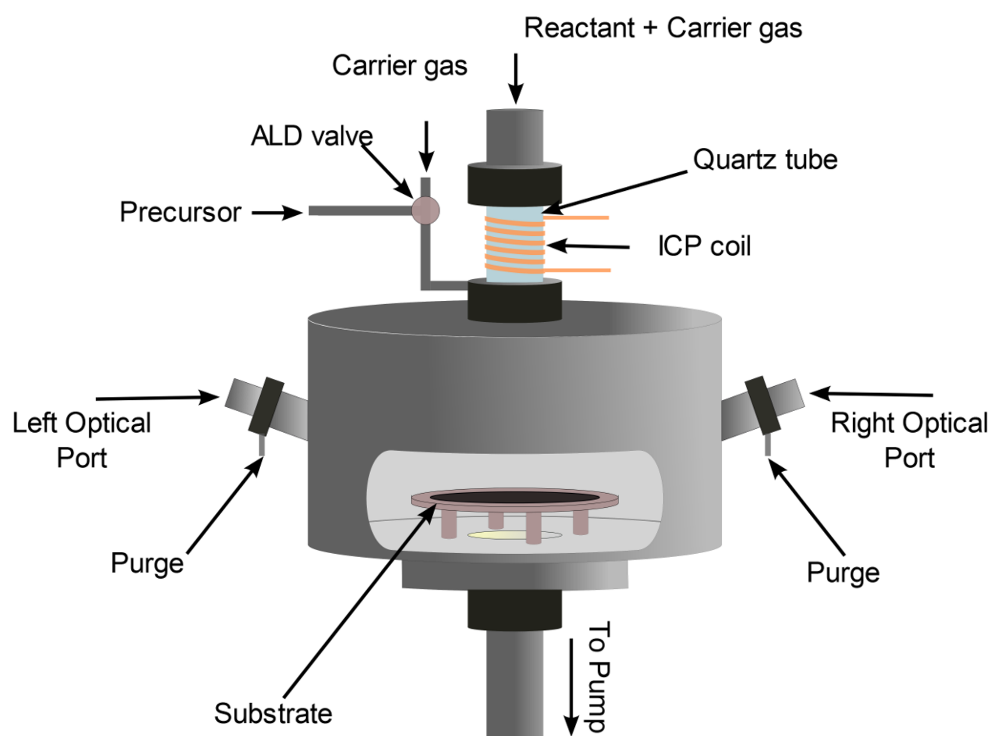

Figure 3-1: Schematic of ALD-150 LX reactor (Kurt J. Lesker Inc.) design showing precursor delivery lines, ICP plasma source, substrate holder and optical ports for in-situ characterization

the lines. Total inert gas flow (~0.4 Torr in idle-state and ~1 Torr during ALD) within the chamber is regulated by electronic mass flow controllers (MKS Instruments). To avoid material condensation within the delivery lines and/or on the inside walls of the reactor, these are kept at higher temperatures (~100-150 °C).

A precise dose of precursor/reactant molecules is pulsed into the carrier gas using electronically-controlled 3-port ALD diaphragm valves (Swagelok) that are maintained at higher temperatures to avoid precursor condensation within

the valves. For ALD precursors with low vapour pressure, the precursor ampoules are provided with external heating.

The substrate stage could be electrically heated from room-temperature (RT) up to 500 °C following a substrate temperature calibration factor. The deposition system is also provided with remote inductively coupled plasma (ICP) source located immediately above the substrate. This remote-ICP source consists of hollow Cu electrode wound around the quartz tube and powered by radio frequency (RF) power source in combination with a matching network. The reactant gas is introduced into the reactor through the quartz tube. During the plasma pulse the confined ICP glow within the quartz tube ionizes the reactant gas molecules into active plasma species for PEALD surface reaction.

The temperatures for precursor ampoule, ALD valve, delivery lines, reactor walls and the substrate are precisely controlled with an electronic PID temperature controller. The reactor chamber is provided with 2 optical ports/windows that are maintained clean by continuous inert gas purging. These optical ports are beneficial for real-time *in-situ* process characterization using techniques such as spectroscopic ellipsometry (SE) and optical emission spectroscopy (OES) as described later in this chapter.

3.3. Experimental Procedures

PEALD zirconium nitride (ZrN) films were grown using tetrakis-dimethylamido zirconium (TDMAZr) precursor (Sigma Aldrich) and forming gas (5% H_2: 95% N_2 from Praxair) reactant plasma on p-type Si (111) with

native SiO_2 layer and thermal SiO_2 substrates. The steps for the substrate preparation and film deposition are described in following subsections.

3.3.1. Substrate Preparation

Si (111) and thermal SiO_2 substrates were diced from 4-inch diameter wafers using precision silicon dicing saw (Disco DAD 321) with a cut width of ~50 μm. The diced substrates were cleaned in Piranha solution (a mixture of concentrated H_2SO_4 and H_2O_2 3:1 by volume) for 15 minutes to remove any trace organic contamination from the substrates, and securely stored in air-tight containers and used for deposition without further HF treatment.

3.3.2. Substrate transfer IN/OUT of reactor

A load-lock (LL) system is used to transfer substrates in and out of the ALD reactor without directly exposing the reactor to the ambient. After loading the substrate holder into the LL, it is pumped from atmospheric pressure down to 0.15 torr using a dry roughing pump (Edwards Inc.) and further down to high vacuum (<10^{-5} torr) using a turbomolecular pump backed with dry roughing pump. Before transferring substrate from LL under high vacuum into the ALD reactor (~ 0.4 Torr), the pressure difference is neutralized by purging LL with high purity N_2 gas. At pressure equilibrium, the transfer-gate valve between LL and the reactor is opened and the robotic arm extends to transfer substrate holder into the reactor. When inside the reactor the substrate holder is raised from the robotic arm using PIN-LIFT-UP function and the arm retracts back into the LL. The substrate holder is then placed on the substrate-stage in the

reactor with PIN-LIFT-DOWN function followed by the closing of transfer-gate valve and pumping LL back to high vacuum.

3.3.3. PEALD of ZrN

After transferring substrate holder into the ALD reactor, the inert gas flow (IGF) within the reactor is set to facilitate delivery of TDMAZr and forming gas to the substrate with the total pressure of ~1 Torr. The substrate temperature, plasma power and plasma gas composition is set to desired values followed by defining the pulsing sequence for the deposition cycle.

Before beginning PEALD, the substrate surface was conditioned with 30 s exposure of reactant gas plasma to facilitate desorption of loosely bound surface contaminant and condition the substrate for deposition. ZrN PEALD films were grown for a set number of deposition cycles and after deposition the substrate holder is transferred from ALD chamber back into LL following similar steps as described in **Section 3.3.2**. The substrate is allowed to cool down for ~15-20 minutes; before venting the LL to atmospheric pressure for substrate removal.

3.4. Characterization Techniques

The ALD growth and material properties for the ZrN PEALD films were characterized with thin film characterization techniques listed in **Table 3-1**. Optimum process parameters for self-limiting ALD growth were identified from the *iSE* data. X-ray reflectivity (*XRR*) was used as an alternative technique to compliment *SE* data analysis. The chemical bonding within the

deposited films and the electronic structure near Fermi energy (E_F) was studied from binding energy (BE) and valence band (VB) features of x-ray photoelectron spectroscopy (*XPS*). Electrical resistivity of ZrN films deposited on SiO_2 substrates was determined from the Van der Pauw sheet resistance measurement. Optical emission spectroscopy (*OES*) technique was used to study the active plasma species in ICP glow.

Table 3-1: Characterization techniques used to evaluate ALD films

Technique	**Properties of ALD films**			
	Optical	**Structural**	**Chemical**	**Electronic**
i-SE	$N = n - i \cdot k$	Thickness (*d*), Interfacial roughness	-	$\varepsilon = \varepsilon_1 - i \cdot \varepsilon_2$
XRR	-	Thickness (*d*), Interfacial roughness, Electron density (ρ^{el})	unit cell scattering factor (*f*)	-
XPS	-	-	Chemical bonding, atomic concentrations	*DOS* at E_{Fermi}
Van der Pauw	-	-	-	Sheet resistance (R_s)
OES	-	-	ICP plasma species	-

3.4.1. *In-situ* spectroscopic ellipsometry (*iSE*)

Spectroscopic ellipsometry (SE), introduced by Drude [1–3], is a powerful surface sensitive optical technique widely applied in thin film characterization to simultaneously determine its thickness and dielectric function [4–7]. In SE a well-defined polarized light is incident on the sample surface and the polarization of light upon specular reflection is determined for sample characterization. Since only the reflected light from the sample surface is

analyzed, the SE technique is well suited for *in-situ* characterization. With the advent of automated systems enabling fast acquisition of high-precision data [8–10], *in-situ* SE (iSE) is being increasingly adapted as a real-time diagnostic technique in moderate vacuum processes such as CVD, RIE, ALD, etc., [11–18].

Ellipsometry measurements consist of the determination of a parameter ρ, which is a ratio of complex reflection coefficients, $\mathcal{R}$ $\mathcal{R}$ in terms of the amplitude *A* and phase angle *δ* for the *p*- and *s*- polarized incident light given by:

$$\rho = \frac{R^p}{R^s} = \frac{A_{re}^p \exp\left(i\delta_{re}^p\right)}{A_{in}^p \exp\left(i\delta_{in}^p\right)} \Bigg/ \frac{A_{re}^s \exp\left(i\delta_{re}^s\right)}{A_{in}^s \exp\left(i\delta_{in}^s\right)} \tag{3.1}$$

For a linearly polarized incident light with equal *p*- and *s*- components (i.e. 45° polarization), $A_{in}^p = A_{in}^s$,$\delta_{in}^p = \delta_{in}^s$ where **Eq. (3.1)** simplifies to:

$$\rho = \frac{A_{re}^p}{A_{re}^s} \exp\left(i\left(\delta_{re}^p - \delta_{re}^s\right)\right) \tag{3.2}$$

The SE parameter ρ is often represented as $\rho = \tan\psi\, e^{i\Delta}$, where $\tan\psi = \left(A_{re}^p / A_{re}^s\right)$ is the amplitude ratio and $\Delta = \delta_{re}^p - \delta_{re}^s$ is the phase difference. For a multilayered film structure, ρ is a function of thickness (*d*) and dielectric constant $\varepsilon = \varepsilon_1 - i \cdot \varepsilon_2$ (or refractive index $N = n - i \cdot k$ with $\varepsilon = N^2$) of every layer. The complex reflection coefficient $R^{p,s}$ from a multilayered structure of *n* layers labeled as *0*, *1*, *2*, *3*... (*n-1)*, *n* where *0* is the vacuum and *n* is the substrate, is given by:

$$R_{0123\ldots n}^{p,s} = \frac{r_{0,1}^{p,s} + R_{123\ldots n}^{p,s}\, e^{-i\varphi_1}}{1 + r_{0,1}^{p,s}\, R_{123\ldots n}^{p,s}\, e^{-i\varphi_1}} \qquad \textbf{(3.3)}$$

The $r_{i,i+1}^{p}$ and $r_{i,i+1}^{s}$ are the reflection coefficients for p- and s- polarized light at the interface between the ith and $(i+1)^{th}$ layer, given by Fresnel's equations:

$$r_{i,i+1}^{p} = \frac{N_{i+1}\cos(\theta_i) - N_i\cos(\theta_{i+1})}{N_{i+1}\cos(\theta_i) + N_i\cos(\theta_{i+1})} \qquad \textbf{(3.4)}$$

$$r_{i,i+1}^{s} = \frac{N_i\cos(\theta_i) - N_{i+1}\cos(\theta_{i+1})}{N_i\cos(\theta_i) + N_{i+1}\cos(\theta_{i+1})} \qquad \textbf{(3.5)}$$

$\varphi_i = 4\pi d_i N_i \cos(\theta_i)/\lambda$, is the phase difference introduced from light propagation through the ith layer of thickness d_i ; N_i is the complex refractive index of the ith layer; θ_i is the incidence angle as light propagates from the ith to the $(i+1)^{th}$ layer following Snell's law, $N_0\sin(\theta_0) = N_i\sin(\theta_i)$. Interfacial features such as surface roughness or diffused interfaces within multilayered structures are included as additional layers with equivalent thickness and effective dielectric constant.

For a multi-layered structure with known thicknesses and dielectric constants for every layer, the theoretical SE parameters (Ψ, Δ) can be calculated from **Eq. (3.3)** – **Eq. (3.5)**. However the thickness and/or dielectric function of a thin film layer cannot be obtained from the measured $(\Psi, \Delta)^{\exp}$ data by analytical inversion, but requires numerical methods [5,19,20] or model based analysis [21,22].

In the model based approach, the unknown dielectric function $\tilde{\varepsilon}$ is expressed in a parameterized form with a reduced number of unknowns, with physical dispersion models like the Drude free electron dispersion, Lorentz oscillators, Harmonic oscillators, etc., or empirical dispersion models such as Cauchy, Sellmeier, etc. With an initial estimate of film thickness and dispersion parameters, the calculated/modeled SE data $(\Psi, \Delta)^{mod}$ is compared with the experimental data $(\Psi, \Delta)^{exp}$ using an error-function [23]. The thickness and dielectric function parameters within the modeled data are treated as fitting variables and are determined from non-linear regression routines [24] aimed towards minimizing this error-function, giving best-fit between $(\Psi, \Delta)^{mod}$ and $(\Psi, \Delta)^{exp}$.

The real-time or dynamic *iSE* (d-iSE) measurements on ALD grown films were taken in a polarizer – rotating compensator – sample – analyzer (PC_RSA) configuration of M2000DI spectroscopic ellipsometer (J. A. Woollam), over the spectral range of 0.73-6.40 eV (712 wavelengths). The hardware configuration of M2000-DI is schematically shown in **Figure 3-2**, where the polarized light is incident at a fixed angle of ~70° from the substrate normal. The acquisition time for *d-iSE* measurements was selected to obtain high signal-to-noise ratio by averaging multiple measurements (~50-100 at rate of ~50 milliseconds per measurements). Also to minimize errors induced by minor misalignment or imperfections within the instrument, a two-zone measurement scheme was employed where the each *d-iSE* dataset is obtained from the two measurements made at +45° and -45° analyzer position [22].

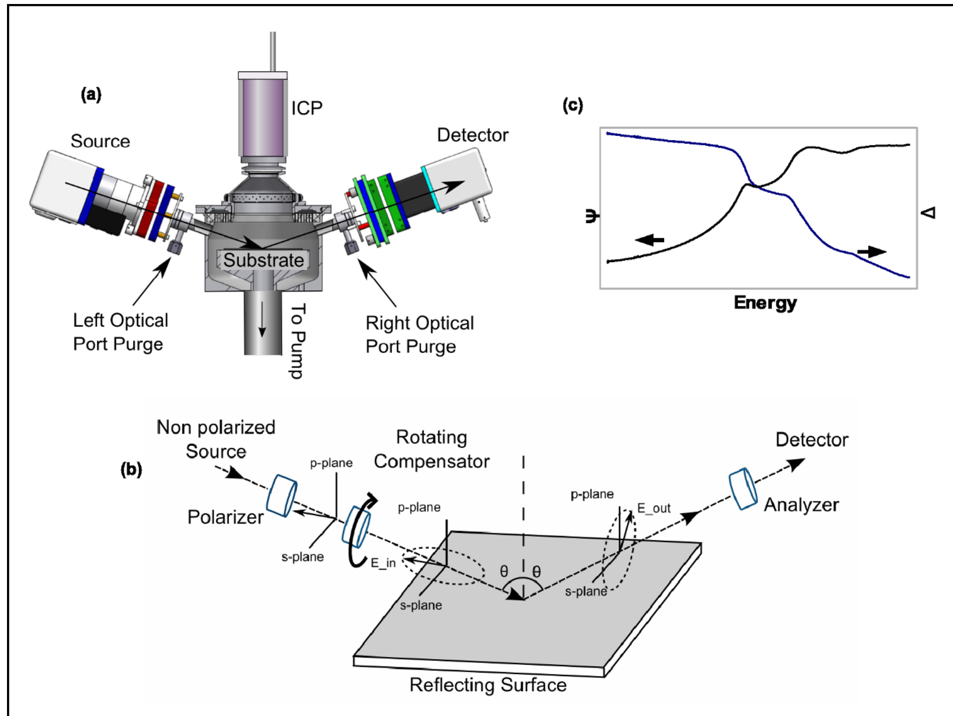

Figure 3-2: In-situ SE for real-time ALD growth studies: (a) Schematics of SE configuration on ALD 150LX reactor (adapted from operation manual, K. J. Lesker); (b) Principle of SE measurement (c) example of SE parameters (Ψ, Δ) measured on native-SiO_2/Si surface.

The model based analysis of measured *d-iSE* data was performed with CompleteEASE software package (ver. 4.48, J. A. Woollam).

3.4.2. X-ray reflectivity (XRR)

In principle x-ray reflectivity (XRR) is similar to the ellipsometry technique, since the measured reflected x-ray intensity from multilayered structure follows **Eq. (3.3)**, except that the incident x-rays are non-polarized and their refractive index is expressed as $n = 1 - \delta - i\beta$ with $\delta = \frac{\lambda^2}{2\pi} r_e \rho_e$ and $\beta = \frac{\lambda}{4\pi}\mu_x$, where r_e is the electron radius, ρ_e is the average electron density and μ_x is the x-ray absorption length [25,26]. *XRR* data analysis also uses a model based

approach treating the layer thickness and electron density as fitting parameters.

XRR measurements on ZrN PEALD films were performed using a Rigaku Ultima-IV multipurpose x-ray diffraction system, with a multilayer mirror for the incident monochromator [27]. Thickness and density of the ALD films were determined from analysis of the measured data using a GenX software package [28].

3.4.3. X-ray photoelectron spectroscopy (XPS)

In x-ray photoelectron spectroscopy the sample surface is exposed to a monochromatic x-ray beam and the intensity of the ejected photoelectrons (from ~ 10 nm sample depth limited by the photoelectron escape depth) is detected as a function of their kinetic energy (KE) with an electron energy analyzer. The binding energy (BE) of these photoelectrons is determined by $BE = h\nu - (KE + \phi)$, where $h\nu$ is the energy of the incident x-ray photon and ϕ is the detector work function. The BE for XPS features are a characteristic of specific electron transitions of a specific element and hence can identify the elements present in the sample. The surface atomic concentration is proportional to the integrated intensity of *XPS* features scaled by its Scofield's relative sensitivity factor (R.S.F.). Depending upon the local chemical environment, bonding and electronic state, the XPS spectrum is observed to undergo a chemical-shift in BE. The near Fermi level (E_F or at BE=0) features of XPS spectra, represents the valence band (VB) electronic density-of-states (DOS).

XPS measurements were performed using an Axis Ultra Spectrometer (Kratos Analytical) primarily to study chemical bonding and level of contamination within ZrN PEALD films. VB XPS spectra were also measured to determine the electronic DOS at the Fermi level.

3.4.4. Van der Pauw sheet resistance

The sheet resistance (R_S) of ZrN PEALD films deposited on thermal SiO_2 substrates was determined from Van der Pauw measurements using a Keithley 2400 source meter as a current source and a Tektronix DMM4050 digital multimeter as a voltammeter as shown schematically shown in **Figure 3-3**.

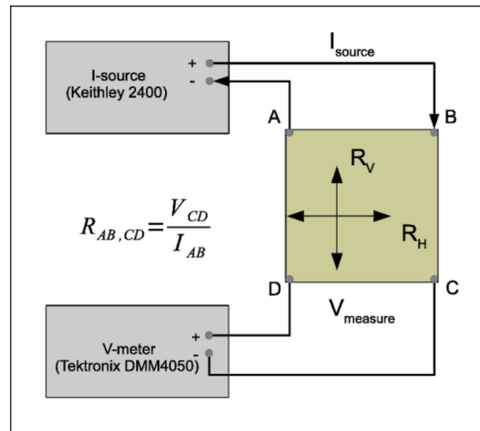

Figure 3-3: Sheet resistance (R_s) from Van der Pauw configuration.

With the soldered indium alloy contacts, the horizontal (R_H) and vertical (R_V) resistance was determined from the slope of measured voltages at different source-current values. To account for any systematic errors, measurements were made in reciprocal configuration and with reversed polarities:

$$R_H = \left(R_{AB,CD} + R_{BA,DC} + R_{CD,AB} + R_{DC,BA}\right)/4$$

$$R_V = \left(R_{BC,DA} + R_{CB,AD} + R_{DA,BC} + R_{AD,CB}\right)/4$$

The sheet resistance (R_S) was calculated using relation, $e^{-\pi R_H/R_S}+e^{-\pi R_V/R_S}=1$ and the electrical resistivity was obtained from the product of R_S and film thickness.

3.4.5. Optical emission spectroscopy (OES)

Optical emission from the PEALD plasma, as shown in **Figure 3-4**, was studied to identify active plasma species. The optical emission was collected through an optical port on ALD reactor using a collimating lens and analyzed using USB2000 Spectrometer (Ocean Optics) with spectral range of 200-850 nm with resolution of 0.4 nm. The plasma emission features were identified by comparison with NIST Atomic Spectral Database [29] and other literature sources [30–35].

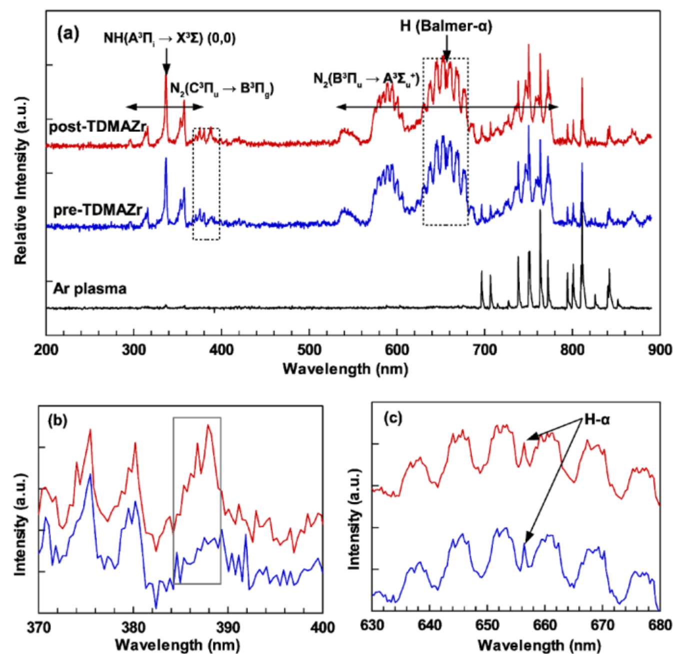

Figure 3-4: (a) Optical emission from 600 Watt (60 sccm forming gas + 100 sccm Argon) reactant plasma before and after TDMAZr pulse. Ar plasma is also shown for reference. (b) Additional features in 384.23-389.33 nm range corresponding to CN emissions were observed in the post-TDMAZr plasma pulse. (c) H-α emission at 656.5 nm shows the presence of atomic H in reactant plasma. For clarity the emission features are shifted along intensity axis.

3.5. References

[1] P. Drude, Ann Phys Chem N. F. 36 (1889) 532.

[2] P. Drude, Ann Phys Chem N. F. 36 (1889) 865.

[3] P. Drude, Ann Phys Chem N. F. 39 (1890) 481.

[4] D.E. Aspnes, J. Electrochem. Soc. 127 (1980) 1359.

[5] H. Arwin, D.E. Aspnes, Thin Solid Films 113 (1984) 101.

[6] K. Vedam, R. Rai, F. Lukes, R. Srinivasan, J. Opt. Soc. Am. 58 (1968) 526.

[7] R.J. Archer, J. Opt. Soc. Am. 52 (1962) 970.

[8] R.W. Collins, Rev. Sci. Instrum. 61 (1990) 2029.

[9] Y.-T. Kim, R.W. Collins, K. Vedam, Surf. Sci. 233 (1990) 341.

[10] I. An, Y.M. Li, H.V. Nguyen, R.W. Collins, Rev. Sci. Instrum. 63 (1992) 3842.

[11] J.B. Theeten, Surf. Sci. 96 (1980) 275.

[12] H. Seitz, B. Schröder, Solid State Commun. 116 (2000) 625.

[13] D.J. Thomas, J. Vac. Sci. Technol. B Microelectron. Nanometer Struct. 7 (1989) 1325.

[14] R. Müller, Appl. Phys. Lett. 57 (1990) 1020.

[15] D.E. Aspnes, W.E. Quinn, M.C. Tamargo, M.A.A. Pudensi, S.A. Schwarz, M.J.S.P. Brasil, R.E. Nahory, S. Gregory, Appl. Phys. Lett. 60 (1992) 1244.

[16] B. Johs, D. Doerr, S. Pittal, I.B. Bhat, S. Dakshinamurthy, Thin Solid Films 233 (1993) 293.

[17] S.D. Murthy, I. Bhat, B. Johs, S. Pittal, P. He, J. Electron. Mater. 24 (1995) 1087.

[18] E. Langereis, S.B.S. Heil, H.C.M. Knoops, W. Keuning, M.C.M. van de Sanden, W.M.M. Kessels, J. Phys. Appl. Phys. 42 (2009) 073001.

[19] D. Barton, F.K. Urban, Thin Solid Films 516 (2007) 119.

[20] M. Gilliot, Thin Solid Films 520 (2012) 5568.

[21] H.G. Tompkins, E.A. Irene, Handbook of Ellipsometry, William Andrew, 2005.

[22] H. Fujiwara, Spectroscopic Ellipsometry: Principles and Applications, Wiley, West Sussex, UK, 2007.

[23] C.M. Herzinger, B. Johs, W.A. McGahan, J.A. Woollam, W. Paulson, J. Appl. Phys. 83 (1998) 3323.

[24] J.J. Moré, in:, G.A. Watson (Ed.), Numer. Anal., Springer Berlin Heidelberg, 1978, pp. 105–116.

[25] J. Daillant, A. Gibaud, eds., X-Ray and Neutron Reflectivity: Principles and Applications, Springer, New York, 1999.

[26] J. Tiilikainen, J.-M. Tilli, V. Bosund, M. Mattila, T. Hakkarainen, J. Sormunen, H. Lipsanen, J. Phys. Appl. Phys. 40 (2007) 7497.

[27] M. Yasaka, Rigaku J. 26 (2010) 1.

[28] M. Björck, G. Andersson, J. Appl. Crystallogr. 40 (2007) 1174.

[29] A.E. Kramida, Y. Ralchenko, J. Reader, N.A.S.D. (2013) Team, NIST Atomic Spectra Database (version 5.1), National Institute of Standards and Technology, Gaithersburg, MD, 2008.

[30] Y.-K. Lee, C.-W. Chung, J. Appl. Phys. 109 (2011) 013306.

[31] S.J. Kang, V.M. Donnelly, Plasma Sources Sci. Technol. 16 (2007) 265.

[32] P. Jamroz, W. Zyrnicki, Surf. Coat. Technol. 201 (2006) 1444.

[33] J.J. Camacho, L. Díaz, M. Santos, D. Reyman, J.M.L. Poyato, J. Phys. Appl. Phys. 41 (2008) 105201.

[34] A. Fierro, G. Laity, A. Neuber, J. Phys. Appl. Phys. 45 (2012) 495202.

[35] S.S. Harilal, R.C. Issac, C.V. Bindhu, P. Gopinath, V.P.N. Nampoori, C.P.G. Vallabhan, Spectrochim. Acta. A. Mol. Biomol. Spectrosc. 53 (1997) 1527.

4. Dynamic *in-situ* SE study of ALD growth initiation[*]

4.1. Introduction

ALD has been conventionally applied in microelectronic fabrication for deposition of compound thin films [1–3]. Recently, atomic scale control in ALD is being increasingly utilized in the fabrication of low-dimensional structures and nanodevices [4,5]. Numerous ALD studies, as reviewed in [6–11], have shown that GPC (nm/cycle) for ALD film is often less than the monolayer thickness. Substrate dependent non-linear growth has also been observed in the early stages of ALD growth [12]. Real-time in-situ techniques such as *QCM*, *QMS*, *d-iSE*, *OES*, etc., have been found to be extremely useful to study ALD growth process [13–18].

This chapter covers application of the *d-iSE* technique to the study of the early stages of ZrN PEALD growth. The raw ellipsometry data is interpreted as a combined effect of partial surface monolayer film growth and changing surface chemistry during the ALD cycle. Bruggeman's effective medium approximation (B-EMA) is applied to construct an optical model representing a partially covered ALD surface monolayer. The measured *d-iSE* data in the

---

[*] A version of this chapter has been submitted to the Journal of Applied Surface Science for publication

early stages of ZrN growth is analyzed on the basis of diffusive ALD film growth [19], where the precursor molecules can undergo surface diffusion to reach the most thermodynamically favourable reaction sites.

4.2. ZrN growth and *d-iSE* acquisition

ZrN PEALD films were deposited on p-type Si (111) substrates in an ALD 150LX reactor with tetrakis-dimethylamido-zirconium (TDMAZr) and forming gas (H_2:N_2) plasma using cycle 0.12s TDMAZr/ 15s Ar/15s plasma (600 W)/15s Ar purge at substrate temperature of 150 °C. The substrate temperature for ZrN deposition was within the ALD temperature window as will be shown in Chapter 5. The Zr precursor pulse and plasma exposures were kept slightly higher than required for self-limiting growth to ensure that the ALD surface reactions attain saturation. Inert gas purges separating precursor and plasma exposure steps were kept sufficiently long to allow complete removal of reaction by-products and also to permit multiple *d-iSE* measurements.

Since the surface chemistry changes continuously during precursor and plasma ALD reaction at the substrate, it was essential to use short acquisition times for *d-iSE* measurements. The *d-iSE* data reported here was average from multiple SE measurements collected over acquisition time of 1.5 s (total of ~3.0 s with two-zone measurement) to reduce signal noise in the acquired data.

4.3. ALD growth modes

Although the term ALD suggests a complete monolayer deposition per cycle, experimental results have shown that even for otherwise “near-ideal” $AlMe_3/H_2O$ process, the steric hindrance from precursor molecules restricts deposition to a partial monolayer over an individual deposition cycle [7].

Depending upon the availability, distribution and selectivity of the surface reaction sites, the modes of ALD growth could be classified into (1) layer-by-layer (Frank-van der Merwe growth) (2) random deposition (RD) and (3) island growth (Volmer-Weber growth) [12,20–23]. For evenly distributed reaction sites, repulsive interaction between precursor molecules (steric factors) results in a uniform precursor adsorption over substrate surface. A preferential adsorbate-substrate interaction favors a layer-by-layer growth, while random deposition occurs when the adsorbate-adsorbate interaction is equally probable as the adsorbate-substrate interaction. In case of non-uniform or a localized distribution of reaction sites, an island-growth is observed [22].

The random deposition mode of ALD growth assumes negligible surface mobility of surface adsorbed species such that they readily react at the surface without diffusing into neighboring energetically more favorable sites [21]. However in a realistic case, the adsorbed species are sufficiently mobile to undergo surface diffusion. In presence of ample reaction sites, such surface diffusion enhanced mode of ALD growth would be an intermediate between an ideal layer-by-layer and random deposition. A theoretical description of such a diffusive mode of film growth has been reported in [19].

4.4. Bruggeman's EMA to model sub monolayer ALD growth

The earliest work on the application of ellipsometry to sub-monolayer adsorption studies of molecular gases on clean substrates can be found in [24–28] that demonstrates coverage (θ) dependence of the measured ellipsometry parameters (Ψ, Δ). The analysis of the (Ψ, Δ), as presented in [28], treats the surface monolayer with coverage θ as a composite system consisting of the adsorbed species and voids with volume fractions θ and (1- θ) respectively, with its dielectric function given by an effective medium approximation as described in [29–31]. It was shown that with EMA representation, coverage of the partial surface monolayer could be reliably extracted from analysis of measured SE data. Based on these studies, the dielectric function of partial ALD surface monolayer was represented with Bruggeman's EMA (B-EMA) layer as schematically shown in **Figure 4-1**.

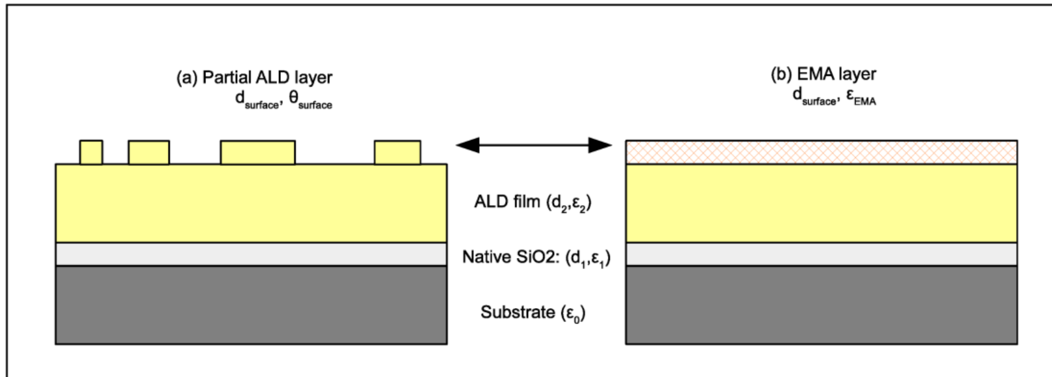

Figure 4-1: Partial ALD surface layer with coverage θ and thickness $d_{surface}$ in (a) is represented with B-EMA layer of effective dielectric function ε_{EMA} and thickness $d_{surface}$ in (b).

In the B-EMA equation **Eq. (4.1)**, ε_{ALD} and ε_{void} are the dielectric constants for the ALD film and the voids with volume fractions θ and (1- θ), respectively, while the effective dielectric constants for the partial ALD layer is ε_{θ}. The

screening parameter L ($0 \le L \le 1$) depends upon the geometrical shape and configuration of ALD clusters in the partial surface layer. Surface coverage of the ALD partial layer is determined by treating θ as an additional fitting parameter in SE data analysis.

$$\theta \frac{\varepsilon_{ALD} - \varepsilon_{\theta}}{L\varepsilon_{ALD} + (1-L)\varepsilon_{\theta}} + (1-\theta)\frac{\varepsilon_{void} - \varepsilon_{\theta}}{L\varepsilon_{void} + (1-L)\varepsilon_{\theta}} = 0 \qquad \textbf{(4.1)}$$

Other theories describing θ dependent optical constants can be found in [32–34]. An alternate approach considering coherent superposition of reflected light from a partial monolayer can be found in [35,36].

4.5. Results and discussion

4.5.1. Interpretation of measured *d-iSE* data

The *d-iSE* parameters (Ψ, Δ) in the early stages of ZrN PEALD growth are shown in **Figure 4-2** along with the precursor pulse and plasma exposure sequence. Although *d-iSE* parameters were measured over entire spectral range of the M2000DI (712 data points in range of 0.73 – 6.4 eV), the parameters measured at 4.0 eV are only shown for clarity. Variation in the measured (*Ψ, Δ*) follows the changing surface chemistry at the growing film interface with every precursor and plasma ALD half-reactions. Since Δ is known to be more sensitive to the surface conditions than Ψ [37], variation in Δ (δΔ) are more noticeable than in Ψ (δΨ).

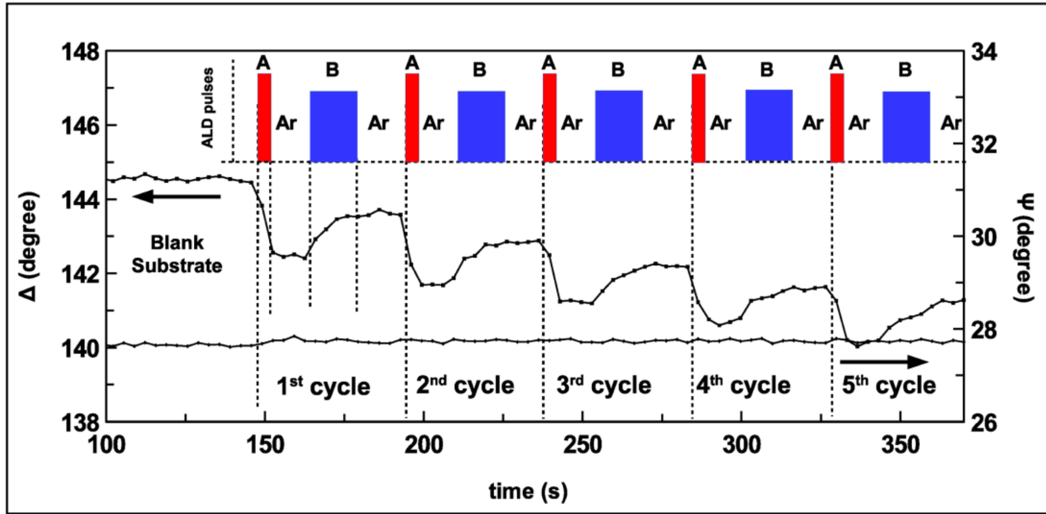

Figure 4-2: The d-iSE parameters (Δ, Ψ) at 4.0 eV measured in the early stages of ZrN PEALD growth. ALD pulse A dna B denotes the TDMAZr pulse and forming gas plasma exposure respectively.

At the end of nth ZrN PEALD cycle in an optimized process, the substrate surface is composed of partial ZrN layer, $\theta^{ZrN} + \theta^{void}$. In the following precursor pulse A, surface adsorption/reaction of TDMAZr molecules changes this surface composition to $\theta^{ZrN} + (\theta - \delta\theta)^{void} + \delta\theta^{TDMAZr}$, resulting in a decrease in Δ ($\delta\Delta < 0$). With the onset of plasma exposures B, the active plasma species reacts with the surface TDMAZr molecules changing the surface composition to $(\theta + \delta\theta)^{ZrN} + (\theta - \delta\theta)^{void}$, along with an increase in Δ ($\delta\Delta > 0$). During Ar purge the surface composition does not undergo any change, and hence, in the absence of precursor or plasma pulses a steady state value is observed in the measured Δ. Since SE measurements are sensitive to both surface chemistry as well as incremental ALD growth $\delta\theta^{ZrN}$, only the steady state parameters (Ψ, Δ) measured after plasma exposures should be analyzed to evaluate ALD film growth unlike the analysis presented in [38].

4.5.2. ZrN PEALD film properties

Thin film dielectric constants differ significantly from their bulk values because of the finite size effects [39–41], hence the dielectric function of ZrN PEALD films was determined from analysis of *iSE* parameters. As a first approximation, in this analysis the thicker ZrN PEALD film was assumed to be smooth with sharp interfaces. The ZrN film/substrate was modelled as a 3-layered stack as shown in **Figure 4-1(a)**, with its dielectric function expressed with Drude-Lorentz oscillators [42, 43] given by **Eq. (4.2)**:

$$\varepsilon = \varepsilon_{\infty} - \frac{E_p^2}{E^2 - i\Gamma_r E} + \sum_{n=1}^{2} \frac{S_n^2}{\left(E_n^2 - E^2\right) + i\Gamma_n E} \qquad \textbf{(4.2)}$$

E_p and Γ_r are the plasma energy and relaxation energy for the free electron absorption expressed by the Drude term. The bound charge contribution to the dielectric function is represented by the strength (S_n), broadening (Γ_n) and center energy (E_n) for nth Lorentz oscillator. The constant ε_{∞} is to account for optical excitations not included in **Eq. (4.2)**.

The thickness of the native SiO_2 layer was determined from the *iSE* measurements on bare Si substrates prior to ALD deposition. For a 60 cycle ZrN PEALD, the *iSE* data analysis revealed film thickness of 5.71±0.01 nm with the dielectric function consisting of two Lorentz oscillators centered at 4.93±0.10 eV and 6.88±0.10 eV, respectively, as shown in **Figure 4-3**.

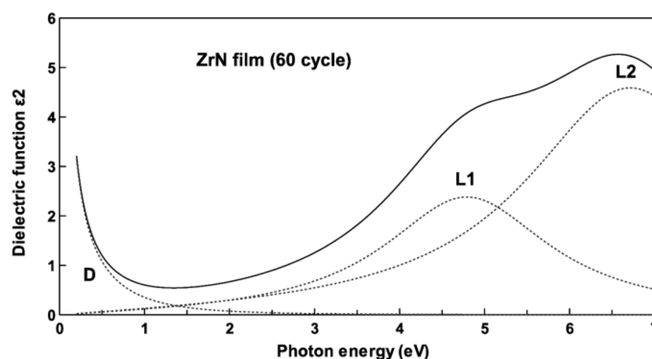

Figure 4-3: Imaginary part (ε_2) of the dielectric function for 5.71±0.01 nm thick ZrN PEALD film as determined from iSE data. The Drude (D) and Lorentz (L1 and L2) components are also shown.

Alternate optical models including roughness at the growing film surface, when applied to *iSE* data analysis, gave the optical roughness of ~ 0.02 nm without significant improvement in SE data fitting or variation in the film dielectric constant. This validates our first approximation where the surface of thicker ZrN PEALD film was assumed to be smooth.

XPS measurements (shown in Chapter 5) on thicker ZrN films, deposited under identical conditions, showed excess N (corresponding to stoichiometry $ZrN_{1.16}$) along with presence of O and C contamination.

4.5.3. Initial stages of ZrN PEALD growth

Skipping the HF last treatment on Si substrates ensures that there are ample reaction sites, surface –OH groups from the native SiO_2 layer, available for ZrN PEALD growth initiation. These evenly distributed surface –OH groups and steric hindrance from the TDMAZr molecules would result in a uniform adsorption of precursor molecules in the first precursor half-reaction of ALD. Also with the sufficient surface mobility of adsorbed TDMAZr molecules

(melting point ~ 75 °C) at substrate temperature of 150 °C, the PEALD growth is inclined towards the diffusive mode of film growth, an intermediate mode between ideal layer–by–layer and random deposition, as discussed earlier in Section 4.3.

For the surface diffusion enhanced growth during the early stages of ZrN PEALD, the optical model as shown in **Figure 4-1(a)** in the analysis of *d-iSE* data could be greatly simplified in terms of ZrN surface monolayer thickness (d^m). In this diffusive growth regime, the ALD film is modelled as (i) partial surface layer with coverage θ and thickness d^m and (ii) underlying ALD film with thickness equal to $n \cdot d^m$, where n is the number of complete ALD monolayers. The adsorbed precursor molecules would mimic and translate the atomic arrangement of substrate surface over growth of first few monolayers. Hence the d^m of 0.27 nm was obtained from interplanar spacing between ZrN (111) planes for the first monolayer deposition on Si (111). An alternate approach to define ALD monolayer thickness has been proposed in [20,21].

The *d-iSE* parameter Δ measured at 4.0 eV during ZrN PEALD, shown in **Figure 4-4(a)**, suggests that TDMAZr molecules are readily adsorbed on bare Si (111) substrates from the very first deposition cycle. This non-inhibited ALD growth initiation is attributed to the ample reactive sites (surface –OH groups) on the surface of the native SiO_2 layer. As shown in **Figure 4-1(b)**, the partial ZrN PEALD surface monolayer with thickness d^m = 0.27 nm and coverage θ is modeled as a B-EMA layer with the ZrN dielectric function as shown in **Figure 4-3** and L=0 in **Eq. (4.1)**. The fractional coverage of the

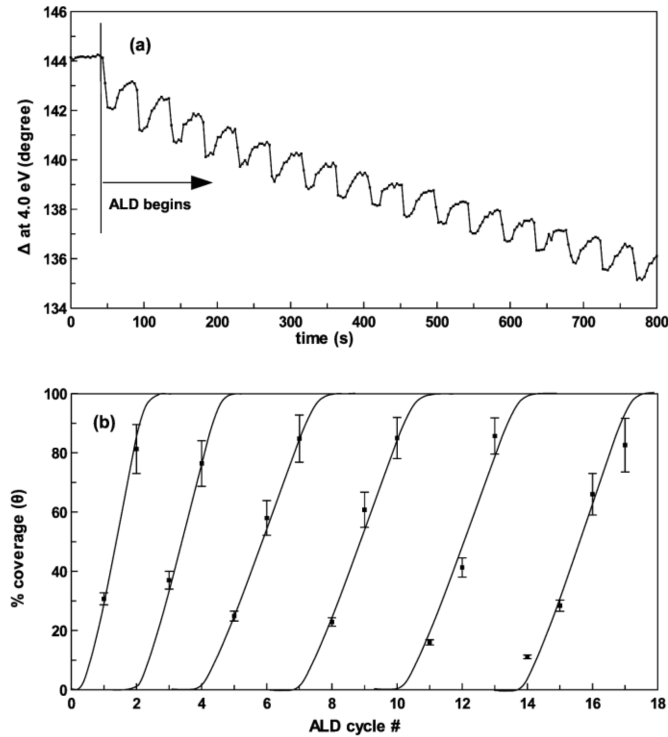

Figure 4-4: (a) *d-iSE* parameter Δ measured at 4.0 eV in the early stages of ZrN PEALD on Si(111) substrate; (b) determined ZrN surface monolayer coverage against deposition cycle for first 6 monolayer growth. This ALD film coverage is determined from the analysis of *d-iSE* data using B-EMA approximation in diffusive growth regime. Solid lines are guide to the eye.

ZrN PEALD surface monolayer is determined from *d-iSE* data analysis by treating it as a fitting parameter. The thickness of underlying ALD film (d_2), starting from zero thickness for first deposition cycle, is incremented in steps of d^m as the surface monolayer coverage approaches completion (θ→1). The calculated ZrN PEALD surface coverage is shown in **Figure 4-4(b)** demonstrates substrate-accelerated growth for first 2 monolayers, while steady state ALD growth is attained from the 3rd monolayer onwards. At the end of 18 deposition cycles, the thickness of the ZrN film was determined to be 1.58 nm, consistent with the growth of ~6 monolayers.

4.6. Summary

In conclusion, a physical interpretation of the *d-iSE* data measured during ZrN PEALD is presented here along with application of B-EMA in the analysis of *d-iSE* data to account for partial monolayer ALD growth. With availability of ample surface –OH reaction sites on the native SiO_2 layer of the Si substrate and sufficient mobility for TDMAZr molecules at 150 °C substrate temperature, the ZrN PEALD is expected to follow the surface diffusion enhanced mode of film growth. In this diffusive growth regime, the coverage of the ZrN PEALD surface monolayer is determined after every deposition cycle from *d-iSE* data. The calculated surface coverage for ZrN PEALD demonstrates substrate accelerated growth for the first 2 monolayer deposition followed by a steady state growth regime from 3rd monolayer onwards. The *d-iSE* data analysis of ZrN PEALD presented in this chapter can be applied to other ALD processes with the modifications to optical model to represent the appropriate mode of film growth.

4.7. References

[1] J. Antson, T. Suntola, Method for Producing Compound Thin Films, 4,058,430, 1977.

[2] T. Suntola, Mater. Sci. Rep. 4 (1989) 261.

[3] J. Robertson, Rep. Prog. Phys. 69 (2006) 327.

[4] S.M. George, Chem. Rev. 110 (2010) 111.

[5] H. Kim, H.-B.-R. Lee, W.-J. Maeng, Thin Solid Films 517 (2009) 2563.

[6] S.M. George, A.W. Ott, J.W. Klaus, J. Phys. Chem. 100 (1996) 13121.

[7] R.L. Puurunen, J. Appl. Phys. 97 (2005) 121301.

[8] V. Miikkulainen, M. Leskelä, M. Ritala, R.L. Puurunen, J. Appl. Phys. 113 (2013) 021301.

[9] S.M. George, Chem. Rev. 110 (2010) 111.

[10] H. Kim, Thin Solid Films 519 (2011) 6639.

[11] H.B. Profijt, S.E. Potts, M.C.M. van de Sanden, W.M.M. Kessels, J. Vac. Sci. Technol. Vac. Surf. Films 29 (2011) 050801.

[12] M.A. Alam, M.L. Green, J. Appl. Phys. 94 (2003) 3403.

[13] K. Knapas, M. Ritala, Crit. Rev. Solid State Mater. Sci. 38 (2013) 167.

[14] H. Tiznado, M. Bouman, B.-C. Kang, I. Lee, F. Zaera, J. Mol. Catal. Chem. 281 (2008) 35.

[15] C.L. Platt, N. Li, K. Li, T.M. Klein, Thin Solid Films 518 (2010) 4081.

[16] R. Methaapanon, S.M. Geyer, S. Brennan, S.F. Bent, Chem. Mater. 25 (2013) 3458.

[17] A. Yanguas-Gil, J.A. Libera, J.W. Elam, ECS Trans. 50 (2013) 43.

[18] E. Langereis, S.B.S. Heil, H.C.M. Knoops, W. Keuning, M.C.M. van de Sanden, W.M.M. Kessels, J. Phys. Appl. Phys. 42 (2009) 073001.

[19] P.I. Cohen, G.S. Petrich, P.R. Pukite, G.J. Whaley, A.S. Arrott, Surf. Sci. 216 (1989) 222.

[20] R.L. Puurunen, W. Vandervorst, W.F.A. Besling, O. Richard, H. Bender, T. Conard, C. Zhao, A. Delabie, M. Caymax, S. De Gendt, M. Heyns, M.M. Viitanen, M. de Ridder, H.H. Brongersma, Y. Tamminga, T. Dao, T. de Win, M. Verheijen, M. Kaiser, M. Tuominen, J. Appl. Phys. 96 (2004) 4878.

[21] R.L. Puurunen, Chem. Vap. Depos. 10 (2004) 159.

[22] R.L. Puurunen, W. Vandervorst, J. Appl. Phys. 96 (2004) 7686.

[23] A. Satta, A. Vantomme, J. Schuhmacher, C.M. Whelan, V. Sutcliffe, K. Maex, Appl. Phys. Lett. 84 (2004) 4571.

[24] R.J. Archer, G.W. Gobeli, J. Phys. Chem. Solids 26 (1965) 343.

[25] G.A. Bootsma, F. Meyer, Surf. Sci. 14 (1969) 52.

[26] F. Meyer, E.E. De Kluizenaar, G.A. Bootsma, Surf. Sci. 27 (1971) 88.

[27] F.H.P.M. Habraken, O.L.J. Gijzeman, G.A. Bootsma, Surf. Sci. 96 (1980) 482.

[28] L.J. Hanekamp, S.J.H. Brader, G.A. Bootsma, Surf. Sci. 135 (1983) 383.

[29] D. Aspnes, J. Theeten, F. Hottier, Phys. Rev. B 20 (1979) 3292.

[30] H. Fujiwara, J. Koh, P. Rovira, R. Collins, Phys. Rev. B 61 (2000) 10832.

[31] M. Scheller, C. Jansen, M. Koch, in:, K. Young (Ed.), Recent Opt. Photonic Technol., InTech, 2010.

[32] C. Strachan, Math. Proc. Camb. Philos. Soc. 29 (1933) 116.

[33] D.V. Sivukhin, Zhurnal Eksp. Teor. Fiz. 18 (1948) 976.

[34] M.J. Dignam, M. Moskovits, J. Chem. Soc. Faraday Trans. 2 69 (1973) 56.

[35] R.H. Muller, J.C. Farmer, Surf. Sci. 135 (1983) 521.

[36] J.C. Farmer, J. Electrochem. Soc. 132 (1985) 313.

[37] A.V. Tikhonravov, M.K. Trubetskov, E. Masetti, A.V. Krasilnikova, I.V. Kochikov, in:, C. Amra, H.A. Macleod (Eds.), Adv. Opt. Interf. Coat., 1999, pp. 173–182.

[38] H. Wang, X. Jiang, B.G. Willis, J. Vac. Sci. Technol. Vac. Surf. Films 30 (2012) 01A133.

[39] C.G. Ribbing, A. Roos, in:, Handb. Opt. Constants Solids, Elsevier, 1997, pp. 351–369.

[40] A. Lehmuskero, M. Kuittinen, P. Vahimaa, Opt. Express 15 (2007) 10744.

[41] S.A. Kovalenko, M. p. Lisitsa, Semicond. Phys. Quantum Electron. Optoelectron. 4 (2001) 352.

[42] M.A. Signore, D. Valerini, L. Tapfer, G. Caretto, A. Rizzo, J. Vac. Sci. Technol. Vac. Surf. Films 29 (2011) 061507.

[43] D. Valerini, M.A. Signore, A. Rizzo, L. Tapfer, J. Appl. Phys. 108 (2010) 083536.

5. Plasma ALD of conducting ZrN thin films*

5.1. Introduction

Transition metal nitrides such as TiN, TaN*, WN*, HfN*, ZrN*, etc., (* denotes variable stoichiometry) are interesting materials with potential applications in semiconductor device fabrication because of their low electrical resistivity, high melting point and high thermal stability [1–6]. Surface reactions for deposition of these metal nitride have been reviewed in [7,8].

This chapter describes process optimization ZrN PEALD using TDMAZr and forming gas (H_2:N_2) reactant plasma to attain self-limiting growth. An experimental design scheme based on ALD surface reactions at saturation is presented for ALD cycle optimization with reduced number of experiments. The observed ZrN growth characteristics with respect to substrate temperature and ALD cycle parameters (precursor/reactant dose and inert gas purge) and their material properties are compared to the reported data in the literature.

5.2. Experimental Procedure

ZrN plasma ALD films were deposited on piranha cleaned p-type Si (111) and thermal SiO_2 (>500 nm thickness on Si) substrates in a continuous flow ALD

---

* A version of this chapter will been submitted for publication

150LX reactor at total pressure of 1.04 torr. Details on the ALD reactor, substrate preparation and loading into the reactor have been described in Chapter 3. For *in-situ* ALD growth characterization, a spectroscopic ellipsometer M2000DI was mounted on the reactor as shown in **Figure 5-1**.

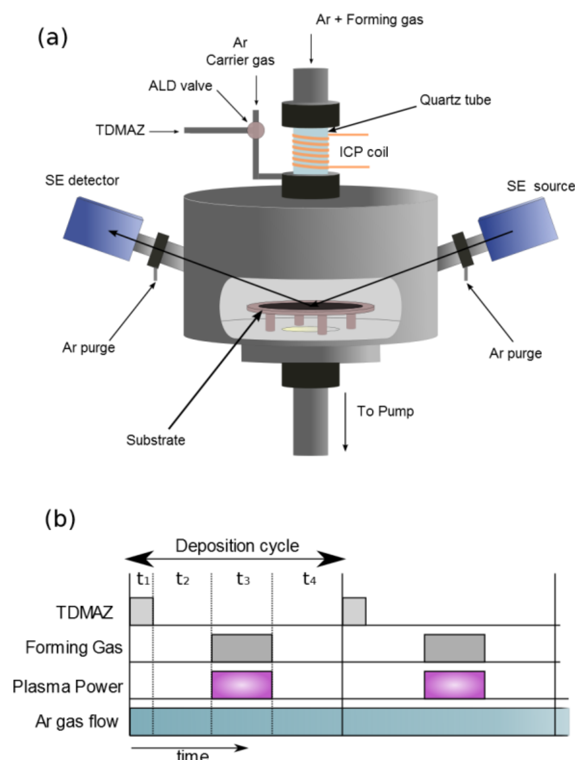

Figure 5-1: (a) Schematics of spectroscopic ellipsometer M2000DI on ALD150LX reactor chamber along with TDMAZr and forming gas inlets. (b) Deposition cycle for ZrN PEALD.

The deposition cycle for ZrN PEALD consisted of TDMAZr pulse (t_1) – Ar purge (t_2) – plasma pulse (t_3) – Ar purge (t_4), where t_i is the respective pulse/purge duration. A precise dose of TDMAZr molecules was introduced into the carrier gas (Ar at 40 sccm flow) from the ampoule (at 75 °C) using an electronically controlled 3-way ALD diaphragm valve (at 75 °C). During the plasma pulse, forming gas (60 sccm flow) was introduced into the reactor

under carrier gas (Ar 100 sccm flow) through a RF (13.56 MHz) inductively coupled plasma (ICP) glow confined within a quartz tube, generating active plasma species for ALD surface reaction. To prevent gas-phase reactions, the precursor and plasma pulses were separated by Ar purges (durations t_2 and t_3 respectively) allowing enough time to pump out any excess unreacted TDMAZr molecules and reaction by-products from the reactor.

The substrates were positioned in the chamber to enable real-time *d-iSE* measurements during deposition. Followed by transfer of substrate into the ALD reactor and before deposition, the substrates were treated with forming gas plasma to remove any loosely adsorbed surface molecules and condition substrate surface for TDMAZr adsorption. After plasma treatment, the thickness and the surface roughness of native SiO_2 layer of Si substrate was determined from *d-iSE* measurements prior to deposition. An average ALD growth-per-cycle (GPC) was obtained from the ZrN film thickness determined from the analysis of *d-iSE* data. For plasma gas composition (60 sccm forming gas, 100 sccm Ar) and constant 600 W plasma power, other ALD process parameters, i.e. temperature window, optimum precursor/reactant dose and inert gas purge, were determined to attain self-limiting growth conditions for ZrN PEALD.

The material properties of ZrN films deposited under self-limiting growth conditions were characterized and compared with literature data. The thickness and dielectric function of the deposited films was obtained from the analysis of *iSE* data measured at the end of deposition. The valence band (VB)

and binding energy (BE) spectra from XPS measurements were used to analyze electronic density-of-states (DOS) near the Fermi energy (E_F) and elements in the PEALD films. Glancing incidence x-ray diffraction (GIXRD) and x-ray reflectivity (XRR) measurements were performed using a Rigaku Ultima-IV diffractometer to investigate crystal microstructure and mass density of the deposited films. XRR thickness was also determined from a few samples to compare with the *iSE* film thickness. Electrical resistivity was determined from 4-wire sheet resistance measurements in Van der Pauw configuration using a Keithley 2400 sourcemeter for current source and Tektronix DMM4050 as a voltammeter.

5.3. Dynamic *iSE* on ZrN plasma ALD films

5.3.1. Acquisition and interpretation of *d-iSE* data

The *d-iSE* data on growing ZrN PEALD film was acquired over 3.0 s for each individual measurement in high-accuracy mode (2-zone measurement). Dynamic *iSE* parameter (Ψ, Δ) were measured over the entire measurement range of the M2000DI (712 wavelengths over 0.73 – 6.4 eV), as shown in **Figure 5-2** (lower inset). As Δ is more sensitive to surface conditions than Ψ [9], only *d-iSE* parameter Δ measured at single wavelength (4.0 eV) is shown here for clarity. The *d-iSE* data acquisition and its interpretation have been discussed in details in Chapter 4. Only the *d-iSE* measurements taken during post-plasma purge were analyzed using CompleteEASE software package (version 4.48, J. A. Woollam) to characterize ALD growth.

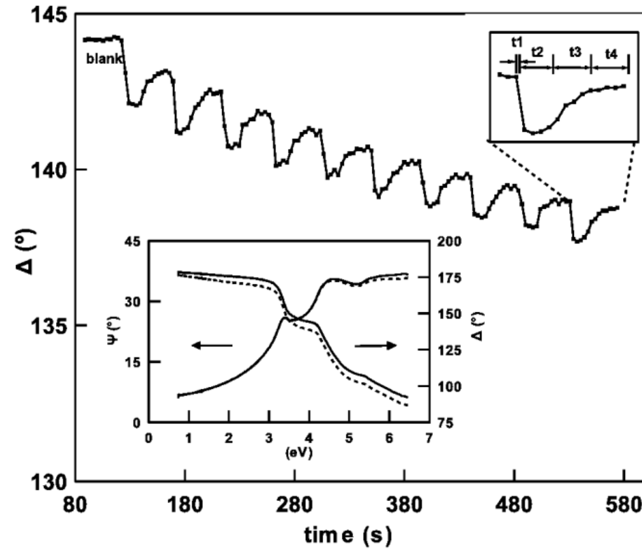

Figure 5-2: The d-iSE parameter Δ measured at 4.0 eV during first 10 cycles of ZrN PEALD. The duration of precursor pulse (t_1), plasma exposure (t_3) and inert gas purges (t_2 and t_4) are shown in upper inset. Lower inset shows iSE parameters (Ψ, Δ) measured on blank substrate (solid line) and after 10 deposition cycles (dotted lines) ever entire range of M2000DI.

5.3.2. Analysis of *d-iSE* data

ALD proceeds with incremental growth of partial surface monolayer per deposition cycle [10,11], and hence an optical model incorporating this sub-monolayer ALD growth must be used in the analysis of *d-iSE* data as shown in Chapter 4. However for optimization of deposition cycle, ALD surface monolayer is approximated as a smooth continuous film with coverage dependent effective thickness [12, 13]. For *d-iSE* data analysis with this approximation, the ALD film/substrate is modelled as a 3-layer stack consisting of continuous ALD film (ε_{film}, d_{film}), native SiO_2 (ε_{ox}, d_{ox}) and Si substrate (ε_{Si}). The thickness of native SiO_2 was determined from the *iSE* measured on bare substrates prior to deposition. Using a model based analysis [14, 15], the measured *d-iSE* parameters after every deposition cycle for ZrN growth were analyzed to characterize ALD process. The dielectric function of

ZrN PEALD films was modelled with a Drude and 2 Lorentz oscillators [16, 17] using **Eq. (5.1)**.

$$\varepsilon = \varepsilon_{\infty} - \frac{E_p^2}{E^2 - i\Gamma_r E} + \sum_{n=1}^{2} \frac{f_n E_n^2}{\left(E_n^2 - E^2\right) + iE\Gamma_n} \quad \textbf{(5.1)}$$

E_p and Γ_r are the plasma energy and relaxation energy for the free electron absorption expressed by the Drude term. The bound charge contribution to the dielectric function is represented with Lorentz oscillators characterized by their strength (f_n), broadening (Γ_n) and center energy (E_n). The constant ε_∞ is to account for optical excitations not included in **Eq. (5.1)**.

5.4. Results and discussion:

5.4.1. Growth-per-cycle (GPC) from *iSE* data

Due to finite-size effects in thin film properties [18–20], the dielectric function parameters were treated as fitting parameters along with ZrN PEALD film thickness for every analyzed *iSE* data set. When surface roughness was included in the optical model for the analysis of *iSE* data, it was found to be ~0.01 nm without significant improvement in the SE data fitting or change in the dielectric function parameters. Hence in the further *iSE* data analysis all the film interfaces are assumed to be smooth within continuous ALD film approximation.

Figure 5-3 shows the characteristic ZrN PEALD thickness as determined from the analysis of *iSE* data at end of every 5$^{\mathrm{th}}$ deposition cycle. Absence of growth initiation/nucleation delay for ZrN PEALD is attributed to the large density of surface –OH reaction sites on Si substrates.

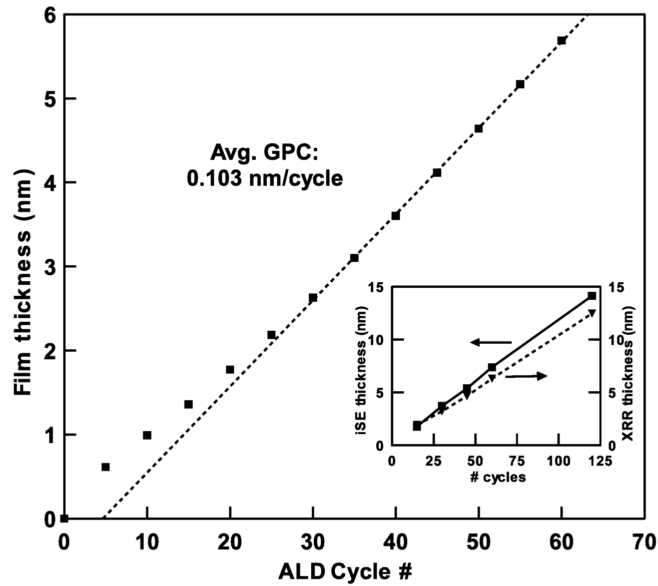

Figure 5-3: ZrN PEALD film thickness against number of deposition cycles as determined from analysis of *iSE* measurements. An average GPC of 0.103 nm per cycle was obtained in the linear growth regime (dotted line) for 0.12s TDMAZr/15s Ar purge/15s plasma/15s Ar purge, for 600 Watts plasma at 150 °C substrate temperature. (Inset) shows a comparison between the film thickness as derived from *iSE* measurements at 150 °C (solid lines) and ex-situ XRR measurements at RT (dotted lines).

In the early stages of deposition, ZrN growth results from heterogeneous surface reactions on native SiO_2 layer, that is, hetero-ALD. However in the later growth stages ALD reactions occurs on the underlying grown film, that is, a homo-ALD. A non-linearity in thickness vs. cycle number over first 25 ALD cycles is attributed to this transition from heterogeneous to homogeneous mode of surface reactions [21–23]. In the linear-growth regime, an average growth per cycle (GPC) was determined as 0.103 nm-per-cycle from the slope of the linear fit between film thicknesses against number of deposition cycles. ZrN film thickness as determined from analysis of *iSE* data was compared with *ex-situ* XRR measurements as shown in **Figure 5-3**(inset). Both the *in-situ* (at 150 °C) and *ex-situ* (at ~ 26 °C) shows a linear increase in film thickness with number of deposition cycles. The difference between the

iSE and XRR thicknesses are related to the measurement conditions and may be linked to the thermal expansion coefficient of ZrN ALD films.

5.4.2. ZrN plasma ALD process optimization

The deposition process parameters, namely the substrate temperature (T_{sub}), TDMAZr pulse (t_1), post-precursor purge (t_2) plasma exposure length (t_3) and post plasma purge (t_4), were experimentally obtained for characteristic ALD growth such that the total time length for the deposition cycle is minimized. The experimental design (see **Table 5-1**), was based on the fundamental ALD surface reactions that are assured to be self-limiting for sufficiently precursor/reactant doses and long inert gas purges. For every set of experiments only the target parameter (denoted with superscript *var*) was varied keeping other parameters constant such that the ZrN film growth is influenced only by the target parameter. With this experimental scheme, the interdependence between parameters affecting film growth could be eliminated, thereby reducing the number of depositions required for ALD cycle optimization.

Table 5-1: Design of experiments to determine optimized process parameters for ZrN PEALD growth. ALD cycle is represented as TDMAZr pulse (t_1) – post-precursor purge (t_2) – plasma pulse (t_3) – post plasma purge (t_4); Substrate temperature (T_{sub}). The optimum range of target parameter obtained in each set was used in the following set. ZrN films were deposited with 600 Watts plasma power and reactant gas composition of (60 sccm forming gas and 100 sccm argon).

# Set	Target Parameter	Test Range	ALD cycle[a] ($t_1 - t_2 - t_3 - t_4$; T_{sub})	Optimized range[b]
1	T_{sub}	100 °C – 350 °C	0.20 – 15 – 15 – 15; $(T_{sub})^{var}$	100 °C ≤ T_{sub} ≤ 200 °C
2	t_1	0.02 s – 0.20 s	$(t_1)^{var}$ – 15 – 15 – 15; 150 °C	$t_1 \geq 0.10$ s
3	t_3	1 s – 18 s	0.10 – 15 – $(t_3)^{var}$ – 15; 150 °C	$t_3 \geq 4$ s
4	t_2	3 s – 18 s	0.10 – $(t_2)^{var}$ – 9 – 15; 150 °C	$t_2 \geq 9$ s
5	t_4	3 s – 18 s	0.10 – 12 – 9 – $(t_4)^{var}$; 150 °C	$t_4 \geq 3$ s

[a] Target parameter for every experimental set (denoted with *var*) was varied within the test range for 600 Watts plasma and reactant gas composition of 60 sccm forming gas and 100 sccm Ar.
[b] For ZrN growth the ALD temperature window was identified as 100-200 °C with deposition consisted consisting of 0.10s TDMAZr/12s Ar/9s plasma/9s Ar.

5.4.2.1. ALD temperature window

The ALD temperature window is the range of substrate temperature (T_{sub}) for which film growth results primarily from the precursor/reactant reaction at the active sites on substrate surface alone. The lower limit of ALD window is determined by the temperature which is sufficient to overcome activation barrier for surface reaction without causing precursor/reactant condensation at the substrate. While the upper temperature limit is determined by the thermal stability of the metal precursor or desorption of surface adsorbed molecules. Hence it is essential to identify the ALD temperature window before optimizing other process parameters.

An arbitrarily high dose of TDMAZr precursor (t_1) and long plasma exposures (t_3) in combination with sufficiently long inert gas purges (t_2 & t_4) ensures characteristic ALD growth if the substrate temperatures (T_{sub}) is within the ALD temperature window. To determine this temperature range, ZrN films were deposited with t_1 = 0.20 s, t_2 = 15 s, t_3 = 15 s and t_4 = 15 s, for T_{sub} varied in the range of 100 to 350 °C. The average GPC determined from *d-iSE* measurements for ZrN deposition is shown in **Figure 5-4** as a function of T_{sub}.

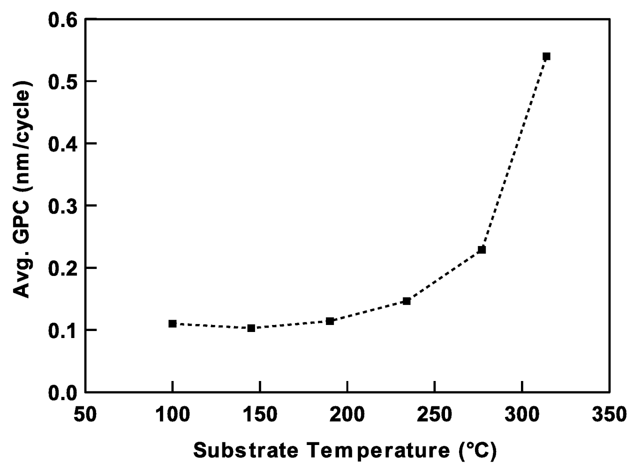

Figure 5-4: Average GPC for ZrN deposition as a function of substrate temperature with 0.20s TDMAZr pulse/15s Ar purge/ 15s plasma/ 15s Ar purge. Surface controlled ALD growth was observed in the temperature range of 100-200 °C with an average GPC 0.109 ± 0.005 nm per cycle.

A steady value of GPC was observed for ZrN growth at T_{sub} in range of 100-200 °C suggesting a surface reaction controlled deposition. A gradual increase in average GPC with T_{sub} higher than 200 °C indicates an increasing contribution from the thermal decomposition of TDMAZr for film growth at higher temperatures and is consistent with CVD growth of ZrN [24]. Thus the temperature range of 100 – 200 °C for ZrN deposition using TDMAZr and forming gas plasma is the ALD temperature window and in agreement with reported ALD studies using similar precursors [1,4,5,25].

5.4.2.2. ALD cycle optimization

At deposition temperatures within the ALD window, a minimum TDMAZr dose and plasma exposure is essential to react with all of available surface sites, leading to surface saturation. Any dosage higher than this minimum does not affect the GPC but adversely affects the ALD throughput due to increased processing time and precursor wastage. Furthermore, the respective inert gas purges are required to be sufficiently long so that all of excess precursor/reactant species and the corresponding reaction by-products are completely evacuated from the reactor. In general metal precursors are more expensive than non-metallic reactants; hence for ZrN PEALD the TDMAZr dose was optimized before other parameters.

To determine the minimum TDMAZr dose to attain surface saturation, ZrN films were deposited with variable precursor pulse ($0.02s \leq t_1 \leq 0.20s$) and arbitrarily long plasma exposure and Ar purges (Set 2 in **Table 5-1**) at T_{sub} = 150 °C. As shown in **Figure 5-5(a)**, for $t_1 < 0.10s$ the GPC was observed to increase with precursor pulse width but attains a steady state value of 0.102 ± 0.001 nm/cycle for $t_1 \geq 0.10s$, thus showing that a minimum of 0.10s pulse of TDMAZr was required to attain self-limiting growth condition.

Figure 5-5: GPC for ZrN deposition at 150 °C substrate temperature as a function of targeted ALD cycle parameters (a) TDMAZr pulse, (b) plasma exposure length, (c) post-precursor purge, and (d) post-plasma purge. The ALD cycle parameters other than the target parameter are listed in Table 5-1.

In the plasma exposure, the active plasma species reacts with surface $Zr(DMA)_x$ (x = 1, 2 or 3) species resulting in the removal of organic ligands and formation of Zr-NH surface species. At sufficiently long plasma exposures, all of the available surface $Zr(DMA)_x$ undergoes reaction and the surface is saturated with Zr-NH species. To determine this minimum plasma exposure, ZrN films were deposited with variable plasma exposure ($1s \leq t_3 \leq 18s$), 0.10 s TDMAZr pulse and long Ar purges (Set 3 in **Table 5-1**) at T_{sub} = 150 °C. As shown in **Figure 5-5(b)**, for $t_3 \geq 4s$ a steady GPC of 0.101 ± 0.001 nm/cycle shows that a minimum exposure of 4s is required to attain surface saturation with respect to plasma half-reaction. Higher GPC values at $t_3 < 4s$ are attributed to incorporation of organic ligands within deposited films from partial plasma reaction as also observed for other PEALD processes [26,27].

A minimum post-precursor purge is necessary for complete removal of excess TDMAZr molecules and respective reaction by-products from ALD reactor. To identify this minimum, ZrN films were deposited with variable post-precursor purges (3s $\leq t_2 \leq$ 18s), 0.10 s TDMAZr pulse, 12s plasma exposure and long post-plasma purges (Set 4 in **Table 5-1**) at T_{sub} = 150 °C. For insufficient purging, the residual precursor molecules would undergo gas-phase reactions during the following plasma exposure. Incorporation of these gas-phase reaction products and the residual by-products from precursor half-reaction within deposited film hence results in higher GPC values for insufficient purging ($t_2 < 9$s) as shown in **Figure 5-5(c)**. For $t_2 \geq 9$s, s steady GPC of 0.102 ± 0.001 nm/cycle indicates that the reactor has been sufficiently purged. Because of the short life-time of plasma reactants and high volatility of their reaction by-products [28] they are conveniently swept away by the continuously flowing Ar gas through the reactor. ZrN deposition with variable post-plasma purges (3s $\leq t_4 \leq$ 18s) for 0.10 s TDMAZr pulse, 15s post-precursor purge and 12s plasma exposure (Set 5 in **Table 5-1**) at T_{sub} = 150 °C, showed a steady state GPC of 0.103 ± 0.001 nm/cycle independent of purge duration, as shown in **Figure 5-5(d)**. However a fairly long post-plasma purge was used to permit multiple *d-iSE* measurements after every ALD cycle.

5.4.3. ZrN PEALD thin film properties

The material properties of ZrN films deposited under self-limiting ALD growth conditions (0.10 s TDMAZr pulse, 12s post precursor purge, 9s plasma exposure and 9s post plasma purge, **Table 5-1**) were characterized for comparison with reported literature data.

The imaginary part of dielectric function of 35.3 nm thick ZrN PEALD film deposited at 150°C substrate temperature as determined from the measured *iSE* data at deposition temperature is shown **Figure 5-6**. The free electron

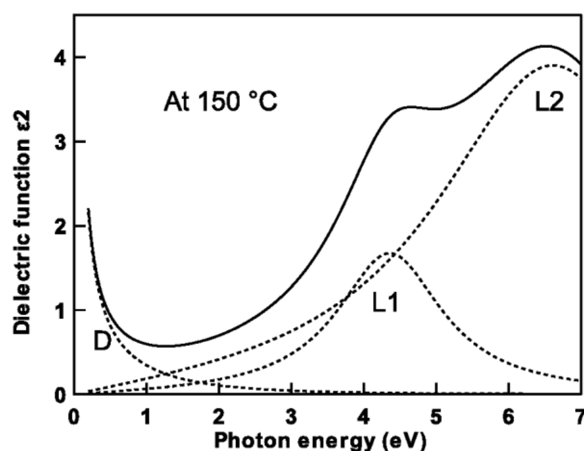

Figure 5-6: Imaginary part of dielectric function (ε_2) for 35.3 nm thick ZrN PEALD film deposited at 150 °C on Si substrate, as determined from iSE data measured at end of deposition without substrate cooling. Free electron dispersion is represented by Drude term (D) while the Lorentz oscillators (L1 and L2) centered at 4.45 eV and 6.89 eV represents the interband optical transitions.

dispersion in the ZrN film was characterized by plasma energy (E_p) of 0.92 ± 0.13 eV and relaxation energy (Γ_r) of 1.95 ± 0.31 eV, while the interband optical transitions described by two Lorentz oscillators, *L1* and *L2* centered at 4.45 ± 0.02 eV and 6.89 ± 0.05 eV respectively. Although free electron dispersion parameters are governed by the finite size effects [18–20], the center energies for Lorentz oscillators as determined for deposited ZrN films are in good agreement with the literature data [16].

XPS survey spectra collected from 35.5 nm thick ZrN film in steps of 0.5 eV with analyzer pass energy of 160 eV, after 3 minutes sputter etching with 4.0 keV Ar^+ ions is shown in **Figure 5-7**. The O (1s and KLL Auger) and C (1s)

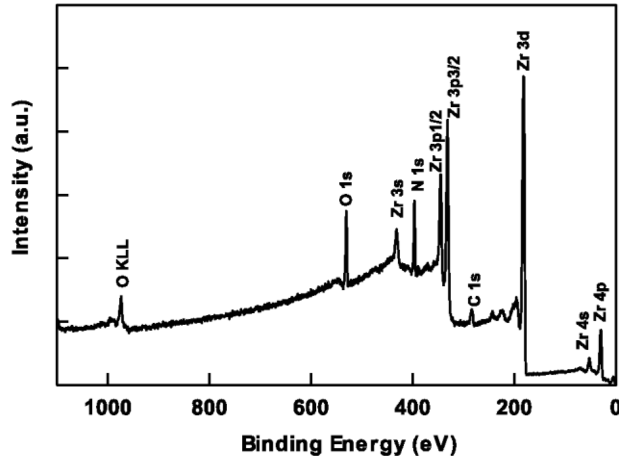

Figure 5-7: XPS survey spectra from 35.5 nm ZrN PEALD film after 3 minutes etching with 4.0 keV Ar^+.

peaks in the survey spectrum shows the presence of oxygen and carbon inclusions in the deposited film. The organic ligands on TDMAZr molecules are responsible for C inclusion, whereas the possible sources for O contamination are investigated in **Chapter 6**.

The valence band (VB) XPS spectrum for PEALD ZrN was collected in 0.05 eV steps with analyzer pass energy of 20 eV as shown in **Figure 5-8**. The photoelectron emission feature at the Fermi level (E_F) shows the metallic nature of the ZrN film, similar to VB emission for sputtered ZrN film as reported in [29]. The XPS valence band studies on ZrN [30-32] have shown that the Fermi level emission band (0 – 2.5 eV) is due to the pure-metallic Zr4d states, whereas the peaks at 5 eV and 15 eV result from hybridized N2p-Zr4d and pure N2s states respectively. For the 5 eV emission peak, the low-energy edge shoulder is consistent with the presence of the Zr_3N_4 phase [31], whereas the high-energy edge shoulder feature could be assigned to O2p states as reported in ZrN/ZrC oxidation studies [33,34]. An additional emission

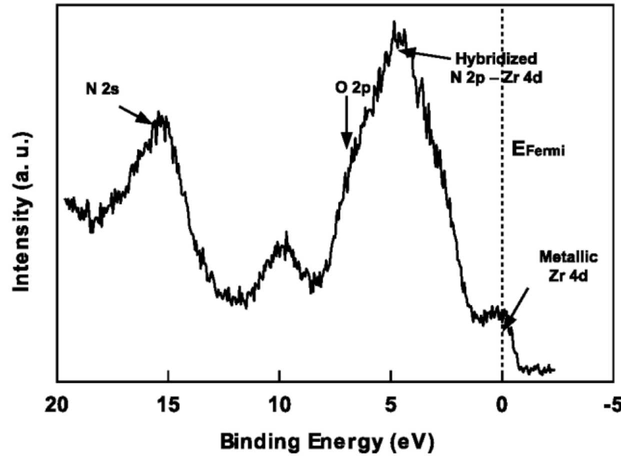

Figure 5-8: Valance-band XPS spectra of 35.5 nm thick ZrN PEALD film deposited at 150 °C.

feature at 10 eV was also reported in [29] and could be assigned either to the presence of a Zr_3N_4 phase [31] or a C2s peak [34,35].

Glancing incidence x-ray diffraction (GIXRD) patterns at 1° incidence from ZrN PEALD film are shown in **Figure 5-9**. For 300 cycle deposition at 150 °C

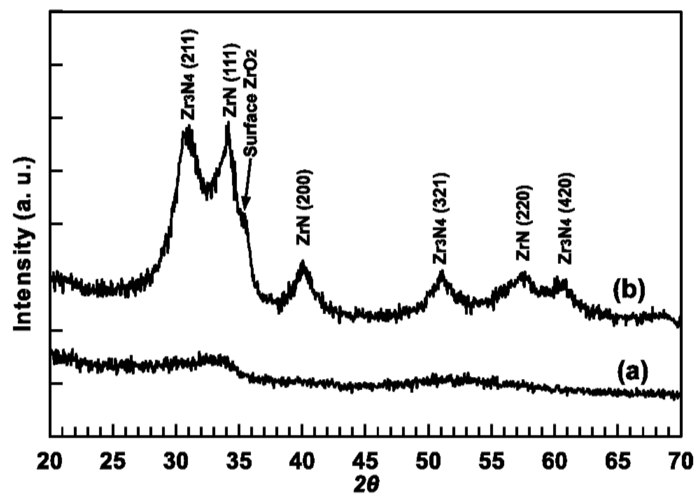

Figure 5-9: GIXRD patterns at 1° incidence from ZrN PEALD films deposited with (a) 300 cycles at 150 °C and (b) 1200 cycle at 225 °C on Si (111) substrates.

only broad diffraction features were observed at 2θ values of 34° and in the 45° - 60° range indicating that ZrN films were primarily amorphous. However

for thicker ZrN films (1200 cycles) deposited at 225 °C, the diffraction peaks corresponding to (111), (200) and (220) planes of ZrN (Powder Diffraction File: 35-0753) were visible. Additional peaks at 32°, 51° and 61° are assigned to (211), (321) and (421) diffraction planes of cubic Zr_3N_4 [36]. The lowest angle peak at 32° has also been indexed as the (320) diffraction plane of orthorhombic Zr_3N_4 [37,38]. A shoulder feature observed at ~ 35° in the diffraction pattern was also reported in ZrN oxidation studies and was assigned to surface oxidized ZrO_2 [39]. For ZrN films deposited at 150 °C, the XRR mass density was found to be 4.24 ± 0.21 grams/cm^3, and was significantly lower than the bulk density of 7.1 grams/cm^3.

Electrical resistivity of ZrN films grown at 150 °C on thermal SiO_2 was determined to be 559.5 μΩ-cm from Van der Pauw sheet resistance measurements. This resistivity is comparable to the electrical resistivity measured for thicker (50 nm) ZrN PEALD films on Si substrate deposited at higher temperatures (T_{sub} > 150 °C) [6]. The electrical resistivity for HfN PEALD films on thermal SiO_2 using H-rich plasma and higher substrate temperatures [5,40] were orders of magnitude higher than for the ZrN PEALD films on thermal SiO_2 using forming gas (5% H_2) plasma at 150 °C. Integration of ZrN PEALD films with GaN based high power device [41] have shown that ZrN provides 8x lifetime improvements over AlN [42].

5.5. Conclusions

PEALD growth characteristics for ZrN deposition using TDMAZr precursor and forming gas plasma is described in this chapter. ZrN growth was

monitored with in-situ spectroscopic ellipsometry measurements in real-time throughout deposition and used in the characterization of ALD in terms of average thickness growth-per-cycle (GPC). An experiment design scheme is presented to determine optimum ALD cycle from a reduced number of depositions.

For ZrN deposition with 0.10s TDMAZr pulse, 12s post precursor purge, 9s plasma pulse and 9s post plasma purge at substrate temperature range of 100-200 °C at 600 Watts plasma, the material properties of PEALD film were characterized using iSE, XPS, XRR, GIXRD, sheet resistance measurements. GIXRD measurements showed that the PEALD grown film was composed of both ZrN and Zr_3N_4 phases. The presence of O and C in the films was indicated by the XPS measurements, and GIXRD peaks indicated the possibility surface ZrO_2. The VB photoemission at Fermi level and electrical resistivity comparable with literature data shows that the ZrN PEALD films were significantly metallic in nature.

5.6. References

[1] J. Musschoot, Q. Xie, D. Deduytsche, S. Van den Berghe, R.L. Van Meirhaeghe, C. Detavernier, Microelectron. Eng. 86 (2009) 72.

[2] B.B. Burton, A.R. Lavoie, S.M. George, J. Electrochem. Soc. 155 (2008) D508.

[3] S.-H. Kim, J.-K. Kim, J.H. Lee, N. Kwak, J. Kim, S.-H. Jung, M.-R. Hong, S.H. Lee, J. Collins, H. Sohn, J. Electrochem. Soc. 154 (2007) D435.

[4] J.S. Becker, E. Kim, R.G. Gordon, Chem. Mater. 16 (2004) 3497.

[5] E.-J. Kim, D.-H. Kim, Electrochem. Solid-State Lett. 9 (2006) C123.

[6] S. Cho, K. Lee, P. Song, H. Jeon, Y. Kim, Jpn. J. Appl. Phys. 46 (2007) 4085.

[7] A. Kafizas, C.J. Carmalt, I.P. Parkin, Coord. Chem. Rev. 257 (2013) 2073.

[8] V. Miikkulainen, M. Leskelä, M. Ritala, R.L. Puurunen, J. Appl. Phys. 113 (2013) 021301.

[9] A.V. Tikhonravov, M.K. Trubetskov, E. Masetti, A.V. Krasilnikova, I.V. Kochikov, in:, C. Amra, H.A. Macleod (Eds.), Adv. Opt. Interf. Coat., 1999, pp. 173–182.

[10] R.L. Puurunen, J. Appl. Phys. 97 (2005) 121301.

[11] R.L. Puurunen, W. Vandervorst, W.F.A. Besling, O. Richard, H. Bender, T. Conard, C. Zhao, A. Delabie, M. Caymax, S. De Gendt, M. Heyns, M.M. Viitanen, M. de Ridder, H.H. Brongersma, Y. Tamminga, T. Dao, T. de Win, M. Verheijen, M. Kaiser, M. Tuominen, J. Appl. Phys. 96 (2004) 4878.

[12] G.A. Bootsma, F. Meyer, Surf. Sci. 14 (1969) 52.

[13] F.H.P.M. Habraken, O.L.J. Gijzeman, G.A. Bootsma, Surf. Sci. 96 (1980) 482.

[14] H. Fujiwara, Spectroscopic Ellipsometry: Principles and Applications, Wiley, West Sussex, UK, 2007.

[15] H.G. Tompkins, E.A. Irene, Handbook of Ellipsometry, William Andrew, 2005.

[16] D. Valerini, M.A. Signore, A. Rizzo, L. Tapfer, J. Appl. Phys. 108 (2010) 083536.

[17] M.A. Signore, D. Valerini, L. Tapfer, G. Caretto, A. Rizzo, J. Vac. Sci. Technol. Vac. Surf. Films 29 (2011) 061507.

[18] C.G. Ribbing, A. Roos, in:, Handb. Opt. Constants Solids, Elsevier, 1997, pp. 351–369.

[19] A. Lehmuskero, M. Kuittinen, P. Vahimaa, Opt. Express 15 (2007) 10744.

[20] S.A. Kovalenko, M. p. Lisitsa, Semicond. Phys. Quantum Electron. Optoelectron. 4 (2001) 352.

[21] M.A. Alam, M.L. Green, J. Appl. Phys. 94 (2003) 3403.

[22] R.L. Puurunen, W. Vandervorst, J. Appl. Phys. 96 (2004) 7686.

[23] J.-W. Lim, H.-S. Park, S.-W. Kang, J. Electrochem. Soc. 148 (2001) C403.

[24] I.-W. Kim, S.-J. Kim, D.-H. Kim, H. Woo, M.-Y. Park, S.-W. Rhee, Korean J. Chem. Eng. 21 (2004) 1256.

[25] J. Wooho, J. Korean Phys. Soc. 56 (2010) 905.

[26] Z. Fang, P.A. Williams, R. Odedra, H. Jeon, R.J. Potter, J. Cryst. Growth 338 (2012) 111.

[27] H. Kim, A.J. Kellock, S.M. Rossnagel, J. Appl. Phys. 92 (2002) 7080.

[28] J. Swerts, A. Delabie, M.M. Salimullah, M. Popovici, M.-S. Kim, M. Schaekers, S. Van Elshocht, ECS Solid State Lett. 1 (2012) P19.

[29] I. Milošev, Surf. Sci. Spectra 5 (1998) 152.

[30] A.L. Ivanovskii, N.I. Medvedeva, S.V. Okatov, Inorg. Mater. 37 (2001) 459.

[31] P. Prieto, L. Galán, J. Sanz, Phys. Rev. B 47 (1993) 1613.

[32] L. Porte, Solid State Commun. 50 (1984) 303.

[33] P. Prieto, L. Galán, J.M. Sanz, Surf. Interface Anal. 21 (1994) 395.

[34] K. Håkansson, H. Johansson, L. Johansson, Phys. Rev. B 48 (1993) 2623.

[35] H. Ihara, M. Hirabayashi, H. Nakagawa, Phys. Rev. B 14 (1976) 1707.

[36] M. Chhowalla, H.E. Unalan, Nat. Mater. 4 (2005) 317.

[37] P. Carvalho, J.M. Chappé, L. Cunha, S. Lanceros-Méndez, P. Alpuim, F. Vaz, E. Alves, C. Rousselot, J.P. Espinós, A.R. González-Elipe, J. Appl. Phys. 103 (2008) 104907.

[38] A. Fragiel, M.H. Staia, J. Muñoz-Saldaña, E.S. Puchi-Cabrera, C. Cortes-Escobedo, L. Cota, Surf. Coat. Technol. 202 (2008) 3653.

[39] G.L.N. Reddy, J.V. Ramana, S. Kumar, S.V. Kumar, V.S. Raju, Appl. Surf. Sci. 253 (2007) 7230.

[40] S. Consiglio, W. Zeng, N. Berliner, E.T. Eisenbraun, J. Electrochem. Soc. 155 (2008) H196.

[41] K.M. Bothe, A.M. Ma, K.J. Voon, D.W. Barlage, A. Afshar, P. Motamedi, T.P. Muneshwar, K.C. Cadien, Polar Source Gallium Nitride MOSFET Structures and Methods of Fabrication, Provisional Patent US 61/967,239

[42] K.M. Bothe, A.M. Ma, K.J. Voon, A. Afshar, T.P. Muneshwar, P. Motamedi, K.C. Cadien, D.W. Barlage, (*In preparation*)

6. Oxygen contamination in ALD nitride films*

6.1. Introduction

Atomic layer deposition of metallic nitrides (TiN, ZrN*, HfN*, TaN*, WN*, etc. where * denotes variable stoichiometry) has several applications in semiconductor fabrication [1,2] such as Cu diffusion barrier layers [3–6], metal contacts [7,8], etc. More recent efforts in nitride ALD are directed towards the deposition of semiconducting group-III-nitrides [9] like AlN, GaN, InN, $Al_xGa_{1-x}N$, $In_xGa_{1-x}N$, etc. Analytical techniques such as XPS [9–11], RBS [12,13], etc., have shown that the nitride films grown with thermal or plasma assisted ALD are impaired with O contamination (as high as 20%). Although different mechanisms for oxygen incorporation within nitride ALD films have been proposed [13,14], in-depth studies on determination of O source and process parameters affecting the level of contamination are lacking.

In this chapter O-contamination within ZrN PEALD films is investigated with aim towards identifying its source to one of the following: (a) residual O_2/H_2O from ALD reactor walls and/or from the process gases; (b) ICP plasma related O-source, (i.e. formation of SiO cluster from plasma interactions with quartz

---

* A version of this chapter will be submitted for publication

tube [14]); (c) surface oxidation of ZrN ALD films on exposure to ambience, and (d) Ar^+ ions bombardment related features during depth-profile [15].

6.2. Experimental Procedure

To ascertain the source/sources of O-contamination careful experiments were performed investigating each source separately. Prior to deposition in the ALD reactor, precursor valves, reactant lines were baked at high temperatures (90-130 °C) for ~24 hrs. The residual O_2/H_2O content in the process gases (i.e. Ar, forming gas, and N_2), was determined from quadruple mass spectrometer residual gas analyzer (QMS-RGA). The emission spectrum during process gas plasma was recorded to detect possible presence of SiO fragments as reported in [14]. PEALD grown 30-40 nm thick ZrN films at 150 °C with 0.1 s TDMAZr pulse/ 12 s Ar purge/ 9 s forming gas plasma exposure (600 Watts)/ 9 s Ar purge were studied. XPS depth-profile with 4.0 keV Ar^+ ion sputtering was performed to record high-resolution emission features corresponding to O1s and Si2p core levels.

6.3. Results and discussion

6.3.1. Residual H_2O/O_2 in process gases

In a continuous flow reactor the ZrN PEALD films were deposited under constant flow of Ar gas (~1 Torr), used as a carrier gas for the transport of precursor/reactant and as the curtain gas to confine precursor/reactant flux close to the substrate. High purity N_2 gas was also used for purging load-lock (~10^{-6} Torr) during automated transfer of substrate in and out of the ALD reactor. Hence these process gases (Ar, forming gas (FG), and N_2) were

analyzed for residual O_2/H_2O concentrations using RGA (AccuQuad, Kurt J. Lesker). The measured QMS spectra in **Figure 6-1** for process gases shows that the residual water vapour or oxygen content if present was within the background signal (~1.6 x 10^{-7} Torr) measured at absence of process gas flow. This suggests that the process gases could not have been a significant source of the O-concentration as detected within ZrN films.

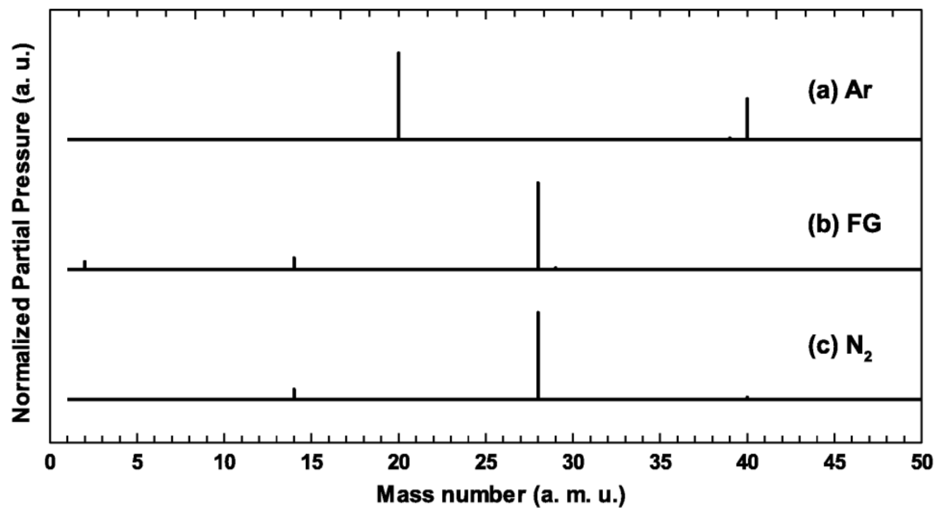

Figure 6-1: RGA spectra of process gas (a) Argon, (b) Forming gas (FG), and (c) Nitrogen. An offset has been added to the ordinate axis representing normalized partial pressure of the gas components for clarity. Absolute pressure corresponding to H_2O was found to be within background 1.6 x 10^{-7} Torr in (a)-(c).

6.3.2. Plasma source related O-contamination

In recent publications [9, 16–18] a good control on O-content within PEALD nitride films have been demonstrated with the application of an alternate plasma source in place of quartz confined ICP plasma. This switch from ICP was based upon the earlier works [14] reporting the formation of SiO from plasma interactions with the quartz tube based on plasma emission measurements. However, detailed investigations establishing the ICP plasma source as the primary source of O-contamination are missing. In addition, a

recent publication in the literature [18] questions advantage of the alternate plasma source over conventional ICP source. The proposed hypothesis was therefore tested by looking for plasma emissions characteristic of SiO fragments and presence of Si2p core-level emission in deposited films using high resolution XPS.

The emission spectra for 600 Watts Ar, N_2 and reactant gas (FG + Ar mix) plasma over range of wavelength characteristic to SiO emission peaks at 229.9 nm, 234.4 nm, 266.9 nm and 269.4 nm [19] is shown in **Figure 6-2**. None of the SiO emission peaks were observed in the measured emission spectra to suggest formation of SiO species. In the original work [14] the emission peak at 295 nm corresponding to N [20] was wrongly assigned to SiO.

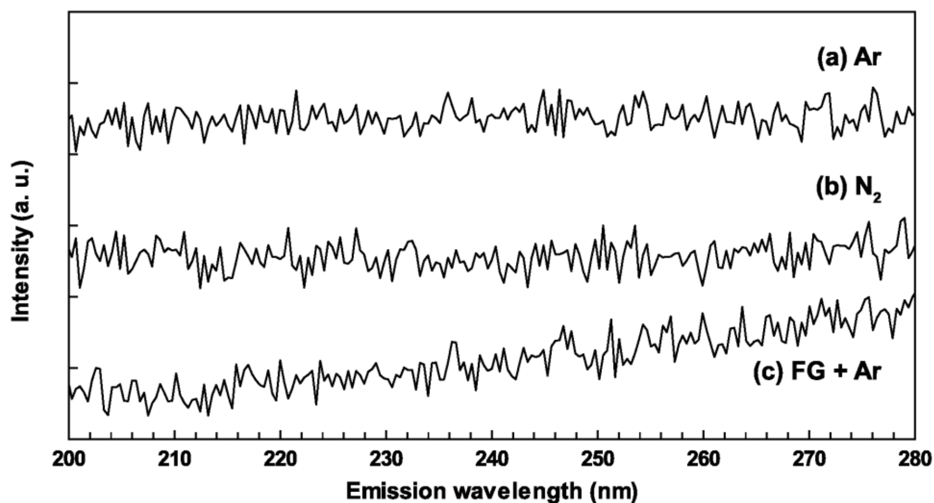

Figure 6-2: OES spectra in 200-280 nm range, measured at the substrate during (a) Argon, (b) Nitrogen, and (c) reactant gas (forming gas + Argon) plasma. None of the characteristics SiO emission peaks at 229.9 nm, 234.4 nm, 266.9 nm and 269.4 nm could be distinguished from background noise in spectra (a)-(c).

Furthermore, the incorporation of SiO fragments generated within the quartz tube of ICP, within ZrN PEALD films would have resulted in the presence of an equivalent amount of Si in addition to O. However the high resolution XPS data, as shown in **Figure 6-3**, does not show Si within detectable limits.

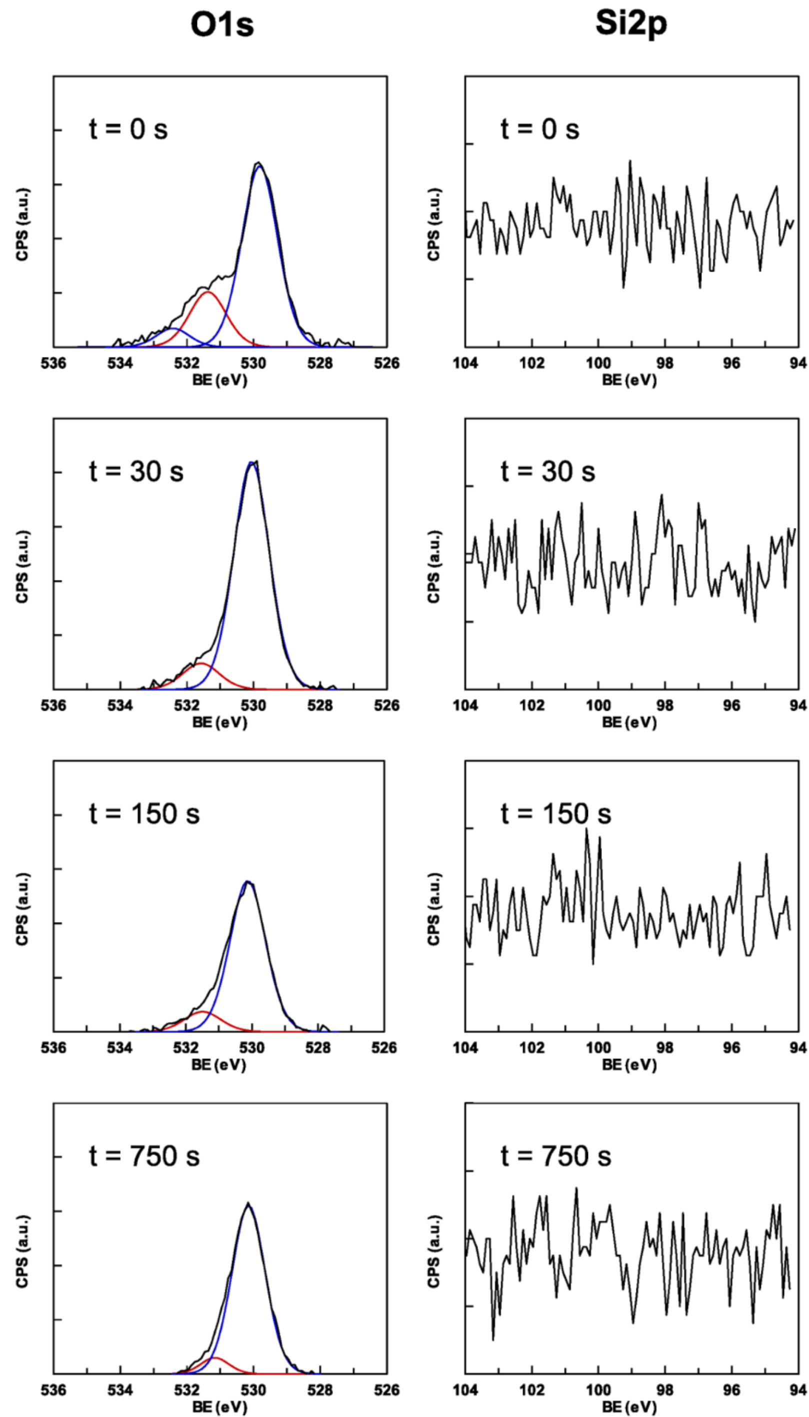

Figure 6-3: High resolution XPS core-level O1s and Si2p emission from ZrN PEALD film at 0s, 30s, 150s, and 750s of 4.0 keV Ar ion sputtering.

Thus the plasma emission and high-resolution XPS measurement disproves the hypothesis that ICP quartz tube could be the source of high levels of O-content within nitride PEALD films.

6.3.3. Surface Oxidation

ZrN oxidation studies [21] have shown the rapid formation of surface ZrO_2 on exposure of ZrN films to air. After the initial native oxide growth, the oxidation rate is limited by oxygen diffusion through already grown ZrO_2 layer [22]. The faster oxidation rate of ZrN compared to Zr [21] may be attributed to the evolution of N_2 gas during oxidation. The depth-profile XPS studies on thermal annealing of ZrN [23] shows that the oxidation is accompanied with rapid depletion of N concentration as function of annealing time.

The O content in TiN atomic layer epitaxy films were found to depend upon the film thickness [13]. Also PEALD growth of Ta and TaN films [24,25] reported negligible O-content for samples capped with in-situ sputtered thick copper film compared to 5-10 atomic % for uncapped samples. These observations suggest that surface oxidation forms a major source of O content within nitride films. The presence of O only as surface oxide layer is also consistent with the electrical resistivity and valence band feature at Fermi level measured on thick ZrN films as shown in Chapter 5.

6.3.4. Oxygen depth-profile

If the surface oxidation hypothesis is correct the oxygen concentration in the depth-profile should decrease as a function of depth into the film. However the O-content was observed to be uniformly distributed throughout film thickness in the XPS spectra measured at different sputter times as shown in **Figure 6-3** and also reported in [13]. The possible explanations for uniform O-distribution are: (a) the ZrN films are porous or, (b) the depth-profile analysis technique induced O-redistribution from surface oxide. If possibility (a) was true, ZrN thin film exposure to atmospheric oxygen would have led to a rapid formation of oxynitride phase. However the valence-band features in XPS and the electrical resistivity of deposited films are inconsistent with the properties of the Zr-oxynitrides [26, 27].

During XPS/AES depth-profiling the sample surface is sputtered with energetic Ar ions and the sample surface is analysed at different sputter depths. The energy and momentum transfer from argon ion impingement initiates a collision cascade within the solid resulting in processes such as ion implantation, defect generation, atomic mixing, atomic migration, preferential sputtering, radiation enhanced diffusion, etc., of which sputtering is the least significant [28]. The ion-solid interactions depend upon the energy and incidence angle of the ion beam and often distort the original atomic concentration profile, making it difficult to interpret the measured concentration-profile [15, 29–32]. The energy and dose of Ar ions used for surface treatment prior to XPS, have also been observed to affect the shape of emission features [33,34].

With the preferential sputtering of surface N atoms, the uniform distribution of O-content within ZrN PEALD film could be explained on the basis of sputter induced transport [30–32] of O and N atoms across oxide/ZrN interface. Similar model has been proposed for the oxidation of Ni films under influence of Ar ion bombardment [35].

6.4. Conclusions

The O contamination within ZrN PEALD nitride films was systematically investigated from the possible sources of inclusion. The residual moisture content in process gases was found to be negligible within background QMS-RGA signal (~1.6 x 10^{-7} Torr). The proposed mechanism of O contamination from ICP quartz tube not supported based on the absence of SiO characteristic peaks at 229.9 nm, 234.4 nm, 266.9 nm and 269.4 nm in the plasma emissions along with lack of any evidence of SiO presence within ZrN films from high-resolution Si2p core-level XPS. From the electrical resistivity and valence band features in XPS, the surface oxidation was identified as a primary source of O within ZrN PEALD films. The uniform distribution of O throughout film thickness as observed from XPS depth profile is explained on the basis of well-established ion-bombardment induced surface effects.

6.5. References

[1] H. Kim, J. Vac. Sci. Technol. B Microelectron. Nanometer Struct. 21 (2003) 2231.

[2] V. Miikkulainen, M. Leskelä, M. Ritala, R.L. Puurunen, J. Appl. Phys. 113 (2013) 021301.

[3] S. Cho, K. Lee, P. Song, H. Jeon, Y. Kim, Jpn. J. Appl. Phys. 46 (2007) 4085.

[4] H.C.M. Knoops, L. Baggetto, E. Langereis, M.C.M. van de Sanden, J.H. Klootwijk, F. Roozeboom, R.A.H. Niessen, P.H.L. Notten, W.M.M. Kessels, J. Electrochem. Soc. 155 (2008) G287.

[5] A.E. Kaloyeros, E. Eisenbraun, Annu. Rev. Mater. Sci. 30 (2000) 363.

[6] J. Wooho, J. Korean Phys. Soc. 56 (2010) 905.

[7] S. Consiglio, W. Zeng, N. Berliner, E.T. Eisenbraun, J. Electrochem. Soc. 155 (2008) H196.

[8] P. Caubet, T. Blomberg, R. Benaboud, C. Wyon, E. Blanquet, J.-P. Gonchond, M. Juhel, P. Bouvet, M. Gros-Jean, J. Michailos, C. Richard, B. Iteprat, J. Electrochem. Soc. 155 (2008) H625.

[9] C. Ozgit-Akgun, I. Donmez, N. Biyikli, ECS Trans. 58 (2013) 289.

[10] C. Ozgit, I. Donmez, M. Alevli, N. Biyikli, Thin Solid Films 520 (2012) 2750.

[11] C. Ozgit, I. Donmez, M. Alevli, N. Biyikli, J. Vac. Sci. Technol. Vac. Surf. Films 30 (2012) 01A124.

[12] J.S. Becker, E. Kim, R.G. Gordon, Chem. Mater. 16 (2004) 3497.

[13] M. Ritala, J. Electrochem. Soc. 142 (1995) 2731.

[14] K.S.A. Butcher, Afifuddin, P.P.-T. Chen, T.L. Tansley, Phys. Status Solidi C 0 (2003) 156.

[15] J.W. Coburn, J. Vac. Sci. Technol. 13 (1976) 1037.

[16] S. Bolat, C. Ozgit-Akgun, B. Tekcan, N. Biyikli, A.K. Okyay, Appl. Phys. Lett. 104 (2014) 243505.

[17] E. Goldenberg, C. Ozgit-Akgun, N. Biyikli, A. Kemal Okyay, J. Vac. Sci. Technol. Vac. Surf. Films 32 (2014) 031508.

[18] C. Ozgit-Akgun, E. Goldenberg, A.K. Okyay, N. Biyikli, J. Mater. Chem. C 2 (2014) 2123.

[19] A.G. Gaydon, Identification of Molecular Spectra., Springer, [S.l.], 2013.

[20] A. Kramida, Yu. Ralchenko, J. Reader, and NIST ASD Team, NIST Atomic Spectra Database, 2013.

[21] N. Farkas, G. Zhang, E.A. Evans, R.D. Ramsier, J.A. Dagata, J. Vac. Sci. Technol. Vac. Surf. Films 21 (2003) 1188.

[22] L. Krusin-Elbaum, M. Wittmer, Thin Solid Films 107 (1983) 111.

[23] G.L.N. Reddy, J.V. Ramana, S. Kumar, S.V. Kumar, V.S. Raju, Appl. Surf. Sci. 253 (2007) 7230.

[24] H. Kim, C. Cabral, C. Lavoie, S.M. Rossnagel, J. Vac. Sci. Technol. B Microelectron. Nanometer Struct. 20 (2002) 1321.

[25] H. Kim, A.J. Kellock, S.M. Rossnagel, J. Appl. Phys. 92 (2002) 7080.

[26] M. Laurikaitis, S. Burinskas, J. Dudonis, D. Milčius, J. Phys. Conf. Ser. 100 (2008) 082051.

[27] P. Carvalho, J.M. Chappé, L. Cunha, S. Lanceros-Méndez, P. Alpuim, F. Vaz, E. Alves, C. Rousselot, J.P. Espinós, A.R. González-Elipe, J. Appl. Phys. 103 (2008) 104907.

[28] S. Hofmann, J. Vac. Sci. Technol. B Microelectron. Nanometer Struct. 10 (1992) 316.

[29] S. Hofmann, Rep. Prog. Phys. 61 (1998) 827.

[30] Z.L. Liau, J. Vac. Sci. Technol. 16 (1979) 121.

[31] A. Galdikas, Vacuum 55 (1999) 51.

[32] S. Loualiche, C. Lucas, P. Baruch, J.P. Gailliard, J.C. Pfister, Phys. Status Solidi A 69 (1982) 663.

[33] C. Morant, J. Sanz, L. Galán, Phys. Rev. B 45 (1992) 1391.

[34] E. Lewin, M. Gorgoi, F. Schäfers, S. Svensson, U. Jansson, Surf. Coat. Technol. 204 (2009) 455.

[35] J.C. de Jesús, P. Pereira, J. Carrazza, F. Zaera, Surf. Sci. 369 (1996) 217.

7. Unconventional ALD: AABAAB… type*

7.1. Introduction

Atomic layer deposition has numerous technologically advanced applications [1–3]. A unique feature of ALD growth is the surface reactions A and B, in a sequence ABAB…, that self-terminates on surface saturation. These ALD surface reactions allow for a uniform and conformal deposition over entire substrate surface, but limits film growth to a single monolayer per deposition cycle under ideal conditional. ALD growth studies [3–8] have shown that only a partial monolayer deposition could be obtained per deposition cycle. The deviation from "*ideal*" ALD growth is due to surface reaction kinetics to attain saturation and largely because of the shadowing effects of bulky precursor molecules preventing adjacent surface active sites from participating in reactions, a steric factor.

A conventional way to overcome kinetic factors for ALD reactions is to introduce excess precursor/reactant dosage (>100 Langmuir) into the reaction, thus promoting surface saturation. Although ALD growth per cycle (GPC) increases with dosage, the utilization of precursor/reactant species is rather poor and any excess unreacted species are pumped out of the reactor and goes waste. With this approach, the surface monolayer growth is still limited by the steric factors from bulky ligands on the adsorbed precursor molecules.

---

* A version of this chapter will be submitted for publication

In this chapter an alternative AABAAB… type of ALD growth is investigated with potential to overcome steric hindrance factors in combination with improved precursor/reactant utilization. A numerical model for conventional ABAB… type ALD growth is developed accounting for steric hindrance factors on the basis of fundamental surface reaction steps. Extending this model to AABAAB… type ALD, the numerical results are compared with ABAB… type deposition. Finally a comparison of ZrN PEALD growth with ABAB… and AABAAB… deposition cycle is presented.

7.2. Growth model for ABAB… type ALD

The theoretical description of ABAB… type ALD in partial monolayer growth regime has been covered in [9–18]. The ALD surface reactions during precursor (A) and reactant (B) pulse are schematically represented in **Figure 7-1**. The first-principle model for ALD growth is developed, keeping track of the fractional coverage of surface species, i.e. reactive sites, adsorbed precursor molecules and fragments of ALD grown film, after every ALD half-reaction starting from a bare substrate.

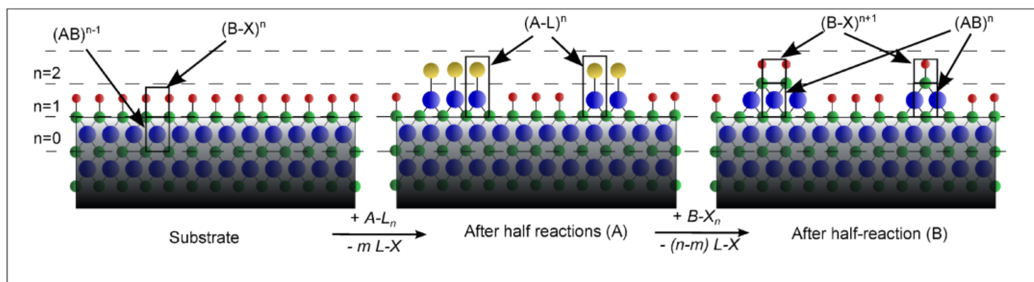

Figure 7-1: Schematic of ALD surface reaction with precursor pulse ($A\text{-}L_n$) and the reactant ($B\text{-}X_n$) pulse. Dashed lines represent the thickness of ALD grown monolayers (indexed as n=1, 2…). The substrate surface has been indexed as n=0. Surface species are shown with rectangles with superscript denoting the monolayer index. (A, B, L and X are denoted by blue, green, yellow and red spheres respectively)

7.2.1. ALD surface reactions

ALD growth, as shown in **Figure 7-1**, can be completely described by the population of surface species, i.e. *B-X*, *A-L* and *A-B* units, as they evolve with every surface reaction step. Hence it is sufficient to track surface concentration or fractional coverage (θ) of these surface species to numerically model the ALD growth. In general the surface reaction kinetics is given by:

$$\frac{d\theta_{site}^{species}}{dt_{dose}} = C_{site}^{species}(1-\theta_{sites}^{species})^{k} - D_{site}^{species}(\theta_{sites}^{species})^{l} \quad \textbf{(7.1)}$$

Where $d\theta_{site}^{species}$ denotes the change in coverage of a species at reaction site over time interval dt. The kinetics of surface reaction depends upon the order k and effective kinetic parameter $C_{site}^{species}$ which is a function of partial pressure of species and the activation energy for surface reaction. For the sake of completion, the desorption reaction of order l with effective kinetic parameter $D_{site}^{species}$ is also included in **Eq. (7.1)**.

Assuming a first-order surface reaction, ($k = 1$) with negligible desorption $(D_{site}^{species} \to 0)$, the solution to **Eq. (7.1)** can be expressed as:

$$\theta_{sites}^{species} = \theta_{sites}(1-\exp(-C_{sites}^{species}t_{species})) \quad \textbf{(7.2)}$$

The initial concentration of active sites available for surface reaction is represented by θ_{sites} and $t_{species}$ is the duration of species exposure. With this formulation, the ALD partial reactions during precursor $A\text{-}L_n$ pulse of duration t_A (reaction *A*) and reactant $B\text{-}X_n$ pulse of duration t_B (reaction B) are expressed as:

$$\begin{aligned}\theta_{B-X}^{A-L} &= \theta_{B-X}(1-\exp(-C_{B-X}^{A-L}\cdot t_A)) \\ \theta_{A-L}^{B-X} &= \theta_{A-L}(1-\exp(-C_{A-L}^{B-X}\cdot t_B))\end{aligned} \qquad \textbf{(7.3)}$$

Where, θ_{B-X} and θ_{A-L} are the surface concentrations of active sites available for reaction A and B with kinetic factors C_{B-X}^{A-L} and C_{A-L}^{B-X} respectively. Hence for ALD growth on n^{th} monolayer during k^{th} deposition cycle, the partial reactions *A(k)* and *B(k)* can be mathematically represented by a set of recurring equations as:

$$\begin{aligned}
{}^{A(k)}\theta^{AB,n} &= {}^{B(k-1)}\theta^{AB,n} + {}^{B(k-1)}\theta_{A(k)}^{AB,n} \\
{}^{A(k)}\theta^{A-L,n} &= {}^{B(k-1)}\theta^{A-L,n} + {}^{B(k-1)}\theta_{A(k)}^{A-L,n} \\
{}^{A(k)}\theta^{B-X,n} &= {}^{B(k-1)}\theta^{B-X,n} + {}^{B(k-1)}\theta_{A(k)}^{B-X,n} \\
{}^{B(k)}\theta^{AB,n} &= {}^{A(k)}\theta^{AB,n} + {}^{A(k)}\theta_{B(k)}^{AB,n} \\
{}^{B(k)}\theta^{A-L,n} &= {}^{A(k)}\theta^{A-L,n} + {}^{A(k)}\theta_{B(k)}^{A-L,n} \\
{}^{B(k)}\theta^{B-X,n} &= {}^{A(k)}\theta^{B-X,n} + {}^{A(k)}\theta_{B(k)}^{B-X,n} \\
{}^{B(k)}\theta^{B-X,n+1} &= {}^{A(k)}\theta^{B-X,n+1} + {}^{A(k)}\theta_{B(k)}^{B-X,n+1}
\end{aligned} \qquad \textbf{(7.4)}$$

Where ${}^{B(k-1)}\theta_{A(k)}^{i,n}$ denotes the change in the surface coverage of *species i* (θ^i) from pulse-B of *(k-1)*th cycle to pulse-A of the kth cycle. The coverage of *species i* (θ^i) at the end of pulse-A of kth deposition cycle is simple denoted by ${}^{A(k)}\theta^i$.

As shown in **Figure 7-1**, the ALD reaction-*A* on a particular monolayer (n^{th} layer) leads to the formation of *A-L* units consuming equivalent number of *B-X* units (See **Eq.(7.3)**), without affecting the concentration of *AB* units. Similarly reaction-*B* results in the formation of *AB* units by consumption of equivalent number of *A-L* units (See **Eq.(7.3)**) without affecting the concentration of *B-X* units. Also for every *AB* unit formed on n^{th} monolayer, *B-X* unit is formed in the *(n+1)*th layer.

The steric factor prevents precursor/reactant molecules from undergoing reaction with immediate-adjacent surface active sites. To include this steric effect into the ALD reaction model, the effective number of the available active surface sites during reaction A and B are reduced by a factor of m_{A-L} and m_{B-X} respectively, on similar lines as [15–18]. Hence the surface reactions during k^{th} ALD cycle, incorporating steric effects can be expressed as:

$$
\begin{aligned}
{}^{B(k-1)}\theta_{A(k)}^{AB,n} &= 0 \\
{}^{B(k-1)}\theta_{A(k)}^{A-L,n} &= \left({}^{B(k-1)}\theta^{B-X,n} / m_{A-L}\right)\cdot(1-\exp(-C_{B-X}^{A-L}\cdot t_A)) \\
{}^{B(k-1)}\theta_{A(k)}^{B-X,n} &= -\left({}^{B(k-1)}\theta_{A(k)}^{A-L,n}\right) \\
{}^{A(k)}\theta_{B(k)}^{AB,n} &= \left({}^{A(k)}\theta^{A-L,n} / m_{B-X}\right)\cdot(1-\exp(-C_{A-L}^{B-X}\cdot t_B)) \\
{}^{A(k)}\theta_{B(k)}^{A-L,n} &= -\left({}^{A(k)}\theta_{B(k)}^{AB,n}\right) \\
{}^{A(k)}\theta_{B(k)}^{B-X,n} &= 0 \\
{}^{A(k)}\theta_{B(k)}^{B-X,n+1} &= {}^{A(k)}\theta_{B(k)}^{AB,n}
\end{aligned}
\qquad \textbf{(7.5)}
$$

Using the initial conditions ${}^{B(0)}\theta^{AB,1} = 0$, ${}^{B(0)}\theta^{A-L,1} = 0$ and ${}^{B(0)}\theta^{B-X,1} = 1$, to represent bare substrate before deposition, the ALD growth after every half-reaction could be determined from solution to **Eq. (7.4)-(7.5)**.

7.2.2. ALD film growth

Using **Eq. (7.4)-(7.5)**, the generalized ALD of *AB* is described as multilayered (*m-layers*) growth [12–14], where the ALD surface reactions are restricted to the topmost *m* incomplete layers. For example when starting from substrate *(n=0)*, if by end of *(k-1)^st^* deposition cycle the *(n-1)^th^* layer is complete, i.e. ${}^{B(k-1)}\theta^{B-X,n-1} \rightarrow 0$, ${}^{B(k-1)}\theta^{A-L,\mathrm{n}-1} \rightarrow 0$ & ${}^{B(k-1)}\theta^{AB,\mathrm{n}-1} \rightarrow 1$, ALD surface reactions are restricted for layers *n* to *n+m-1*. The reaction kinetics for precursor/reactant reaction at these multiple layers are represented as factors

$C^{A-L}_{B-X,i}$ and $C^{B-X}_{A-L,i}$ were the index goes sequentially from *i=1* to *i=m* for surface reactions on n^{th} layer to *n+m-1* layer. For such multilayered ALD growth, the surface reactions on the topmost *m-layers* after pulse-A and pulse-B are described by **Eq. (7.6)** and **Eq. (7.7)** respectively:

Surface reaction during pulse-A:

$$\begin{bmatrix} {}^{A(k)}\theta^{AB,n} = {}^{B(k-1)}\theta^{AB,n} \\ {}^{A(k)}\theta^{A-L,n} = {}^{B(k-1)}\theta^{A-L,n} + ({}^{B(k-1)}\theta^{B-X,n} / m_{A-X}) \cdot (1-\exp(-C^{A-L}_{B-X,1} \cdot t_A)) \\ {}^{A(k)}\theta^{B-X,n} = {}^{B(k-1)}\theta^{B-X,n} - ({}^{B(k-1)}\theta^{B-X,n} / m_{A-X}) \cdot (1-\exp(-C^{A-L}_{B-X,1} \cdot t_A)) \\ \vdots \\ {}^{A(k)}\theta^{AB,n+(m-1)} = {}^{B(k-1)}\theta^{AB,n+(m-1)} \\ {}^{A(k)}\theta^{A-L,n+(m-1)} = {}^{B(k-1)}\theta^{A-L,n+(m-1)} + ({}^{B(k-1)}\theta^{B-X,n+(m-1)} / m_{A-X}) \cdot (1-\exp(-C^{A-L}_{B-X,\mathrm{m}} \cdot t_A)) \\ {}^{A(k)}\theta^{B-X,n+(m-1)} = {}^{B(k-1)}\theta^{B-X,n+(m-1)} - ({}^{B(k-1)}\theta^{B-X,n+(m-1)} / m_{A-X}) \cdot (1-\exp(-C^{A-L}_{B-X,m} \cdot t_A)) \\ {}^{A(k)}\theta^{B-X,n+m} = {}^{B(k-1)}\theta^{B-X,n+m} \end{bmatrix} \quad \textbf{(7.6)}$$

Surface reaction during pulse-B:

$$\begin{bmatrix} {}^{B(k)}\theta^{AB,n} = {}^{A(k)}\theta^{AB,n} + ({}^{A(k)}\theta^{A-L,n} / m_{B-X}) \cdot (1-\exp(-C^{B-X}_{A-L,1} \cdot t_B)) \\ {}^{B(k)}\theta^{A-L,n} = {}^{A(k)}\theta^{A-L,n} - ({}^{A(k)}\theta^{A-L,n} / m_{B-X}) \cdot (1-\exp(-C^{B-X}_{A-L,1} \cdot t_B)) \\ {}^{B(k)}\theta^{B-X,n+1} = {}^{A(k)}\theta^{B-X,n+1} + ({}^{A(k)}\theta^{A-L,n+1} / m_{B-X}) \cdot (1-\exp(-C^{B-X}_{A-L,1} \cdot t_B)) \\ \vdots \\ {}^{B(k)}\theta^{AB,n+(m-1)} = {}^{A(k)}\theta^{AB,n+(m-1)} + ({}^{A(k)}\theta^{A-L,n+(m-1)} / m_{B-X}) \cdot (1-\exp(-C^{B-X}_{A-L,m} \cdot t_B)) \\ {}^{B(k)}\theta^{A-L,n+(m-1)} = {}^{A(k)}\theta^{A-L,n+(m-1)} - ({}^{A(k)}\theta^{A-L,n+(m-1)} / m_{B-X}) \cdot (1-\exp(-C^{B-X}_{A-L,m} \cdot t_B)) \\ {}^{B(k)}\theta^{B-X,n+\mathrm{m}} = {}^{A(k)}\theta^{B-X,n+m} + ({}^{A(k)}\theta^{A-L,n+m} / m_{B-X}) \cdot (1-\exp(-C^{B-X}_{A-L,m} \cdot t_B)) \\ {}^{B(k)}\theta^{B-X,n} = {}^{A(k)}\theta^{B-X,n} \end{bmatrix} \quad \textbf{(7.7)}$$

The average thickness of the ALD film, d_{ALD} in units of monolayers, is expressed as $d_{ALD} = (n-1) + \sum_{i=n}^{n+m-1} \theta^{AB,i}$, where *m* is the allowed number of partial monolayer above underlying (*n-1*) complete layers. A theoretical growth rate per cycle is estimated from the linear fit between the theoretical ALD thickness and the number of deposition cycles in the linear growth

regime. Theoretical ALD film thickness obtained from the solution of **Eq. (7.6) - (7.7)** plotted against deposition cycle in **Figure 7-2**.

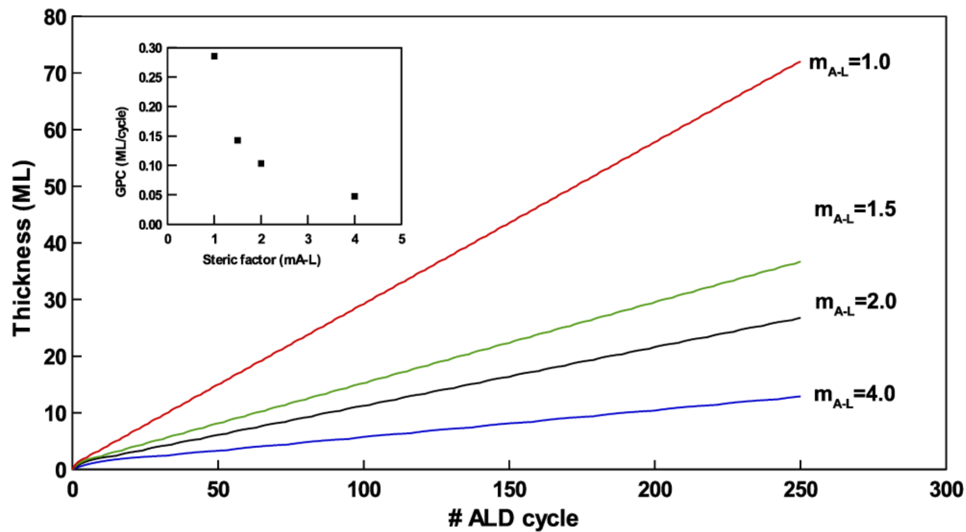

Figure 7-2: Modeled ALD film thickness as a function of deposition cycles obtained from **Eq. (7.6)** and **Eq. (7.7)** for the precursor steric factor (m_{A-L}) varied as 1.0, 1.5, 2.0 and 4.0 assuming no steric hindrance from reactant molecules (m_{B-X} =1). From the linear fit between thickness and number of deposition cycles the determined GPC (units: ML/cycle) is shown as a function of m_{A-L} (Inset). Precursor and reactant pulses along with other surface reaction kinetic parameters were kept the same in these calculations (see text for details). GPC of less than 1 ML/cycle at m_{A-L} =1 suggests that the precursor pulse used in this calculation was shorter than that required for surface saturation

In these calculations the precursor $A\text{-}L_n$ and reactant $B\text{-}X_n$ pulses were arbitrarily kept at 1 s and 9 s respectively, and the surface reactions were modelled so as to allow up to 3 partial monolayers (*m=3*). The kinetic parameter $C_{B-X,i}^{A-L}$, for adsorption of precursor $A\text{-}L_n$ on surface *B-X* sites was assumed to vary as 1.800, 0.540 and 0.162 for reaction at the first, the second and the third partial monolayer respectively, while for the reaction of $B\text{-}X_n$ at surface *A-L* sites a constant $C_{A-L,i}^{B-X}$ of 3.8 was used at all 3 partial monolayers. The effect of steric factors on ALD growth is demonstrated by varying the

numerical value of $m_{A\text{-}L}$ as 1.0 (no steric hindrance), 1.5, 2.0 and 4.0 respectively for $m_{B\text{-}X}=1$.

7.3. Growth model for AABAAB… type ALD

The steric hindrance factor adversely affects the GPC during ALD, as shown in **Figure 7-2**(inset), the higher the steric factor the lower the observed GPC. A schematic of the precursor reaction is shown in **Figure 7-3**(a), where the bulky ligands (*L*) on adsorbed molecules prevent further adsorption on adjacent surface sites, represented by region (*S1*). These ligands are removed as by-products (*L-X*) of the precursor ($A\text{-}L_n$) reaction at surface *B-X* sites, as shown in **Figure 7-3(b)** and freeing up the adjacent surface sites (region *S1* reduced to *S2*). The conventional approach to overcome steric hindrance in

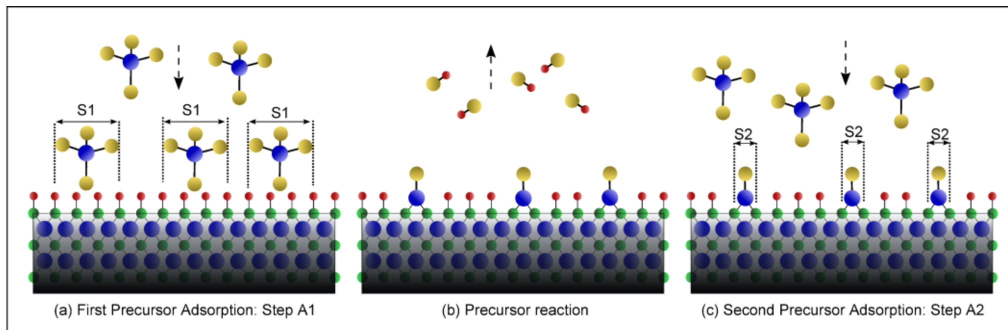

Figure 7-3: (a) Precursor ($A\text{-}L_x$) adsorption at surface sites (B-X) with effective shadowed region (S1); (b) decrease in the volume of adsorbed molecules from removal of ligands (L-X); and (c) the reduced steric hindrance (S2) is utilized for step A2 of AABAAB… type deposition.

ABAB… type deposition has been to introduce a large dose of precursor ($A\text{-}L_n$) molecules in the reactor in single step (pulse-A) such that the precursor surface reaction as shown in **Figure 7-3** attain surface saturation. Although this approach ensures surface saturation at sufficiently large precursor dose, the precursor utilization is quite poor and improvement in GPC is marginal.

Hence a modified deposition cycle (AABAAB…) appears to potentially reduce steric effects with simultaneous improvement in ALD precursor utilization.

In the proposed AABAAB… deposition the precursor species ($A\text{-}L_n$) is introduced in the reactor as two individual pulses (henceforth referred to as pulse-*A1* and pulse-*A2*) separated by an inert purge. After surface reaction of precursor molecules of pulse-*A1*, the effective shadowed region decreases from *S1* to *S2*. The newly exposed surface sites become available for reaction with precursor molecules of pulse-*A2*, as shown in **Figure 7-3(c)**. Followed by pulse-*A2*, the surface reaction with reactant *B* is similar to that in pulse-*B* of conventional ABAB… type deposition. Extension of ABAB… growth model to AABAAB… type requires the modifications to **Eq. (7.6)-(7.7)**, so as to account for pulse-*A1*, pulse-*A2* and pulse-*B*:

<u>Surface reaction during pulse-A1:</u>

$$\begin{bmatrix} {}^{A1(k)}\theta^{AB,n} = {}^{B(k-1)}\theta^{AB,n} \\ {}^{A1(k)}\theta^{A-L,n} = {}^{B(k-1)}\theta^{A-L,n} + \left({}^{B(k-1)}\theta^{B-X,n} / m_{A-X}\right)\cdot\left(1-\exp(-C^{A-L}_{B-X,1}\cdot t_A)\right) \\ {}^{A1(k)}\theta^{B-X,n} = {}^{B(k-1)}\theta^{B-X,n} - \left({}^{B(k-1)}\theta^{B-X,n} / m_{A-X}\right)\cdot\left(1-\exp(-C^{A-L}_{B-X,1}\cdot t_A)\right) \\ \vdots \\ {}^{A1(k)}\theta^{AB,n+(m-1)} = {}^{B(k-1)}\theta^{AB,n+(m-1)} \\ {}^{A1(k)}\theta^{A-L,n+(m-1)} = {}^{B(k-1)}\theta^{A-L,n+(m-1)} + \left({}^{B(k-1)}\theta^{B-X,n+(m-1)} / m_{A-X}\right)\cdot\left(1-\exp(-C^{A-L}_{B-X,\mathrm{m}}\cdot t_A)\right) \\ {}^{A1(k)}\theta^{B-X,n+(m-1)} = {}^{B(k-1)}\theta^{B-X,n+(m-1)} - \left({}^{B(k-1)}\theta^{B-X,n+(m-1)} / m_{A-X}\right)\cdot\left(1-\exp(-C^{A-L}_{B-X,m}\cdot t_A)\right) \\ {}^{A1(k)}\theta^{B-X,n+m} = {}^{B(k-1)}\theta^{B-X,n+m} \end{bmatrix} \quad \textbf{(7.8)}$$

Surface reaction during pulse-A2:

$$\left[\begin{aligned}
{}^{A2(k)}\theta^{AB,n} &= {}^{A1(k)}\theta^{AB,n} \\
{}^{A2(k)}\theta^{A-L,n} &= {}^{A1(k)}\theta^{A-L,n} + \left({}^{A1(k)}\theta^{B-X,n} \big/ m_{A-X}\right)\cdot(1-\exp(-C^{A-L}_{B-X,1}\cdot t_A)) \\
{}^{A2(k)}\theta^{B-X,n} &= {}^{A1(k)}\theta^{B-X,n} - \left({}^{A1(k)}\theta^{B-X,n} \big/ m_{A-X}\right)\cdot(1-\exp(-C^{A-L}_{B-X,1}\cdot t_A)) \\
&\vdots \\
{}^{A2(k)}\theta^{AB,n+(m-1)} &= {}^{A1(k)}\theta^{AB,n+(m-1)} \\
{}^{A2(k)}\theta^{A-L,n+(m-1)} &= {}^{A1(k)}\theta^{A-L,n+(m-1)} + \left({}^{A1(k)}\theta^{B-X,n+(m-1)} \big/ m_{A-X}\right)\cdot(1-\exp(-C^{A-L}_{B-X,\mathrm{m}}\cdot t_A)) \\
{}^{A2(k)}\theta^{B-X,n+(m-1)} &= {}^{A1(k)}\theta^{B-X,n+(m-1)} - \left({}^{A1(k)}\theta^{B-X,n+(m-1)} \big/ m_{A-X}\right)\cdot(1-\exp(-C^{A-L}_{B-X,m}\cdot t_A)) \\
{}^{A2(k)}\theta^{B-X,n+m} &= {}^{A1(k)}\theta^{B-X,n+m}
\end{aligned}\right] \qquad \mathbf{(7.9)}$$

Surface reaction during pulse-B:

$$\left[\begin{aligned}
{}^{B(k)}\theta^{AB,n} &= {}^{A2(k)}\theta^{AB,n} + \left({}^{A2(k)}\theta^{A-L,n} \big/ m_{B-X}\right)\cdot(1-\exp(-C^{B-X}_{A-L,1}\cdot t_B)) \\
{}^{B(k)}\theta^{A-L,n} &= {}^{A2(k)}\theta^{A-L,n} - \left({}^{A2(k)}\theta^{A-L,n} \big/ m_{B-X}\right)\cdot(1-\exp(-C^{B-X}_{A-L,1}\cdot t_B)) \\
{}^{B(k)}\theta^{B-X,n+1} &= {}^{A2(k)}\theta^{B-X,n+1} + \left({}^{A2(k)}\theta^{A-L,n+1} \big/ m_{B-X}\right)\cdot(1-\exp(-C^{B-X}_{A-L,1}\cdot t_B)) \\
&\vdots \\
{}^{B(k)}\theta^{AB,n+(m-1)} &= {}^{A2(k)}\theta^{AB,n+(m-1)} + \left({}^{A2(k)}\theta^{A-L,n+(m-1)} \big/ m_{B-X}\right)\cdot(1-\exp(-C^{B-X}_{A-L,m}\cdot t_B)) \\
{}^{B(k)}\theta^{A-L,n+(m-1)} &= {}^{A2(k)}\theta^{A-L,n+(m-1)} - \left({}^{A2(k)}\theta^{A-L,n+(m-1)} \big/ m_{B-X}\right)\cdot(1-\exp(-C^{B-X}_{A-L,m}\cdot t_B)) \\
{}^{B(k)}\theta^{B-X,n+\mathrm{m}} &= {}^{A2(k)}\theta^{B-X,n+m} + \left({}^{A2(k)}\theta^{A-L,n+m} \big/ m_{B-X}\right)\cdot(1-\exp(-C^{B-X}_{A-L,m}\cdot t_B)) \\
{}^{B(k)}\theta^{B-X,n} &= {}^{A2(k)}\theta^{B-X,n}
\end{aligned}\right] \qquad \mathbf{(7.10)}$$

Figure 7-4 shows the theoretical film thickness with AABAAB… type ALD, from the solution to **Eq. (7.8) - (7.10)**, with pulse-A1, pulse-A2 and pulse-B kept at 0.5s, 0.5s, and 9s. Surface reactions were modelled so as to allow up to 3 partial monolayers formation for steric factor $m_{A-L} = 4$, keeping other growth parameters the same as calculations shown in **Figure 7-2**. To compare AABAAB… growth with conventional ALD, theoretical film thickness for ABAB… growth with precursor pulse of 1s (equivalent to 2 pulses of 0.5s) is also presented.

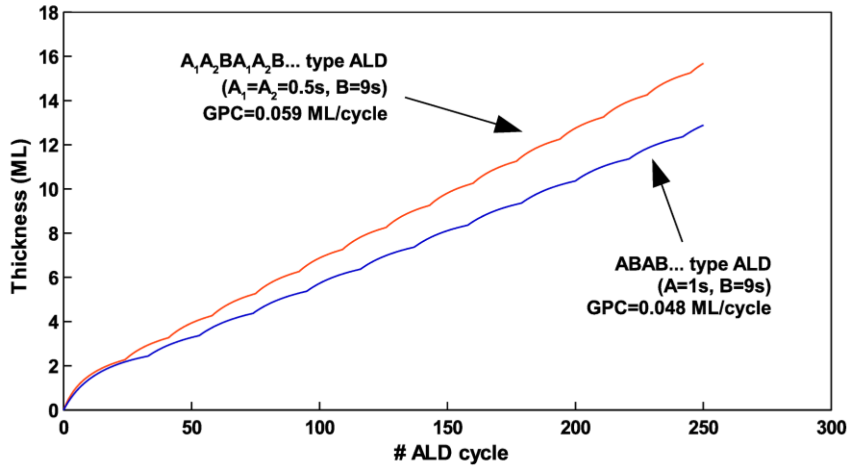

Figure 7-4: Modeled ALD film thickness for AABAAB… (A_1 = 0.5s, A_2 = 0.5s, B = 9s) and ABAB… (A = 1s and B = 9s) type deposition with precursor steric factor m_{A-L}= 4.0. For equivalent precursor dose the calculated GPC of 0.059 ML/cycle with AABAAB… ALD as compared to GPC of 0.048 ML/cycle with ABAB… ALD shows better precursor utilization for proposed AABAAB… cycle.

The theoretical GPC values for AABAAB… and ABAB… type growth at different values of precursor steric hindrance factors (m_{A-L}) are tabulated in Table 7-1. In the absence of any steric effects (i.e. m_{A-L} = 1) both type of ALD results in similar film growth with GPC of 0.286 ML/cycle. However when steric effects are significant (i.e. m_{A-L} > 1), the AABAAB… deposition resulted in higher GPC as compared to ABAB… deposition, for the equivalent exposure of ALD precursor.

Table 7-1: Theoretical GPC for AABAAB… growth and ABAB… growth for total precursor dose of 1s and reactant pulse of 9s, with precursor steric factor m_{A-L} = 1.0, 1.5, 2.0 and 4.0

m_{A-L}	GPC (ML/cycle)	
	AABAAB… growth	**ABAB… growth**
4.0	0.059	0.048
2.0	0.125	0.103
1.5	0.167	0.143
1.0	0.286	0.286

The self-limiting growth for AABAAB… type ALD with respect to total precursor dose ($dose_{A1} = dose_{A2} = 0.5*dose_{total}$) is shown in **Figure 7-5(a)-(d)**,

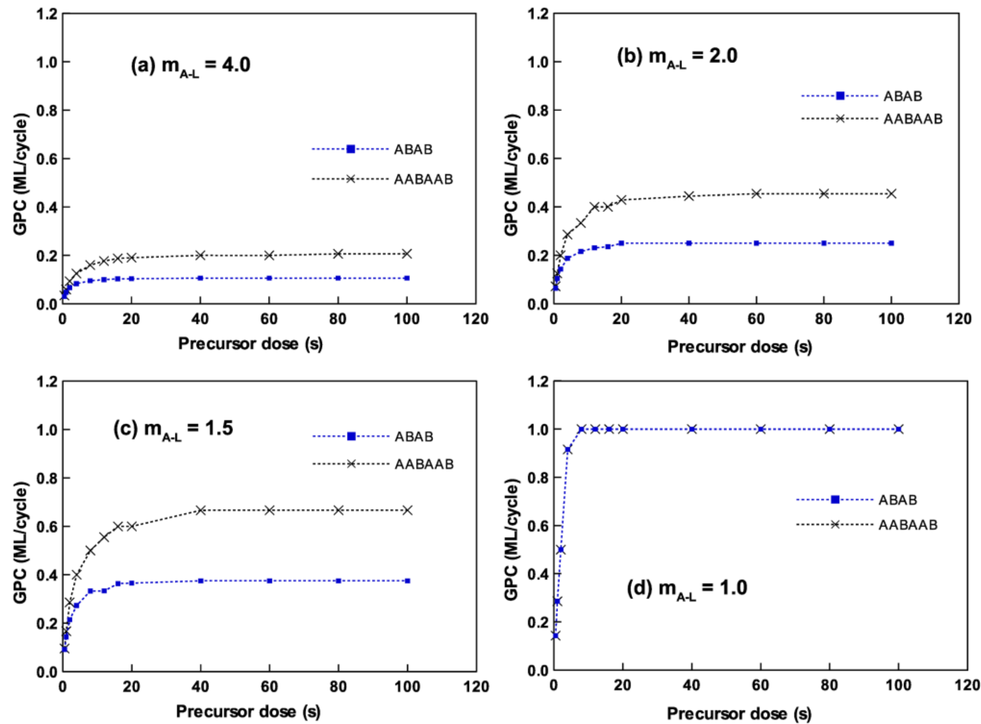

Figure 7-5: Simulated ALD saturation curves with respect to precursor dose for AABAAB and ABAB type deposition at (a) m_{A-L}=4.0; (b) m_{A-L}=2.0; (c) m_{A-L}=1.5; and (d) m_{A-L}=1.0. The modeled GPC is obtained at equivalent precursor dose for AABAAB type deposition ($dose_{A1} = dose_{A2} = 0.5*dose_{total}$) and ABAB type deposition ($dose_{A} = dose_{total}$).

for variable precursor steric factors (m_{A-L}). For comparison, saturation curves with respect to precursor dosing for conventional ABAB… type ALD ($dose_A = dose_{total}$) are also shown.

In case when precursor molecules exhibit steric hindrance (i.e. $m_{A-L}>1$), only a fraction ($1/m_{A-L}$) of the total surface active sites are consumed during precursor half reaction, and hence at saturation only partial monolayer growth is observed per cycle as shown in **Figure 7-5(a)-(c)**. In the ideal case when steric hindrance from precursor molecules are negligible, (i.e. $m_{A-L}=1$), every deposition cycle under saturation conditions would result in a complete

monolayer deposition **Figure 7-5(d)**. The higher GPC at saturation with AABAAB than with ABAB type deposition for an equivalent precursor dose in presence of steric hindrance demonstrates precursor utilization with the proposed ALD recipe.

7.4. Results and discussion

To experimentally verify simulation results shown in **Figure 7-5**, experimental saturation curves were determined for ZrN PEALD growth with modified AABAAB… and the conventional ABAB… type deposition. These films were deposited on Si (111) substrates at 150 °C with a variable TDMAZr precursor dose, 12s of post-TDMAZr purge, 9s forming gas plasma, and 9s of post-plasma purge. Except for the ALD valves temperature set to 90 °C, rest all temperature set points were identical to those reported in Chapter 5. To ensure identical dosage of TDMAZr molecules is used, the precursor pulses at step A_1 and A_2 of AABAAB were kept at half times the pulse at step A of ABAB deposition.

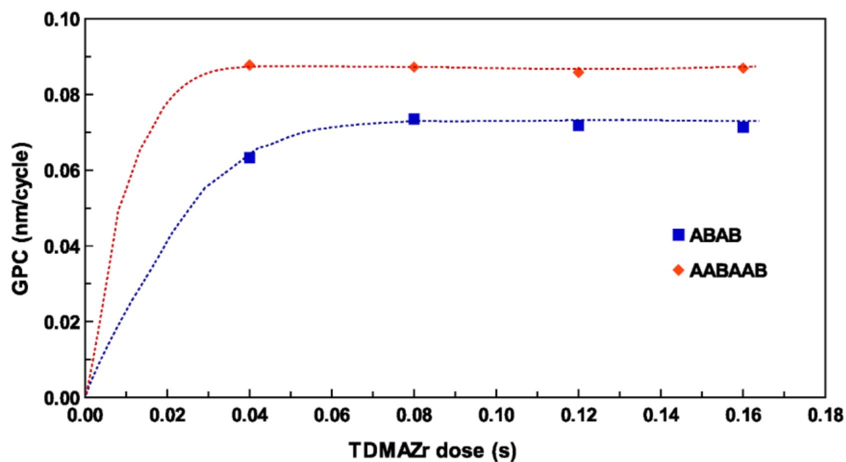

Figure 7-6: ALD saturations curves obtained for ZrN deposition using ABAB and AABAAB type deposition.

As shown in **Figure 7-6** the GPC values at saturation condition for ZrN deposition were found as 0.087±0.001 nm/cycle for AABAAB… recipe and 0.072±0.001 nm/cycle for ABAB… type recipe. Also in the range of TDMAZr pulse lengths under investigation, the self-limiting ZrN growth was obtained at minimum precursor pulse of 0.08 ms for ABAB type deposition, whereas for AABAAB type deposition surface saturation was observed at total precursor pulse of 0.04 s (pulse A_1 = 0.02 s and pulse A_2 = 0.02 s). These results are in agreement with the numerical data shown in **Figure 7-5**, and demonstrates that with the modified ALD cycle, not only is the GPC at saturation higher but also saturation condition is attained with much shorter TDMAZr dose as compared to the conventional ALD.

7.5. Conclusions

A first-principle numerical model for ALD growth is developed for deposition of a binary material (*AB*) using precursor ($A\text{-}L_n$) and reactant ($B\text{-}X_n$). The effects of precursor steric hindrance are included in the model as parameter ($1/m_{A\text{-}L}$) that represents the ratio of surface sites participating in surface reaction to the total number of available surface sites. A modification (AABAAB…) to the conventional (ABAB…) type ALD cycle is investigated and modeled since the volume of adsorbed precursor molecules undergoes reduction on reacting at the surface. The theoretical calculations based upon the presented ALD growth model showed that for the equivalent precursor dose, GPC at saturation is higher with AABAAB… cycle than ABAB… cycle. The experimental saturation curves for ZrN PEALD are in agreement with the calculated data and shows ~20% increase in the GPC at saturation

(0.087±0.001 nm/cycle with AABAAB… as compared to 0.072±0.001 nm/cycle with ABAB…). Also the surface saturation was obtained at the minimum total TDMAZr dose of 0.04 s with AABAAB cycle as compared to 0.08 s for ABAB cycle. Although this chapter demonstrates higher precursor utilization only for AAB… cycle, this approach is not limited to $(A)_2(B)_1$… but could be extended to a generalized $(A)_m(B)_n$… cycle. Although ALD on flat substrate was tested, but similar improvements are expected for deposition within high aspect ratio features.

7.6. References

[1] J. Robertson, Rep. Prog. Phys. 69 (2006) 327.

[2] H. Kim, H.-B.-R. Lee, W.-J. Maeng, Thin Solid Films 517 (2009) 2563.

[3] S.M. George, Chem. Rev. 110 (2010) 111.

[4] S.M. George, A.W. Ott, J.W. Klaus, J. Phys. Chem. 100 (1996) 13121.

[5] R.L. Puurunen, J. Appl. Phys. 97 (2005) 121301.

[6] V. Miikkulainen, M. Leskelä, M. Ritala, R.L. Puurunen, J. Appl. Phys. 113 (2013) 021301.

[7] H. Kim, Thin Solid Films 519 (2011) 6639.

[8] H.B. Profijt, S.E. Potts, M.C.M. van de Sanden, W.M.M. Kessels, J. Vac. Sci. Technol. Vac. Surf. Films 29 (2011) 050801.

[9] R.L. Puurunen, Chem. Vap. Depos. 9 (2003) 249.

[10] M.A. Alam, M.L. Green, J. Appl. Phys. 94 (2003) 3403.

[11] C.D. Travis, R.A. Adomaitis, Theor. Chem. Acc. 133 (2014).

[12] R.L. Puurunen, W. Vandervorst, J. Appl. Phys. 96 (2004) 7686.

[13] R.L. Puurunen, Chem. Vap. Depos. 10 (2004) 159.

[14] J. Evans, Phys. Rev. B 39 (1989) 5655.

[15] H.-S. Park, J.-S. Min, J.-W. Lim, S.-W. Kang, Appl. Surf. Sci. 158 (2000) 81.

[16] J.-W. Lim, J.-S. Park, S.-W. Kang, J. Appl. Phys. 87 (2000) 4632.

[17] J.-W. Lim, H.-S. Park, S.-W. Kang, J. Appl. Phys. 88 (2000) 6327.

[18] J.-W. Lim, H.-S. Park, S.-W. Kang, J. Electrochem. Soc. 148 (2001) C403.

8. Conclusions and Contributions to Knowledge

8.1. Conclusions

- ZrN PEALD dynamic *iSE* (*d-iSE*) data during growth was interpreted and modeled, and it was shown that for surface diffusion enhanced film growth, a partial surface monolayer growth of ZrN PEALD film formed at the end of every deposition cycle.
- Design of experiments based on self-limiting ALD surface reactions were used to optimize deposition cycle for ZrN PEALD films.
- Conducting ZrN PEALD films (resistivity of 559.5 μΩ-cm) were deposited at 150 °C substrate temperature using TDMAZr precursor and forming gas (5% H_2) reactant plasma without post-deposition annealing. Electrical resistivity of our ZrN films is compared with that of other PEALD grown transition metal nitrides in **Table 8-1**.
- The optical emission spectrum from ICP plasma did not support the formation of SiO species from the interaction between plasma and plasma confining quartz tube. Also the absence of Si 2p core-level emission in depth-profile XPS spectra from ZrN PEALD films suggested that incorporation of SiO species could not have been the source of O-contamination.
- O 1s emission in depth-profile XPS spectra was associated to the Ar ion sputtering induced diffusion/relocation of ZrN surface oxide into the underlying film during depth-profiling.

- The numerical ALD growth model showed that the AABAAB… type deposition cycle would result in higher GPC at saturation as compared with the conventional ABAB… type cycle, for equivalent dose of precursor *A*, other deposition parameters remaining identical.
- ZrN PEALD growth experiments with AABAAB… deposition cycle demonstrated an simultaneous ~20% increase in the GPC and 50% reduction in the minimum TDMAZr dose necessary for saturation as compared to conventional ABAB… cycle.

Table 8-1: Electrical resistivity (ρ) of PEALD grown transition metal nitrides on SiO_2.

Material	Precursor/Reactant	$T_{Substrate}$ (°C)	ρ (μΩ-cm)
HfN	TEMAHf/H_2 plasma [1]	250	2327
TaN	TBTDETa/H_2 plasma [2]	260	400
	PDMATa/ H_2 plasma [3]	225	380[a]
TiN	$TiCl_4$/(88% H_2 – N_2) plasma [3]	350	150[a]
	TDMATi/H_2 plasma [4]	150	210-275
	TDMATi/NH_3 plasma [5]	200	180
ZrN	TDEAZr/N_2 plasma [6]	300	400[a]
	TDMAZr/(5% H_2 – N_2) plasma	**150**	**559.6***

TEMAHf : tetrakis-(ethyl-methyl-amino)-hafnium

TBTDETa : ter-(butyl-imido)-tris-(diethyl-amido)-tantalum

PDMATa : pentakis-dimethyl-amino-tantalum

$TiCl_4$: titanium tetrachloride

TDMATi : tetrakis-diethyl-amino-titanium

TDEAZr : tetrakis-ethyl-methyl-amino-titanium

TDMAZr : tetrakis-diethyl-amino-zirconium

[a] Resistivity measured for films directly deposited on Si substrate.

* With further optimization of deposition process the electrical resistivity of PEALD ZrN films is expected to reduce below the reported value in this work

8.2. Contributions to knowledge

- Interpretation and analysis of *d-iSE* data has been presented, demonstrating its application to the study of ALD in the early stages of growth.
- An experimental design scheme has been presented for optimization of the ALD cycle parameters from reduced number of experiments.
- The investigation of O-contamination in ZrN PEALD films have shown that source of this contamination was not related to the conventional ICP plasma source against the claims promoting application of alternate plasma source for PEALD.
- With AABAAB… type deposition cycle, as example it was shown that the efficiency of precursor utilization in ALD could be improved with novel ALD recipes of type $(A)_m(B)_n(A)_m(B)_n$…

8.3. References

[1] S. Consiglio, W. Zeng, N. Berliner, E.T. Eisenbraun, J. Electrochem. Soc. 155 (2008) H196.

[2] J.-S. Park, H.-S. Park, S.-W. Kang, J. Electrochem. Soc. 149 (2002) C28.

[3] H.C.M. Knoops, L. Baggetto, E. Langereis, M.C.M. van de Sanden, J.H. Klootwijk, F. Roozeboom, R.A.H. Niessen, P.H.L. Notten, W.M.M. Kessels, J. Electrochem. Soc. 155 (2008) G287.

[4] P. Caubet, T. Blomberg, R. Benaboud, C. Wyon, E. Blanquet, J.-P. Gonchond, M. Juhel, P. Bouvet, M. Gros-Jean, J. Michailos, C. Richard, B. Iteprat, J. Electrochem. Soc. 155 (2008) H625.

[5] J. Musschoot, Q. Xie, D. Deduytsche, S. Van den Berghe, R.L. Van Meirhaeghe, C. Detavernier, Microelectron. Eng. 86 (2009) 72.

[6] S. Cho, K. Lee, P. Song, H. Jeon, Y. Kim, Jpn. J. Appl. Phys. 46 (2007) 4085

9. Future Directions

The key-results presented in this thesis would serve as a guide for future research directions into the development of nitride ALD in specific and ALD fundamentals in general.

The *d-iSE* data analysis procedure demonstrated for ZrN PEALD growth will be applied to study different modes of ALD growth. The design of experiment presented for ZrN PEALD optimization would be adapted for other ALD process for faster process optimization.

The electrical resistivity data for ZrN PEALD films using forming gas plasma with 5% H_2 plasma was found to be comparable with nitride PEALD processes using H-rich reactant gases. Hence the role of H content in reactant plasma gas requires further study. The development of PEALD recipe for selective deposition of mononitride (ZrN) or nitrogen-rich (Zr_3N_4) phase with control over impurity concentration would be beneficial to several technologically advanced applications.

It is essential to develop Ar sputtering recipes for depth-profile characterization of PEALD films with minimum distortion in the actual concentration profile. The precursor utilization efficiency with novel ALD recipes ($A_mB_nA_mB_n$… type cycle) are required to be evaluated for deposition within high-aspect ratio features.

Bibliography

Aaltonen, T., Ritala, M., Leskelä, M., 2005. Electrochem. Solid-State Lett. 8, C99.

Aarik, J., Mändar, H., Kirm, M., Pung, L., 2004. Thin Solid Films 466, 41–47.

Adachi, J., Kurosaki, K., Uno, M., Yamanaka, S., 2005a. J. Alloys Compd. 396, 260–263.

Adachi, J., Kurosaki, K., Uno, M., Yamanaka, S., 2005b. J. Alloys Compd. 399, 242–244.

A. Kramida, Yu. Ralchenko, J. Reader, and NIST ASD Team, 2013. NIST Atomic Spectra Database.

Alam, M.A., Green, M.L., 2003. J. Appl. Phys. 94, 3403.

Andersson, K., Veszelei, M., Roos, A., 1994. Sol. Energy Mater. Sol. Cells 32, 199–212.

An, I., Li, Y.M., Nguyen, H.V., Collins, R.W., 1992. Rev. Sci. Instrum. 63, 3842.

Antson, J., Suntola, T., 1977. Method for producing compound thin films. 4,058,430.

Archer, R.J., 1962. J. Opt. Soc. Am. 52, 970.

Archer, R.J., Gobeli, G.W., 1965. J. Phys. Chem. Solids 26, 343–351.

Arwin, H., Aspnes, D.E., 1984. Thin Solid Films 113, 101–113.

Aspnes, D.E., 1980. J. Electrochem. Soc. 127, 1359.

Aspnes, D.E., Quinn, W.E., Tamargo, M.C., Pudensi, M.A.A., Schwarz, S.A., Brasil, M.J.S.P., Nahory, R.E., Gregory, S., 1992. Appl. Phys. Lett. 60, 1244.

Aspnes, D., Theeten, J., Hottier, F., 1979. Phys. Rev. B 20, 3292–3302.

Bae, C., Krug, C., Lucovsky, G., Chakraborty, A., Mishra, U., 2004. Appl. Phys. Lett. 84, 5413.

Barnett, S.A., Hultman, L., Sundgren, J.-E., Ronin, F., Rohde, S., 1988. Appl. Phys. Lett. 53, 400.

Barton, D., Urban, F.K., 2007. Thin Solid Films 516, 119–127.

Bazhanov, D.I., Knizhnik, A.A., Safonov, A.A., Bagatur'yants, A.A., Stoker, M.W., Korkin, A.A., 2005. J. Appl. Phys. 97, 044108.

Becker, J.S., Kim, E., Gordon, R.G., 2004. Chem. Mater. 16, 3497–3501.

Benia, H.., Guemmaz, M., Schmerber, G., Mosser, A., Parlebas, J.-C., 2002. Appl. Surf. Sci. 200, 231–238.

Björck, M., Andersson, G., 2007. J. Appl. Crystallogr. 40, 1174–1178.

Bolat, S., Ozgit-Akgun, C., Tekcan, B., Biyikli, N., Okyay, A.K., 2014. Appl. Phys. Lett. 104, 243505.

Bootsma, G.A., Meyer, F., 1969. Surf. Sci. 14, 52–76.

Bothe, K., Ma, A., Voon, K., Barlage, D., Afshar, A., Motamedi, P., Muneshwar, T., Cadien, K., Polar Source Gallium Nitride MOSFET Structures and Methods of Fabrication. US Provisional patent 61/967,239

Braic, V., Balaceanu, M., Braic, M., 2008. Grazing incidence mirrors for EUV lithography. IEEE, pp. 267–270.

Burton, B.B., Lavoie, A.R., George, S.M., 2008. J. Electrochem. Soc. 155, D508.

Butcher, K.S.A., Afifuddin, Chen, P.P.-T., Tansley, T.L., 2003. Phys. Status Solidi C 0, 156–160.

Camacho, J.J., Díaz, L., Santos, M., Reyman, D., Poyato, J.M.L., 2008. J. Phys. Appl. Phys. 41, 105201.

Carvalho, P., Chappé, J.M., Cunha, L., Lanceros-Méndez, S., Alpuim, P., Vaz, F., Alves, E., Rousselot, C., Espinós, J.P., González-Elipe, A.R., 2008. J. Appl. Phys. 103, 104907.

Caubet, P., Blomberg, T., Benaboud, R., Wyon, C., Blanquet, E., Gonchond, J.-P., Juhel, M., Bouvet, P., Gros-Jean, M., Michailos, J., Richard, C., Iteprat, B., 2008. J. Electrochem. Soc. 155, H625.

Chen, C.-S., Liu, C.-P., Yang, H.-G., Tsao, C.Y.A., 2004. J. Vac. Sci. Technol. B Microelectron. Nanometer Struct. 22, 1075.

Chhowalla, M., Unalan, H.E., 2005. Nat. Mater. 4, 317–322.

Chihi, T., Fatmi, M., Ghebouli, B., Guemmaz, M., 2011. Solid State Sci. 13, 1414–1419.

Ching, W., Xu, Y.-N., Ouyang, L., 2002. Phys. Rev. B 66.

Cho, S., Lee, K., Song, P., Jeon, H., Kim, Y., 2007. Jpn. J. Appl. Phys. 46, 4085–4088.

Coburn, J.W., 1976. J. Vac. Sci. Technol. 13, 1037.

Cohen, P.I., Petrich, G.S., Pukite, P.R., Whaley, G.J., Arrott, A.S., 1989. Surf. Sci. 216, 222–248.

Collins, R.W., 1990. Rev. Sci. Instrum. 61, 2029.

Consiglio, S., Zeng, W., Berliner, N., Eisenbraun, E.T., 2008. J. Electrochem. Soc. 155, H196.

Daillant, J., Gibaud, A. (Eds.), 1999. X-ray and neutron reflectivity: principles and applications, Lecture notes in physics. Monographs. Springer, New York.

Davis, W.R., Wilson, J., Mick, S., Jian Xu, Hao Hua, Mineo, C., Sule, A.M., Steer, M., Franzon, P.D., 2005. IEEE Des. Test Comput. 22, 498–510.

Dignam, M.J., Moskovits, M., 1973. J. Chem. Soc. Faraday Trans. 2 69, 56.

DongHo, K., ChulMin, K., EunHong, K., YoungChul, S., TaeGeun, K., CheongHyun, R., Cheol-Koo, H., 2009. J. Korean Phys. Soc. 55, 1149.

Drude, P., 1889a. Ann Phys Chem N. F. 36, 532–560.

Drude, P., 1889b. Ann Phys Chem N. F. 36, 865–897.

Drude, P., 1890. Ann Phys Chem N. F. 39, 481–554.

Egeland, G.W., Wheeler, K., Peralta, P., McClellan, K.J., Maloy, S.A., Bond, G.M., 2011. J. Nucl. Mater. 416, 253–261.

Eisenbraun, E., van der Straten, O., Yu Zhu, Dovidenko, K., Kaloyeros, A., 2001. Atomic layer deposition (ALD) of tantalum-based materials for zero thickness copper barrier applications. IEEE, pp. 207–209.

Elam, J.., Nelson, C.., Grubbs, R.., George, S.., 2001. Surf. Sci. 479, 121–135.

Elliott, S.D., 2007. Models for ALD and MOCVD Growthof Rare Earth Oxides, in: Fanciulli, M., Scarel, G. (Eds.), Rare Earth Oxide Thin Films, Topics in Applied Physics. Springer Berlin Heidelberg, pp. 73–86.

Evans, J., 1989. Phys. Rev. B 39, 5655–5664.

Fang, Z., Williams, P.A., Odedra, R., Jeon, H., Potter, R.J., 2012. J. Cryst. Growth 338, 111–117.

Farkas, N., Zhang, G., Evans, E.A., Ramsier, R.D., Dagata, J.A., 2003. J. Vac. Sci. Technol. Vac. Surf. Films 21, 1188.

Farkas, N., Zhang, G., Ramsier, R.D., Evans, E.A., Dagata, J.A., 2008. J. Vac. Sci. Technol. Vac. Surf. Films 26, 297.

Farmer, J.C., 1985. J. Electrochem. Soc. 132, 313.

Fierro, A., Laity, G., Neuber, A., 2012. J. Phys. Appl. Phys. 45, 495202.

Fix, R., Gordon, R.G., Hoffman, D.M., 1991. Chem. Mater. 3, 1138–1148.

Fragiel, A., Staia, M.H., Muñoz-Saldaña, J., Puchi-Cabrera, E.S., Cortes-Escobedo, C., Cota, L., 2008. Surf. Coat. Technol. 202, 3653–3660.

Fujiwara, H., 2007. Spectroscopic Ellipsometry: Principles and Applications. Wiley, West Sussex, UK.

Fujiwara, H., Koh, J., Rovira, P., Collins, R., 2000. Phys. Rev. B 61, 10832–10844.

Galdikas, A., 1999. Vacuum 55, 51–58.

Gaydon, A.G., 2013. Identification of molecular spectra. Springer, [S.l.].

George, S.M., 2010. Chem. Rev. 110, 111–131.

George, S.M., Ott, A.W., Klaus, J.W., 1996. J. Phys. Chem. 100, 13121–13131.

Gilliot, M., 2012. Thin Solid Films 520, 5568–5574.

Goldenberg, E., Ozgit-Akgun, C., Biyikli, N., Kemal Okyay, A., 2014. J. Vac. Sci. Technol. Vac. Surf. Films 32, 031508.

Gordon, R.G., Hausmann, D., Kim, E., Shepard, J., 2003. Chem. Vap. Depos. 9, 73–78.

Gotoh, Y., Tsuji, H., Ishikawa, J., 2003. J. Vac. Sci. Technol. B Microelectron. Nanometer Struct. 21, 1607.

Gribaudo, L., Arias, D., Abriata, J., 1994. J. Phase Equilibria 15, 441–449.

Groner, M.D., Elam, J.W., Fabreguette, F.H., George, S.M., 2002. Thin Solid Films 413, 186–197.

Gruss, K.., Davis, R.., 1999. Surf. Coat. Technol. 114, 156–168.

Guo, Q.-X., Kwan, W.-K., Cheng, X.-L., Zhang, H., 2010. Phys. Status Solidi B 247, 67–71.

Habraken, F.H.P.M., Gijzeman, O.L.J., Bootsma, G.A., 1980. Surf. Sci. 96, 482–507.

Håkansson, K., Johansson, H., Johansson, L., 1993. Phys. Rev. B 48, 2623–2626.

Hanekamp, L.J., Brader, S.J.H., Bootsma, G.A., 1983. Surf. Sci. 135, 383–395.

Harilal, S.S., Issac, R.C., Bindhu, C.V., Gopinath, P., Nampoori, V.P.N., Vallabhan, C.P.G., 1997. Spectrochim. Acta. A. Mol. Biomol. Spectrosc. 53, 1527–1536.

Hasan, P., Potts, S.E., Carmalt, C.J., Palgrave, R.G., Davies, H.O., 2008. Polyhedron 27, 1041–1046.

Hase, I., Nishihara, Y., 1999. Phys. Rev. B 60, 1573–1581.

Hausmann, D.M., Kim, E., Becker, J., Gordon, R.G., 2002. Chem. Mater. 14, 4350–4358.

Henn-Lecordier, L., Lei, W., Anderle, M., Rubloff, G.W., 2007. J. Vac. Sci. Technol. B Microelectron. Nanometer Struct. 25, 130.

Herzinger, C.M., Johs, B., McGahan, W.A., Woollam, J.A., Paulson, W., 1998. J. Appl. Phys. 83, 3323.

Hoffman, D.M., 1994. Polyhedron 13, 1169–1179.

Hofmann, S., 1992. J. Vac. Sci. Technol. B Microelectron. Nanometer Struct. 10, 316.

Hofmann, S., 1998. Rep. Prog. Phys. 61, 827–888.

Horita, S., 1993. J. Vac. Sci. Technol. Vac. Surf. Films 11, 2452.

Horita, S., Toda, T., Kasagawa, H., 2003. J. Korean Phys. Soc. 42, 1142–1145.

Huang, M.L., Chang, Y.C., Chang, C.H., Lee, Y.J., Chang, P., Kwo, J., Wu, T.B., Hong, M., 2005. Appl. Phys. Lett. 87, 252104.

Ihara, H., Hirabayashi, M., Nakagawa, H., 1976. Phys. Rev. B 14, 1707–1714.

International Technology Roadmap for Semiconductors, 2012.

Ivanovskii, A.L., Medvedeva, N.I., Okatov, S.V., 2001. Inorg. Mater. 37, 459–465.

Jamroz, P., Zyrnicki, W., 2006. Surf. Coat. Technol. 201, 1444–1453.

Johansson, B.O., Hentzell, H.T.G., Harper, J.M.E., Cuomo, J.J., 2011. J. Mater. Res. 1, 442–451.

Johs, B., Doerr, D., Pittal, S., Bhat, I.B., Dakshinamurthy, S., 1993. Thin Solid Films 233, 293–296.

Kafizas, A., Carmalt, C.J., Parkin, I.P., 2013. Coord. Chem. Rev. 257, 2073–2119.

Kaloyeros, A.E., Eisenbraun, E., 2000. Annu. Rev. Mater. Sci. 30, 363–385.

Kang, S.J., Donnelly, V.M., 2007. Plasma Sources Sci. Technol. 16, 265–272.

Kim, E.-J., Kim, D.-H., 2006. Electrochem. Solid-State Lett. 9, C123.

Kim, H., 2003. J. Vac. Sci. Technol. B Microelectron. Nanometer Struct. 21, 2231.

Kim, H., 2011. Thin Solid Films 519, 6639–6644.

Kim, H., Cabral, C., Lavoie, C., Rossnagel, S.M., 2002. J. Vac. Sci. Technol. B Microelectron. Nanometer Struct. 20, 1321.

Kim, H., Kellock, A.J., Rossnagel, S.M., 2002. J. Appl. Phys. 92, 7080.

Kim, H., Lee, H.-B.-R., Maeng, W.-J., 2009. Thin Solid Films 517, 2563–2580.

Kim, I.-W., Kim, S.-J., Kim, D.-H., Woo, H., Park, M.-Y., Rhee, S.-W., 2004. Korean J. Chem. Eng. 21, 1256–1259.

Kim, J.B., Kwon, D.R., Chakrabarti, K., Lee, C., Oh, K.Y., Lee, J.H., 2002. J. Appl. Phys. 92, 6739.

Kim, J., Kim, S., Jeon, H., Cho, M.-H., Chung, K.-B., Bae, C., 2005a. Appl. Phys. Lett. 87, 053108.

Kim, J., Kim, S., Kang, H., Choi, J., Jeon, H., Cho, M., Chung, K., Back, S., Yoo, K., Bae, C., 2005b. J. Appl. Phys. 98, 094504.

Kim, K.-H., Kwak, N.-W., Lee, S.H., 2009. Electron. Mater. Lett. 5, 83–86.

Kim, S.-H., Kim, J.-K., Lee, J.H., Kwak, N., Kim, J., Jung, S.-H., Hong, M.-R., Lee, S.H., Collins, J., Sohn, H., 2007. J. Electrochem. Soc. 154, D435.

Kim, S.-W., Kwon, S.-H., Jeong, S.-J., Park, J.-S., Kang, S.-W., 2008. Electrochem. Solid-State Lett. 11, H303.

Kim, T.-H., Eom, T.-K., Kim, S.-H., Kang, D.-H., Kim, H., Yu, S., Lim, J.M., 2011. Electrochem. Solid-State Lett. 14, D89.

Kim, Y., Koo, J., Han, J., Choi, S., Jeon, H., Park, C.-G., 2002. J. Appl. Phys. 92, 5443.

Kim, Y.-T., Collins, R.W., Vedam, K., 1990. Surf. Sci. 233, 341–350.

Knapas, K., Ritala, M., 2013. Crit. Rev. Solid State Mater. Sci. 38, 167–202.

Knoops, H.C.M., Baggetto, L., Langereis, E., van de Sanden, M.C.M., Klootwijk, J.H., Roozeboom, F., Niessen, R.A.H., Notten, P.H.L., Kessels, W.M.M., 2008. J. Electrochem. Soc. 155, G287.

Komiyama, H., Shimogaki, Y., Egashira, Y., 1999. Chem. Eng. Sci. 54, 1941–1957.

Kovalenko, S.A., Lisitsa, M. p., 2001. Semicond. Phys. Quantum Electron. Optoelectron. 4, 352–357.

Kramida, A.E., Ralchenko, Y., Reader, J., Team, N.A.S.D. (2013), 2008. NIST Atomic Spectra Database (version 5.1). National Institute of Standards and Technology, Gaithersburg, MD.

Krusin-Elbaum, L., Wittmer, M., 1983. Thin Solid Films 107, 111–116.

Kwon, O.-K., Kwon, S.-H., Park, H.-S., Kang, S.-W., 2004. J. Electrochem. Soc. 151, C753.

Langereis, E., Heil, S.B.S., Knoops, H.C.M., Keuning, W., van de Sanden, M.C.M., Kessels, W.M.M., 2009. J. Phys. Appl. Phys. 42, 073001.

Laurikaitis, M., Burinskas, S., Dudonis, J., Milčius, D., 2008. J. Phys. Conf. Ser. 100, 082051.

Lee, Y.-K., Chung, C.-W., 2011. J. Appl. Phys. 109, 013306.

Lehmuskero, A., Kuittinen, M., Vahimaa, P., 2007. Opt. Express 15, 10744.

Lei, W., Henn-Lecordier, L., Anderle, M., Rubloff, G.W., Barozzi, M., Bersani, M., 2006. J. Vac. Sci. Technol. B Microelectron. Nanometer Struct. 24, 780.

Leskelä, M., Kemell, M., Kukli, K., Pore, V., Santala, E., Ritala, M., Lu, J., 2007. Mater. Sci. Eng. C 27, 1504–1508.

Leu, L.C., Sadik, P., Norton, D.P., McElwee-White, L., Anderson, T.J., 2008. J. Vac. Sci. Technol. B Microelectron. Nanometer Struct. 26, 1723.

Lewin, E., Gorgoi, M., Schäfers, F., Svensson, S., Jansson, U., 2009. Surf. Coat. Technol. 204, 455–462.

Liau, Z.L., 1979. J. Vac. Sci. Technol. 16, 121.

Lim, J.-W., Park, H.-S., Kang, S.-W., 2000. J. Appl. Phys. 88, 6327.

Lim, J.-W., Park, H.-S., Kang, S.-W., 2001. J. Electrochem. Soc. 148, C403.

Lim, J.-W., Park, J.-S., Kang, S.-W., 2000. J. Appl. Phys. 87, 4632.

Lim, J.W., Yun, S.J., 2004. Electrochem. Solid-State Lett. 7, F45.

Lim, J.W., Yun, S.J., Kim, H.-T., 2007. J. Electrochem. Soc. 154, G239.

Lim, J.W., Yun, S.J., Lee, J.H., 2004. Electrochem. Solid-State Lett. 7, F73.

Liu, X., Ramanathan, S., Longdergan, A., Srivastava, A., Lee, E., Seidel, T.E., Barton, J.T., Pang, D., Gordon, R.G., 2005. J. Electrochem. Soc. 152, G213.

Loualiche, S., Lucas, C., Baruch, P., Gailliard, J.P., Pfister, J.C., 1982. Phys. Status Solidi A 69, 663–676.

Lu, H.-L., Sun, L., Ding, S.-J., Xu, M., Zhang, D.W., Wang, L.-K., 2006. Appl. Phys. Lett. 89, 152910.

Maeng, W.J., Kim, H., 2006. Electrochem. Solid-State Lett. 9, G191.

Matero, R., Rahtu, A., Ritala, M., 2001. Chem. Mater. 13, 4506–4511.

Meng, W.J., 1992. J. Vac. Sci. Technol. Vac. Surf. Films 10, 1610.

Menou, N., Wang, X.P., Kaczer, B., Polspoel, W., Popovici, M., Opsomer, K., Pawlak, M.A., Knaepen, W., Detavernier, C., Blomberg, T., Pierreux, D., Swerts, J., Maes, J.W., Favia, P., Bender, H., Brijs, B., Vandervorst, W., Van Elshocht, S., Wouters, D.J., Biesemans, S., Kittl, J.A., 2008. 0.5 nm EOT low leakage ALD SrTiO3 on TiN MIM capacitors for DRAM applications, in: Electron Devices Meeting, 2008. IEDM 2008. IEEE International. IEEE, pp. 1–4.

Methaapanon, R., Geyer, S.M., Brennan, S., Bent, S.F., 2013. Chem. Mater. 25, 3458–3463.

Meyer, F., De Kluizenaar, E.E., Bootsma, G.A., 1971. Surf. Sci. 27, 88–106.

Miikkulainen, V., Leskelä, M., Ritala, M., Puurunen, R.L., 2013. J. Appl. Phys. 113, 021301.

Milošev, I., 1998. Surf. Sci. Spectra 5, 152.

Mohney, S.E., Luther, B.P., Wolter, S.D., Jackson, T.N., Karlicek, R.F., Kern, R.S., 1998. TiN and ZrN based ohmic contacts to n-GaN, in: High Temperature Electronics Conference, 1998. HITEC. 1998 Fourth International. IEEE, pp. 134–137.

Morant, C., Sanz, J., Galán, L., 1992. Phys. Rev. B 45, 1391–1398.

Moré, J.J., 1978. The Levenberg-Marquardt algorithm: Implementation and theory, in: Watson, G.A. (Ed.), Numerical Analysis, Lecture Notes in Mathematics. Springer Berlin Heidelberg, pp. 105–116.

Müller, R., 1990. Appl. Phys. Lett. 57, 1020.

Muller, R.H., Farmer, J.C., 1983. Surf. Sci. 135, 521–531.

Murthy, S.D., Bhat, I., Johs, B., Pittal, S., He, P., 1995. J. Electron. Mater. 24, 1087–1091.

Musschoot, J., Xie, Q., Deduytsche, D., Van den Berghe, S., Van Meirhaeghe, R.L., Detavernier, C., 2009. Microelectron. Eng. 86, 72–77.

Netterfield, R.P., Martin, P.J., McKenzie, D.R., 1990. J. Mater. Sci. Lett. 9, 972–974.

Niinistö, J., Rahtu, A., Putkonen, M., Ritala, M., Leskelä, M., Niinistö, L., 2005. Langmuir 21, 7321–7325.

Ohring, M., 2002. Materials science of thin films: deposition and structure, 2nd ed. ed. Academic Press, San Diego, CA.

Ozgit-Akgun, C., Donmez, I., Biyikli, N., 2013. ECS Trans. 58, 289–297.

Ozgit-Akgun, C., Goldenberg, E., Okyay, A.K., Biyikli, N., 2014. J. Mater. Chem. C 2, 2123.

Ozgit, C., Donmez, I., Alevli, M., Biyikli, N., 2012. Thin Solid Films 520, 2750–2755.

Ozgit, C., Donmez, I., Alevli, M., Biyikli, N., 2012. J. Vac. Sci. Technol. Vac. Surf. Films 30, 01A124.

Park, H.-S., Min, J.-S., Lim, J.-W., Kang, S.-W., 2000. Appl. Surf. Sci. 158, 81–91.

Park, J.-S., Park, H.-S., Kang, S.-W., 2002. J. Electrochem. Soc. 149, C28.

Park, S.-J., Kim, W.-H., Lee, H.-B.-R., Maeng, W.J., Kim, H., 2008. Microelectron. Eng. 85, 39–44.

Pichon, L., Girardeau, T., Straboni, A., Lignou, F., Guérin, P., Perrière, J., 1999. Appl. Surf. Sci. 150, 115–124.

Pierson, H.O., 1996. , in: Handbook of Refractory Carbides and Nitrides: Properties, Characteristics, Processing, and Applications. Noyes Publications, Park Ridge, N.J.

Platt, C.L., Li, N., Li, K., Klein, T.M., 2010. Thin Solid Films 518, 4081–4086.

Porte, L., 1984. Solid State Commun. 50, 303–306.

Prieto, P., 1996. J. Vac. Sci. Technol. Vac. Surf. Films 14, 3181.

Prieto, P., Fernández, A., Soriano, L., Yubero, F., Elizalde, E., González-Elipe, A., Sanz, J., 1995. Phys. Rev. B 51, 17984–17987.

Prieto, P., Galán, L., Sanz, J., 1993. Phys. Rev. B 47, 1613–1615.

Prieto, P., Galán, L., Sanz, J.M., 1994. Surf. Interface Anal. 21, 395–399.

Profijt, H.B., Kudlacek, P., van de Sanden, M.C.M., Kessels, W.M.M., 2011. J. Electrochem. Soc. 158, G88.

Puurunen, R.L., 2003. Chem. Vap. Depos. 9, 249–257.

Puurunen, R.L., 2004. Chem. Vap. Depos. 10, 159–170.

Puurunen, R.L., 2005. J. Appl. Phys. 97, 121301.

Puurunen, R.L., Vandervorst, W., 2004. J. Appl. Phys. 96, 7686.

Puurunen, R.L., Vandervorst, W., Besling, W.F.A., Richard, O., Bender, H., Conard, T., Zhao, C., Delabie, A., Caymax, M., De Gendt, S., Heyns, M., Viitanen, M.M., de Ridder, M., Brongersma, H.H., Tamminga, Y., Dao, T., de Win, T., Verheijen, M., Kaiser, M., Tuominen, M., 2004. J. Appl. Phys. 96, 4878.

Reddy, G.L.N., Ramana, J.V., Kumar, S., Kumar, S.V., Raju, V.S., 2007. Appl. Surf. Sci. 253, 7230–7237.

Ribbing, C.G., Roos, A., 1997. Zirconium Nitride (ZrN) Hafnium Nitride (HfN), in: Handbook of Optical Constants of Solids. Elsevier, pp. 351–369.

Ritala, M., 1995. J. Electrochem. Soc. 142, 2731.

Ritala, M., Niinistö, J., 2009. Chapter 4. Atomic Layer Deposition, in: Jones, A.C., Hitchman, M.L. (Eds.), Chemical Vapour Deposition. Royal Society of Chemistry, Cambridge, pp. 158–206.

Robertson, J., 2006. Rep. Prog. Phys. 69, 327–396.

Saha, B., Acharya, J., Sands, T.D., Waghmare, U.V., 2010. J. Appl. Phys. 107, 033715.

Sanz, J.., Soriano, L., Prieto, P., Tyuliev, G., Morant, C., Elizalde, E., 1998. Thin Solid Films 332, 209–214.

Satta, A., Vantomme, A., Schuhmacher, J., Whelan, C.M., Sutcliffe, V., Maex, K., 2004. Appl. Phys. Lett. 84, 4571.

Scheller, M., Jansen, C., Koch, M., 2010. Applications of Effective Medium Theories in the Terahertz Regime, in: Young, K. (Ed.), Recent Optical and Photonic Technologies. InTech.

Seitz, H., Schröder, B., 2000. Solid State Commun. 116, 625–629.

Senzaki, Y., Park, S., Chatham, H., Bartholomew, L., Nieveen, W., 2004. J. Vac. Sci. Technol. Vac. Surf. Films 22, 1175.

Shevjakov, A.M., Kuznetsova, G.N., Aleskovskii, V.B., 1965. Interaction of titanium and germanium tetra-chlorides with hydrated silica, in: High Temperature Chemistry of Oxides. Presented at the 2nd USSR Conference on High Temperature Chemistry of Oxides, Lenin- grad, USSR (Nauka, Leningrad, USSR, 1967), pp. 149–155.

Signore, M.A., Valerini, D., Tapfer, L., Caretto, G., Rizzo, A., 2011. J. Vac. Sci. Technol. Vac. Surf. Films 29, 061507.

Sivukhin, D.V., 1948. Zhurnal Eksp. Teor. Fiz. 18, 976–994.

Sneh, O., Clark-Phelps, R.B., Londergan, A.R., Winkler, J., Seidel, T.E., 2002. Thin Solid Films 402, 248–261.

Straboni, A., Pichon, L., Girardeau, T., 2000. Surf. Coat. Technol. 125, 100–105.

Strachan, C., 1933. Math. Proc. Camb. Philos. Soc. 29, 116.

Sugiyama, K., 1975. J. Electrochem. Soc. 122, 1545.

Suntola, T., 1989. Mater. Sci. Rep. 4, 261–312.

Swerts, J., Delabie, A., Salimullah, M.M., Popovici, M., Kim, M.-S., Schaekers, M., Van Elshocht, S., 2012. ECS Solid State Lett. 1, P19–P21.

Takeyama, M.B., Noya, A., Sakanishi, K., 2000. J. Vac. Sci. Technol. B Microelectron. Nanometer Struct. 18, 1333.

Theeten, J.B., 1980. Surf. Sci. 96, 275–293.

Thomas, D.J., 1989. J. Vac. Sci. Technol. B Microelectron. Nanometer Struct. 7, 1325.

Tiilikainen, J., Tilli, J.-M., Bosund, V., Mattila, M., Hakkarainen, T., Sormunen, J., Lipsanen, H., 2007. J. Phys. Appl. Phys. 40, 7497–7501.

Tikhonravov, A.V., Trubetskov, M.K., Masetti, E., Krasilnikova, A.V., Kochikov, I.V., 1999. Sensitivity of the ellipsometric angles psi and delta to the surface inhomogeneity, in: Amra, C., Macleod, H.A. (Eds.),

Advances in Optical Interference Coatings. Presented at the Proc. SPIE, pp. 173–182.

Tiznado, H., Bouman, M., Kang, B.-C., Lee, I., Zaera, F., 2008. J. Mol. Catal. Chem. 281, 35–43.

Tompkins, H.G., Irene, E.A., 2005. Handbook of Ellipsometry. William Andrew.

Travis, C.D., Adomaitis, R.A., 2014. Theor. Chem. Acc. 133.

Triyoso, D.H., Hegde, R.I., Grant, J., Fejes, P., Liu, R., Roan, D., Ramon, M., Werho, D., Rai, R., La, L.B., Baker, J., Garza, C., Guenther, T., White, B.E., Tobin, P.J., 2004. J. Vac. Sci. Technol. B Microelectron. Nanometer Struct. 22, 2121.

Valerini, D., Signore, M.A., Rizzo, A., Tapfer, L., 2010. J. Appl. Phys. 108, 083536.

Vedam, K., Rai, R., Lukes, F., Srinivasan, R., 1968. J. Opt. Soc. Am. 58, 526.

Vehkamäki, M., 1999. Electrochem. Solid-State Lett. 2, 504.

Wang, H., Jiang, X., Willis, B.G., 2012. J. Vac. Sci. Technol. Vac. Surf. Films 30, 01A133.

Wendel, H., Suhr, H., 1992. Appl. Phys. Solids Surf. 54, 389–392.

Westlinder, J., Malmström, J., Sjöblom, G., Olsson, J., 2005. Solid-State Electron. 49, 1410–1413.

Wooho, J., 2010. J. Korean Phys. Soc. 56, 905.

Xie, Q., Musschoot, J., Deduytsche, D., Van Meirhaeghe, R.L., Detavernier, C., Van den Berghe, S., Jiang, Y.-L., Ru, G.-P., Li, B.-Z., Qu, X.-P., 2008. J. Electrochem. Soc. 155, H688.

Yanguas-Gil, A., Libera, J.A., Elam, J.W., 2013. ECS Trans. 50, 43–51.

Yasaka, M., 2010. Rigaku J. 26, 1–9.

Yun, J.-H., Choi, E.-S., Jang, C.-M., Lee, C.-S., 2002. Jpn. J. Appl. Phys. 41, L418–L421.